

Copyright  
by  
Jason Andrew Kenney  
2006

The Dissertation Committee for Jason Andrew Kenney  
certifies that this is the approved version of the following dissertation:

**Transient Charging Processes at Liquid-Solid and  
Vacuum-Solid Interfaces**

Committee:

---

Gyeong Hwang, Supervisor

---

Roger Bonnecaze

---

John Ekerdt

---

Brian Korgel

---

Laxminarayan Raja

**Transient Charging Processes at Liquid-Solid and  
Vacuum-Solid Interfaces**

by

**Jason Andrew Kenney, B.S., M.S.**

**DISSERTATION**

Presented to the Faculty of the Graduate School of

The University of Texas at Austin

in Partial Fulfillment

of the Requirements

for the Degree of

**DOCTOR OF PHILOSOPHY**

THE UNIVERSITY OF TEXAS AT AUSTIN

December 2006

Dedicated to my wife Ou and my parents, Bob and Aline.

## Acknowledgments

There are many people who have made my time in Austin special. First and foremost is Ou, who has been everything to me these last three years and with whom I look forward to spending the rest of my life. I was also blessed by two great roommates, Cheung and Morehouse, a couple of guys who insisted on enjoying life and would do anything for a friend.

I would be remiss if I did not thank Gyeong for the opportunity he gave me to come to Austin. He has managed to build a great research group in a short period of time, and I appreciate the friendships made with my coworkers, particularly Devina and SH.

Outside of Austin, I have always had a wonderful group of friends and family supporting me. This is especially true of my parents, my brother, and Jon, all of whom have always been there for me.

# **Transient Charging Processes at Liquid-Solid and Vacuum-Solid Interfaces**

Publication No. \_\_\_\_\_

Jason Andrew Kenney, Ph.D.  
The University of Texas at Austin, 2006

Supervisor: Gyeong Hwang

The behavior of transient charging processes at interfaces has become increasingly important in the manufacture of materials on the micron-scale and below. Herein, the modeling and simulation of processes occurring at liquid-solid and vacuum-solid interfaces are considered. For the liquid-solid interface, an electrochemical machining system is modeled using equivalent circuits. Comparisons are then made between experimental and model results for transient current response and machining resolution. Predictions are given regarding the use of complex electrode shapes. For the vacuum-solid interface, surface charging of dielectric under plasma bombardment is considered. A high aspect ratio structure with varying absolute dimension is used with a bimodal ion energy distribution, and the resulting fluxes and energies of ions investigated.

# Table of Contents

<b>Acknowledgments</b>	<b>v</b>
<b>Abstract</b>	<b>vi</b>
<b>List of Tables</b>	<b>x</b>
<b>List of Figures</b>	<b>xi</b>
<b>Chapter 1. Introduction</b>	<b>1</b>
<b>Chapter 2. Liquid-Solid Interface: Electrochemistry and Microfabrication</b>	<b>3</b>
2.1 Electrochemical Microfabrication . . . . .	3
2.1.1 Overview . . . . .	3
2.1.2 ECM with Ultrashort Voltage Pulses . . . . .	4
2.2 Electrochemical Concepts . . . . .	6
2.2.1 Electrochemical Double Layer . . . . .	7
2.2.2 Faradaic Current . . . . .	12
2.2.3 Capacitive Current . . . . .	14
<b>Chapter 3. Computational Modeling: ECM with Ultrashort Voltage Pulses</b>	<b>17</b>
3.1 Background . . . . .	17
3.2 Computational Model . . . . .	19
3.2.1 Assumptions . . . . .	19
3.2.2 Overview . . . . .	21
3.2.3 Transient Charging Simulation . . . . .	22
3.2.4 Profile Evolution . . . . .	27

<b>Chapter 4. Simulation Results:</b>	
<b>ECM with Ultrashort Voltage Pulses</b>	<b>31</b>
4.1 Transient Current Response . . . . .	31
4.2 Overpotential and Dissolution Current Evolution . . . . .	34
4.3 Lateral Etch Resolution . . . . .	36
4.3.1 2D Computational Model Calculations . . . . .	39
4.3.2 2D Theory . . . . .	40
4.3.3 3D Computational Model Calculations . . . . .	47
4.4 Tool Templates . . . . .	50
4.5 Summary . . . . .	60
<b>Chapter 5. Vacuum-Solid Interface:</b>	
<b>Differential Surface Charging of Dielectric</b>	<b>62</b>
5.1 Plasma Background . . . . .	62
5.2 Plasma Etching and Deposition . . . . .	64
5.2.1 Overview . . . . .	64
5.2.2 Differential Charging . . . . .	65
<b>Chapter 6. Computational Modeling:</b>	
<b>Plasma Charging of Nanopatterned Dielectric</b>	<b>67</b>
6.1 Background . . . . .	67
6.2 Computational Model . . . . .	69
6.2.1 Assumptions . . . . .	69
6.2.2 Overview . . . . .	70
6.2.3 Ion and Electron Generation . . . . .	71
6.2.4 Potential Calculation . . . . .	72
6.2.5 Particle Trajectory Calculation . . . . .	75
6.2.6 Surface Conduction . . . . .	76
<b>Chapter 7. Simulation Results:</b>	
<b>Plasma Charging of Nanopatterned Dielectric</b>	<b>78</b>
7.1 Transient Potential . . . . .	78
7.2 Potential Statistics . . . . .	83
7.3 Potential Contours . . . . .	84



7.4 Ion Trajectories . . . . .	88
7.5 Exiting Ion Flux and Energy . . . . .	89
7.6 Summary . . . . .	95
<b>Chapter 8. Conclusion</b>	<b>97</b>
<b>Appendices</b>	<b>99</b>
<b>Appendix A. Electrochemical Fabrication Processes</b>	<b>100</b>
A.1 Hole Drilling Processes . . . . .	101
A.1.1 Electrochemical Drilling . . . . .	101
A.1.2 Shaped Tube Electrochemical Machining . . . . .	102
A.1.3 Electrochemical Jet Machining . . . . .	103
A.1.3.1 Capillary and Electro Stream Drilling . . . . .	104
A.1.3.2 Jet Electrolytic Drilling . . . . .	105
A.1.3.3 Other ECJM . . . . .	106
A.2 Surface Finishing . . . . .	107
A.2.1 Electroplating . . . . .	107
A.2.2 Electrochemical Polishing . . . . .	109
A.3 Electroforming . . . . .	111
A.4 Microfabrication . . . . .	111
A.4.1 Masked Processes . . . . .	111
A.4.2 Damascene Process . . . . .	113
A.4.3 Pulsed Electrochemical Machining . . . . .	114
<b>Appendix B. Product Effect on Electrolyte Resistivity</b>	<b>117</b>
<b>Appendix C. Electrolyte Resistivity Calculation</b>	<b>120</b>
<b>Appendix D. Capacitance Calculation</b>	<b>123</b>
<b>Appendix E. Particle Trajectory Calculation</b>	<b>125</b>
<b>Bibliography</b>	<b>129</b>

<b>Index</b>	<b>139</b>
<b>Vita</b>	<b>141</b>

## List of Tables

7.1	Transient Potential Statistics . . . . .	83
-----	--	----

## List of Figures

2.1	Schematic of ECM-USVP system, indicating the different resistances encountered by current pathways. Lines at the tool and workpiece (substrate) electrodes indicate the electrochemical double layer. . . . .	6
2.2	Schematic of the electrochemical double layer. The locus of centers of specifically-adsorbed ions form the inner Helmholtz plane (IHP). The outer Helmholtz plane (OHP) is the locus of centers of solvated-ions at closest approach to the electrode surface. . . . .	8
2.3	Normalized potential with distance from outer Helmholtz plane for a 1:1 electrolyte at 300 K with the indicated outer Helmholtz plane potentials and bulk concentrations. . . . .	10
2.4	Double layer capacity with electrode potential relative to bulk electrolyte, for the indicated bulk electrolyte concentrations. Outer Helmholtz plane is assumed located 3 Å from electrode, and the dielectric constant of the compact layer is set equal to 5. Electrolyte is 1:1 and at 300 K. . . . .	11
2.5	Schematic of a typical current vs. potential curve. The region between the initial reduction and initial oxidation corresponds to ideal polarized electrode behavior. . . . .	13
2.6	Current density $j$ as a function of overpotential for the indicated values of the exchange current density. Smaller values of the exchange current density give larger regions of ideal polarized electrode behavior. $T$ is 300 K and $\alpha$ is 0.5. . . . .	14
2.7	Current density vs. overpotential for the Butler-Volmer equation and anodic and cathodic Tafel equations in the region of largest discrepancies. Outside of this overpotential range, Tafel behavior almost precisely matches that of the Butler-Volmer form. For this calculation, $j_0$ is $1 \cdot 10^{-3}$ A/m <sup>2</sup> , $T$ is 300 K, and $\alpha$ is 0.5. . . . .	15
2.8	Equivalent circuit for an electrode-double layer-electrolyte half-cell. The double layer capacitance ( $C_d$ ) is in parallel with the polarization resistance ( $R_p$ ). Connections from this structure are made to the electrode and bulk electrolyte resistance ( $R_s$ ). . . . .	16

3.1	Flowchart depicting the major components and linkages for the ECM-USVP Computational Model. . . . .	22
3.2	Schematic of the equivalent circuit used in the ECM-USVP Computational Model. The electrolyte takes the form of a resistor mesh. Connections are made to the tool and substrate electrodes through capacitors in parallel, representing the double layers at those surfaces. Black dots indicate nodes in the electrolyte where potentials are found during the transient charging simulation. Reflective boundary conditions indicated with dashed lines. . . . .	23
4.1	Transient current response during one 50:500 ns pulse:pause period for (a) 2D and (b) 3D computational models. . . . .	35
4.2	Evolution of the overpotential along the substrate for a 50 ns, -1.6 V pulse and the indicated tool-substrate separations. Tool diameter is 10 $\mu\text{m}$ . . . . .	37
4.3	Evolution of the dissolution current along the substrate for a 50 ns, -1.6 V pulse and the indicated tool-substrate separations. Tool diameter is 10 $\mu\text{m}$ . All values are normalized by the largest value obtained at a separation of 1 $\mu\text{m}$ . . . . .	38
4.4	(a) Machining system used to measure resolution. 2D region used in computational model indicated by plane. (b) Definition of resolution ( $d_1$ ) and gap space at the leading edge of the tool ( $d_2$ ). . . . .	39
4.5	(a) 2D etch resolutions with pulse duration for a lateral etching process using the indicated tool diameters. (b) Ratios of the 2D resolutions relative to those obtained at 25 ns for each tool diameter. Degree of sub-linearity increases with decreasing tool diameter. . . . .	41
4.6	Profile evolution of a lateral etch of the substrate by a 5 $\mu\text{m}$ diameter tool moving at 1.5 $\mu\text{m}/\text{min}$ . Pulse durations as indicated (ns) . . . . .	42
4.7	Schematic of the geometry used in the 2D stationary system. Resolution is indicated by the quantity $r_2 - r_1$ . . . . .	43
4.8	(a) Etch resolutions derived from a stationary two-dimensional model as a function of tool radius and pulse duration. (b) Ratio of etch resolution to pulse duration, normalized by limiting values at pulse durations of 0, for stationary two-dimensional model. Value of 1 indicates a linear increase in resolution with pulse duration. . . . .	45

4.9	(a) Etch profiles for a tool of radius $2.5\ \mu\text{m}$ etched to a depth of $5\ \mu\text{m}$ . Pulse duration as indicated (ns). (b) Etch resolution ratios relative to that of a 25 ns pulse at varying etch depths. Horizontal lines indicate linear behavior. . . . .	49
4.10	Underside of surface etched laterally at a depth of $5\ \mu\text{m}$ for a distance of $60\ \mu\text{m}$ . A $10\ \mu\text{m}$ diameter tool moving at $1.5\ \mu\text{m}/\text{min}$ was used, along with 100 ns pulses of -2.3 V applied to the tool with a 1:10 pulse:pause ratio. . . . .	50
4.11	(a) 3D etch resolutions with pulse duration for a lateral etching process using the indicated tool diameters. (b) Ratios of the 3D resolutions relative to those obtained at 25 ns for both tool diameters. . . . .	51
4.12	Schematic of the parallel etching system. . . . .	53
4.13	Midpoint etch depth vs. tool separation for the parallel and series cases at the indicated pulse durations. Schematics indicate joining and separation of the holes formed at the different tool separations. Inset: Difference in midpoint etch depth (parallel case - series case). . . . .	54
4.14	Profiles of the resulting holes after etching with 25 ns pulses at a separation of $6\ \mu\text{m}$ , edge-to-edge, with tool(s) of diameter $5\ \mu\text{m}$ , for (a) series and (b) parallel cases. . . . .	55
4.15	Cross sections showing the overpotential at the end of a 50 ns pulse at the substrate surface for tool located at (a) the initial substrate surface and (b) $40\ \mu\text{m}$ below the initial substrate surface. Tool Separation is $8\ \mu\text{m}$ . The series overpotential is the sum of the individual tool contributions. The difference is defined as parallel - series. . . . .	57
4.16	Cross sections showing the relative dissolution current at the end of a 50 ns pulse at the substrate surface for tool located at (a) the initial substrate surface and (b) $40\ \mu\text{m}$ below the initial substrate surface. Tool Separation is $8\ \mu\text{m}$ . The series dissolution current is the sum of the individual tool contributions. The difference is defined as parallel - series. . . . .	58
4.17	Cross sections showing the (a) overpotential and (b) relative dissolution current at the end of a 50 ns pulse at the substrate surface for the unit cell of an array of tools separated by $8\ \mu\text{m}$ in both $x$ and $y$ dimensions. Tools were held $3\ \mu\text{m}$ above an unmodified substrate. The series quantities are the sum of the individual tool contributions to the central unit cell of a $5\times 5$ cell region. The difference is defined as parallel - series. . . . .	61

5.1	Schematic of the differential charging process for masked substrates under plasma exposure. High aspect ratio features receive reduced electron flux at the lower trench sidewalls and bottom due to shadowing effects. For the case of insulating materials in either of these regions, surface charging phenomena can result. . . . .	65
6.1	Schematic of the simulation domain used in this study (not to scale). Dielectric structures are represented by the gray rectangles. Upper and lower boundaries indicate the locations from which ions and electrons emerge and may exit, respectively. At these locations, the potential is fixed. Dashed side boundaries indicate reflective boundary conditions. Labeled points indicate locations where potential measurements are taken: (a) trench exit left, (b) trench exit center, and (c) trench exit right. . . .	68
6.2	Flowchart depicting the major components and linkages for the Plasma Charging of Dielectric Computational Model. . . . .	71
6.3	Ion energy distribution function (IEDF) for the directed $z$ velocity. Adapted from [49]. . . . .	72
7.1	Potential with number of particles generated for the indicated trench widths and locations. $T_i = 1$ K. The time-scale of each plot varies with trench width: 500 nm: 0.533 s, 100 nm: 13.3 s, 50 nm: 53.3 s. . . . .	80
7.2	Potential with number of particles generated for the indicated trench widths and locations. $T_i = 300$ K. The time-scale of each plot varies with trench width: 500 nm: 0.533 s, 100 nm: 13.3 s, 50 nm: 53.3 s. . . . .	81
7.3	Potential with number of particles generated for the indicated trench widths and locations. $T_i = 10,000$ K. The time-scale of each plot varies with trench width: 500 nm: 0.533 s, 100 nm: 13.3 s, 50 nm: 53.3 s. . . . .	82
7.4	Potential contours indicating mean ( $\bar{X}$ ) and extreme ( $\bar{X} \pm 2\sigma$ ) behavior, with centerline potentials in the trench region. $T_i = 1$ K. . . . .	85
7.5	Potential contours indicating mean ( $\bar{X}$ ) and extreme ( $\bar{X} \pm 2\sigma$ ) behavior, with centerline potentials in the trench region. $T_i = 300$ K. . . . .	86
7.6	Potential contours indicating mean ( $\bar{X}$ ) and extreme ( $\bar{X} \pm 2\sigma$ ) behavior, with centerline potentials in the trench region. $T_i = 10,000$ K. . . . .	87

7.7	Trajectories of high and low energy ion species passing through trenches with the indicated widths. The electric fields used match the $\bar{X} - 2\sigma$ contours for an ion temperature of 1 K (Figure 7.4) with the appropriate trench width. In all cases, the initial $x$ velocity component is 0. . . . .	90
7.8	Extrusion plots showing numbers and energies of ions reaching the trench exit with the number of combined ions and electrons entering the simulation domain. Intervals of 20,000 combined ions and electrons entering the domain are used between recording of data. The ion energy distribution function of ions entering the simulation domain is also given. $T_i = 1$ K. . . . .	92
7.9	Extrusion plots showing numbers and energies of ions reaching the trench exit with the number of combined ions and electrons entering the simulation domain. Intervals of 20,000 combined ions and electrons entering the domain are used between recording of data. The ion energy distribution function of ions entering the simulation domain is also given. $T_i = 300$ K. . . . .	93
7.10	Extrusion plots showing numbers and energies of ions reaching the trench exit with the number of combined ions and electrons entering the simulation domain. Intervals of 20,000 combined ions and electrons entering the domain are used between recording of data. The ion energy distribution function of ions entering the simulation domain is also given. $T_i = 10,000$ K. . . . .	94
B.1	Schematic of the geometry used to calculate the influence of dissolution products on electrolyte resistivity. . . . .	118
C.1	Resistivity with $H_2SO_4$ concentration for 0.1 M $CuSO_4$ mixtures. Lines indicate estimates according to $CuSO_4$ and $H_2SO_4$ equivalents and their average. Dots represent the solutions used in [72]. . . . .	122
D.1	Illustration of varying resistances of connections made to the substrate electrode in the $x$ and $z$ directions. The angle formed by a connection to the substrate helps to determine the capacitance of the connection. . . . .	123



# Chapter 1

## Introduction

Transient charging processes at interfaces are involved in several of the key technologies by which micron- and nanometer-scale devices are fabricated today. In some cases, the charging occurs by design, such as with electrochemical methods or electrical discharge machining. Here, a greater understanding of transient behavior can be used to improve the process performance and control. In other cases, the charging occurs as a side effect of the method being used, such as the charging of insulating surfaces which can occur during plasma processing. Increased knowledge as to how this charging can change as device dimensions shrink is an important step in combating the problem.

In this work, transient charging processes occurring during two different processing technologies are investigated through use of computational models. For the first, a novel electrochemical machining system is considered, capable of sub-micron resolution. Here the transient charging at liquid-solid interfaces occurs by design but is not well understood. For the second, plasma interactions with dielectric surfaces are studied. In this case, the charging processes at the vacuum-solid interfaces are undesired and can have significant negative effects. It is believed that these are, respectively, the first computational treatment of this particular electrochemical machining technology and the first investigation of dielectric charging in plasma considering the individual effects of ions and electrons rather than averaged behaviors.

The descriptions herein follow a general format for both technologies. First, background information is provided about the technology at hand, with an emphasis on relevant concepts applicable to the modeling process. Next, the model is developed. This involves a stating of assumptions, an overview of the computational structure, and a description of numerical techniques and equations used. This is followed by results from the modeling effort. These include comparisons with experimental data and trends for validation where possible, along with predicted behaviors.

## Chapter 2

# Liquid-Solid Interface: Electrochemistry and Microfabrication

Electrochemistry is a mature field, with the scholarly work of Galvani and Volta dating from the late 1700s and commercial applications as far back as the 1850s. In the more than two centuries of active research, a thorough understanding of electrochemical processes has been developed, with implications on physical phenomena ranging from corrosion to biochemical pathways. In addition, a wide variety of applications has been discovered, including power sources (e.g. batteries and fuel cells), electroanalytical sensors, electrolysis for purification of metals (e.g. Al, Cu), and the etching/deposition of metals.

## 2.1 Electrochemical Microfabrication

### 2.1.1 Overview

Electrochemical techniques, however, have found limited use in the processing of structures with sizes in the micron range and smaller, such as those found in semiconductor devices and micro-electro-mechanical systems (MEMS), owing to the difficulty in localizing electrochemical reactions using traditional methods. To overcome this limitation, several techniques (see Appendix A) have been developed which allow for selective modification of substrates on the micron-scale and below. These methods generally involve some means by which the electrochemical reactions are physically prevented

from occurring in undesired locations. For example, the dual Damascene process for copper interconnect fabrication employs patterned resist layers and dry etching technologies to create trenches and vias to be filled with copper in a single electrochemical deposition step, followed by chemical mechanical polishing (CMP) [8]. Similarly, the LIGA process uses electroforming onto masked surfaces for the production of high aspect ratio features, useful for MEMS fabrication [50]. Alternately, resist layers can be used to mask a surface prior to electrochemical dissolution, in a similar fashion to “wet” chemical etching. With the electrochemical process, however, some control may be exerted over mass transport and current distribution to limit lateral etching and the resulting undercutting of the mask, unlike the isotropic etching found in typical “wet” processes [18]. Finally, maskless physical confinement of the electrolyte in the form of a fine electrolyte jet impinging on the substrate has been investigated. Nozzles ranging in diameter from 200  $\mu\text{m}$  down to 50  $\mu\text{m}$  have been used to limit the diameter of the resulting flow, allowing for the creation of features of sub-millimeter resolution [20, 44]. Through superposition of multiple passes, complex 3D structures can be formed [55].

### **2.1.2 ECM with Ultrashort Voltage Pulses**

In recent years, an alternate approach to localizing electrochemical reactions has been developed which does not require physical separation between the electrolyte and areas not to be modified. By using voltage pulses of tens of nanoseconds or shorter applied to a tool electrode, electrochemical micro- and nano-structuring of electrically-conductive substrates such as copper [40, 63, 64], gold [40, 63, 64, 75, 76], stainless steel [5, 39], nickel [41, 72], and p-type silicon [6, 63, 73] has been performed. The technique is known as

electrochemical machining (ECM) with ultrashort voltage pulses (hereafter, ECM-USVP), the “machining” moniker following from the naming of other electrochemical dissolution methods which have been used as alternatives to traditional machining processes. It relies on the differing rates of charge accumulation of regions of the substrate relatively close to and far from the tool electrode, owing to the increased resistance of longer current pathways between tool and substrate, as illustrated in Figure 2.1. With voltage pulses in the nanosecond regime, the rate of charge accumulation in regions more than several microns away from the tool can be made negligible, suppressing electrochemical reactions. The use of 500 ps pulses has realized feature sizes as small as 200 nm, with gaps between tool and substrate of approximately 80 nm [41].

This type of ECM offers several benefits over other approaches, both electrochemical and otherwise. As masks are not required, single-step processing of substrates is possible, giving advantages over LIGA processing. In addition, three-dimensional shaping of complex structures has been demonstrated [39], as well as high aspect ratio columns and holes [5, 36, 37], areas where lithographic plasma technologies have had difficulty. As with other ECM techniques, it is capable of machining hard, brittle materials, unlike traditional machining techniques which involve physical interaction between the tool and substrate. The dissolution process also tends to leave surface properties such as composition and crystal structure intact, in contrast with the thermal layers arising from electrical discharge machining (EDM) [52]. Potential applications include fabrication of MEMS, biological and medical devices, sensors, and high performance 2D photonic band gap materials, and deposition of self-aligned, submicron-sized metal clusters.

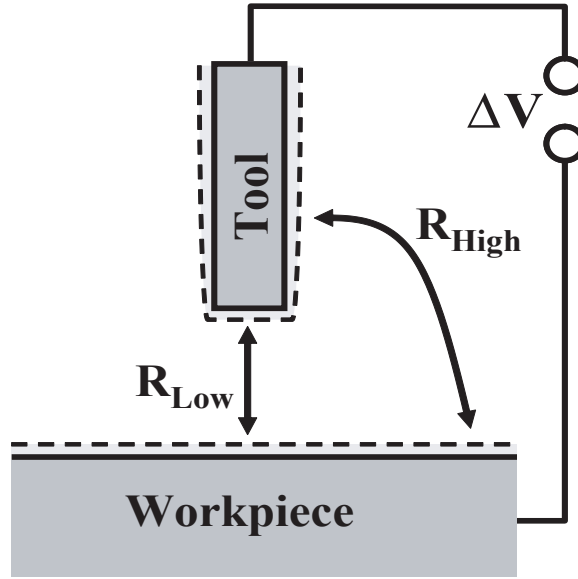


Figure 2.1: Schematic of ECM-USVP system, indicating the different resistances encountered by current pathways. Lines at the tool and workpiece (substrate) electrodes indicate the electrochemical double layer.

Herein, computational modeling of ECM-USVP is considered for dissolution processes with resolutions above  $1\ \mu\text{m}$ . In this chapter, background material on relevant electrochemical concepts is presented. This will include discussion of the structure and properties of the electrochemical double layer as well as the models of faradaic and capacitive currents. In the following chapter, simplifying assumptions to these electrochemical concepts will be given as they pertain to ECM-USVP.

## 2.2 Electrochemical Concepts

Electrochemistry is to a large degree concerned with the transport of charge across the interface between differing chemical phases. This most com-

monly occurs in the form of a metal electrode (electronic conductor) in contact with an electrolyte solution (ionic conductor). When an electric potential is applied and current flows, charge is transported through the electrolyte phase via the movement of ion species and the electrode via electrons/holes. The choice of electrode materials, the magnitude and polarity of the potentials applied, and the type and strength of the electrolyte all play roles in the rate at which charge is transferred across the interfaces.

### 2.2.1 Electrochemical Double Layer

The above quantities also determine the structure of the electrode-solution interface, depicted in Figure 2.2. Commonly referred to as the electrochemical double layer, the solution side consists of compact and diffuse layers. The compact layer is composed of solvent molecules and specifically-adsorbed ions, the electrical centers of which combine to form the inner Helmholtz plane (IHP). Further into the electrolyte region is the outer Helmholtz plane (OHP), defined as the closest distance to which solvated ions may approach the electrode surface. From this plane and beyond, interactions between the ions and electrode are electrostatic rather than chemical, and a diffuse layer forms containing a charge equal and opposite that of the electrode surface, less the charge contained within the compact layer. At equilibrium, this diffuse layer shields the electrode charge from the bulk electrolyte.

As the IHP has a thickness on the order of that of atomic radii, the double layer thickness is essentially that of the diffuse layer. According to Gouy-Chapman-Stern theory [10], at equilibrium the potential decay for a  $z:z$  electrolyte away from the OHP is given by

$$\frac{\tanh(ze\phi/4kT)}{\tanh(ze\phi_2/4kT)} = e^{-(x-x_2)/\lambda} \quad (2.1)$$

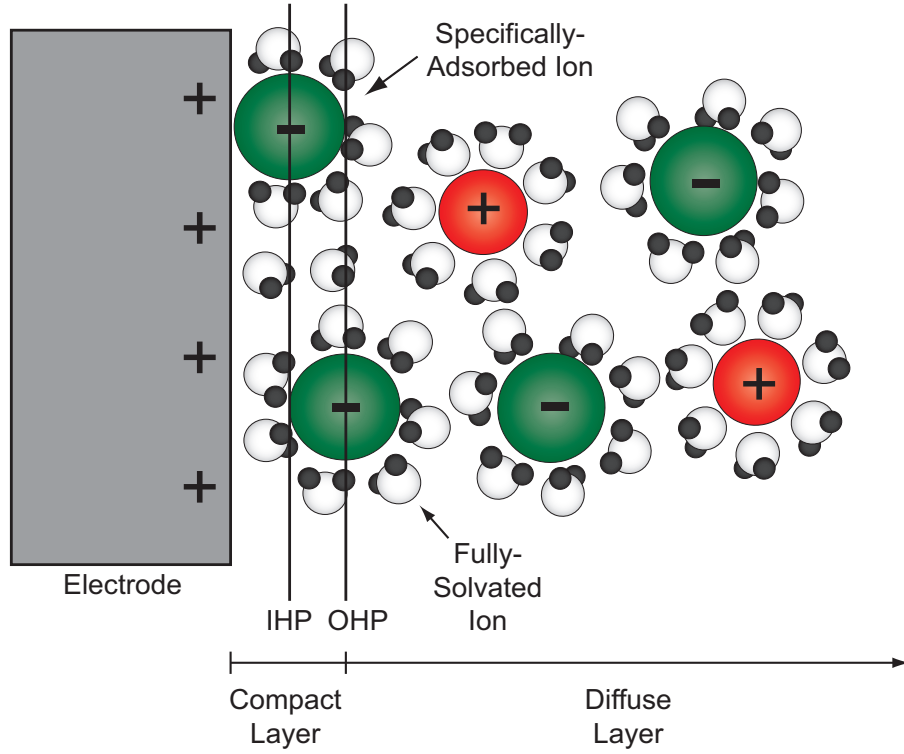


Figure 2.2: Schematic of the electrochemical double layer. The locus of centers of specifically-adsorbed ions form the inner Helmholtz plane (IHP). The outer Helmholtz plane (OHP) is the locus of centers of solvated-ions at closest approach to the electrode surface.

where  $z$  is the magnitude of the charge of the electrolyte species;  $e$  is the charge of an electron;  $\phi$  is the potential, relative to the bulk electrolyte, at position  $x$ ;  $\phi_2$  is the potential, relative to the bulk electrolyte, at position  $x_2$  (location of the OHP);  $k$  is the Boltzmann constant;  $T$  is the temperature; and  $\lambda$  is the Debye length of the electrolyte solution, which for a  $z:z$  electrolyte is given by

$$\lambda = \left( \frac{\varepsilon \varepsilon_0 k T}{2 n^0 z^2 e^2} \right)^{1/2} \quad (2.2)$$

with  $\varepsilon$  the dielectric constant (for water,  $\sim 80$ ),  $\varepsilon_0$  the permittivity of free space,



and  $n^0$  the number concentration of each ion in the bulk. Several potential profiles are given in Figure 2.3 for values of  $\phi_2$  and concentration relevant to ECM processing. In all cases, the diffuse layer (and hence the double layer) has a thickness at or under 10 nm.

A consequence of the electrode charge and solution-side charge shielding in the compact and diffuse layers is capacitor-like behavior of the electrochemical double layer. Stern's modification [10] to Gouy-Chapman theory recognized that this capacitance has contributions from the compact layer, which is somewhat fixed based on the dielectric constant of the medium and distance to the OHP, and the diffuse layer, which will vary according to electrode potential and electrolyte concentration and composition, among other factors. As these capacitances are in series, it is convenient to express the overall double layer capacitance with its inverse,

$$\begin{aligned}\frac{1}{C_d} &= \frac{x_2}{\varepsilon\varepsilon_0} + \frac{1}{(2\varepsilon\varepsilon_0 z^2 e^2 n^0 / kT)^{1/2} \cosh(ze\phi_2/2kT)} \\ &= \frac{1}{C_{Compact}} + \frac{1}{C_{Diffuse}},\end{aligned}\tag{2.3}$$

where  $C_d$ ,  $C_{Compact}$ , and  $C_{Diffuse}$  are the double layer, compact layer, and diffuse layer capacities, respectively<sup>1</sup>. Taking into account the relationship between the electrode and OHP potentials ( $\phi_0 = \phi_2 - x_2 (\frac{d\phi}{dx})|_{x_2}$ ), Figure 2.4 examines the double layer capacity vs. the electrode potential for different electrolyte concentrations. For these calculations, the OHP is located 3 Å from the electrode, and the dielectric constant within the compact layer is estimated at 5, considering the lack of mobility and orientational freedom for water molecules there as opposed to the bulk electrolyte [23]. The resulting

---

<sup>1</sup> $C_d$  is often used for both capacitance and capacity [= capacitance/area]. Consideration of the units should make clear which definition is being used.

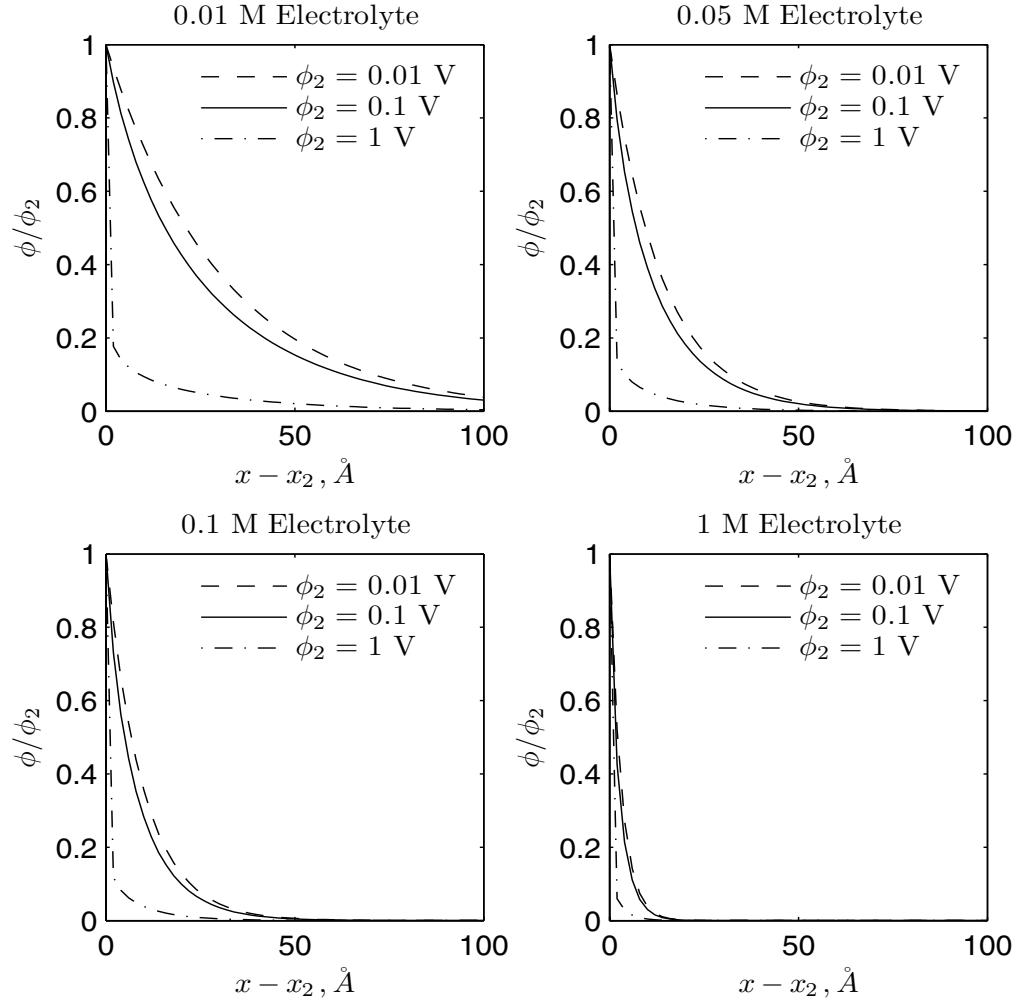


Figure 2.3: Normalized potential with distance from outer Helmholtz plane for a 1:1 electrolyte at 300 K with the indicated outer Helmholtz plane potentials and bulk concentrations.

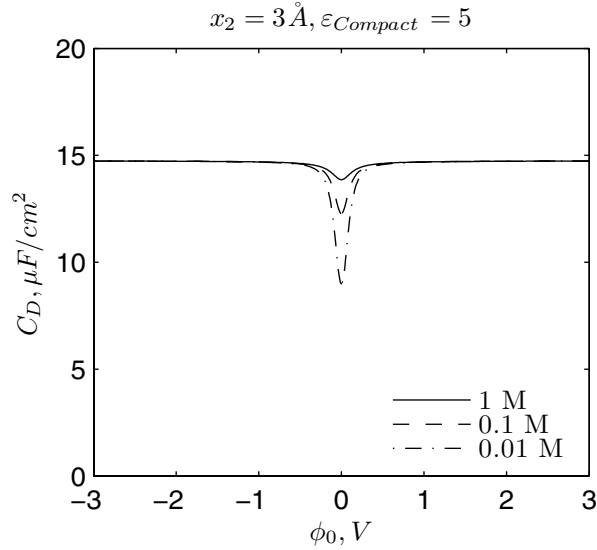


Figure 2.4: Double layer capacity with electrode potential relative to bulk electrolyte, for the indicated bulk electrolyte concentrations. Outer Helmholtz plane is assumed located 3 Å from electrode, and the dielectric constant of the compact layer is set equal to 5. Electrolyte is 1:1 and at 300 K.

capacities indicate little change for the higher concentrations at all electrode potentials.

Two types of processes occur at the electrode-solution interface, referred to as faradaic and nonfaradaic. Faradaic processes are those in which charge transfer occurs across the interface, resulting in reduction or oxidation. As these are the processes which result in electrochemical modification, considerable effort has gone into their understanding, modeling, and manipulation. Other events which occur at the interface, including adsorption/desorption and changes to the electrochemical double layer structure, are termed non-faradaic. These processes may occur naturally at equilibrium or as a result of changes in the electrode potential or electrolyte composition. During oxidation

or reduction, both faradaic and nonfaradaic processes occur [11].

### 2.2.2 Faradaic Current

The equilibrium behavior of many electrochemical systems has been investigated, generating current-potential curves for a variety of electrode-electrolyte combinations. A schematic of a typical curve is given in Figure 2.5. A common feature of these curves is a region where changes in potential do not result in appreciable current, a result of the thermodynamically-possible reactions having very slow kinetics. In such regions, the electrode is referred to as an ideal polarized electrode (IPE) and the double layer acts essentially as a capacitor. At more positive and negative potentials, oxidations and reductions occur, respectively, resulting in anodic (oxidation) and cathodic (reduction) currents.

It is important to note a distinction in the types of current considered in electrochemical systems and how they are modeled. The current from the current-potential curve at equilibrium consists primarily of faradaic current, the anodic and cathodic currents resulting from oxidation and reduction processes. For systems which are not mass transfer limited, it is often modeled by the Butler-Volmer equation [12],

$$i = i_0[e^{-\alpha F\eta/RT} - e^{(1-\alpha)F\eta/RT}], \quad (2.4)$$

where  $i$  is the faradaic current;  $i_0$  is the exchange current;  $\alpha$  is the transfer coefficient, typically on the range of 0.3 to 0.7;  $F$  is the Faraday constant;  $R$  is the gas constant; and  $\eta$  is the overpotential, which is defined as the deviation of electrode potential from the equilibrium potential. The component terms of the right hand side of the equation represent the cathodic current (left) and

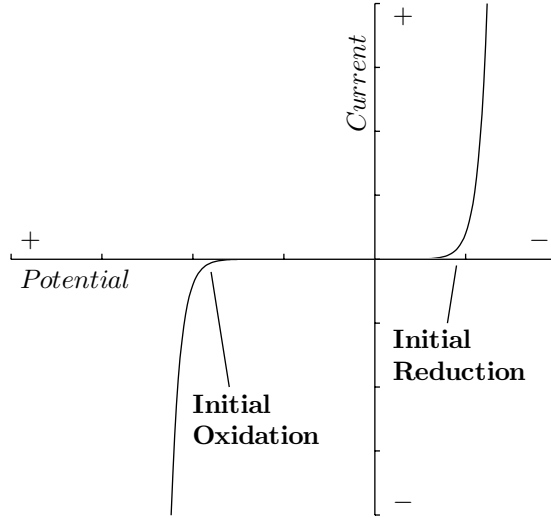


Figure 2.5: Schematic of a typical current vs. potential curve. The region between the initial reduction and initial oxidation corresponds to ideal polarized electrode behavior.

anodic current. Figure 2.6 illustrates the use of Equation 2.4 with different values of the exchange current density ( $j_0 = i_0/A$ ), making clear its role in IPE behavior.

For sufficiently large (magnitude) overpotentials, either the anodic or cathodic current will effectively dominate. Consider the ratio of currents:

$$\frac{i_A}{i_C} = \frac{e^{(1-\alpha)F\eta/RT}}{e^{-\alpha F\eta/RT}} = e^{F\eta/RT} \quad (2.5)$$

At 300 K, this ratio will be greater than 100 for an overpotential greater than 0.120 V (or less than 0.01 for an overpotential less than -0.120 V). Such cases are termed Tafel behavior, and the suppressed term may be dropped [13]:

$$i = i_0 e^{-\alpha F\eta/RT} \text{ (cathodic)} \quad (2.6)$$

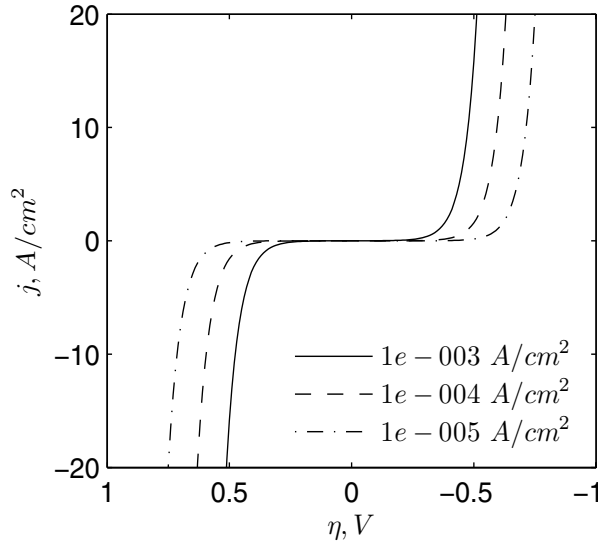


Figure 2.6: Current density  $j$  as a function of overpotential for the indicated values of the exchange current density. Smaller values of the exchange current density give larger regions of ideal polarized electrode behavior.  $T$  is 300 K and  $\alpha$  is 0.5.

$$i = -i_0 e^{(1-\alpha)F\eta/RT} \text{ (anodic)} \quad (2.7)$$

Figure 2.7 gives a comparison of faradaic current density as approximated by the Butler-Volmer equation and by Tafel behavior, at an exchange current density relevant to ECM-USVP [63].

### 2.2.3 Capacitive Current

The other major current in electrochemical systems is the capacitive current, also known as the double-layer or nonfaradaic current. This current primarily flows transiently while the double layer is charging or discharging, usually due to a change in electrode potential, and is considered the portion of the overall current that does not involve charge transfer across the electrode-

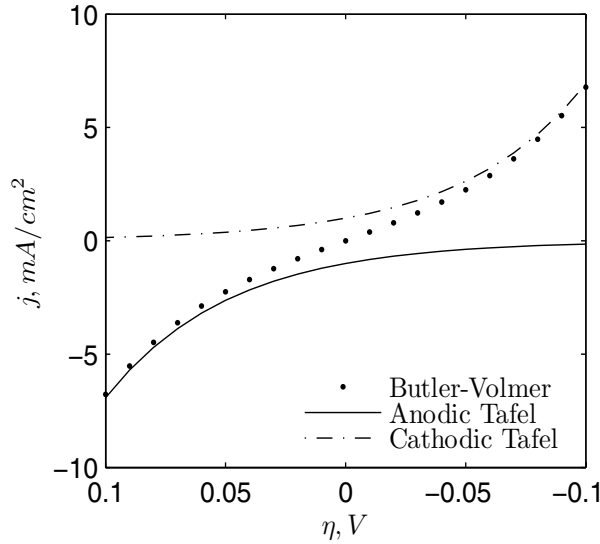


Figure 2.7: Current density vs. overpotential for the Butler-Volmer equation and anodic and cathodic Tafel equations in the region of largest discrepancies. Outside of this overpotential range, Tafel behavior almost precisely matches that of the Butler-Volmer form. For this calculation,  $j_0$  is  $1 \cdot 10^{-3}$  A/m<sup>2</sup>,  $T$  is 300 K, and  $\alpha$  is 0.5.

electrolyte interface [17]. Some charge transfer (and hence faradaic current) does occur during these charging processes, however, and thus even for an electrode exhibiting IPE characteristics there is a resistive component to the double layer. It is typically referred to as the polarization resistance ( $R_p$ ), and an equivalent circuit for the electrode-double layer-electrolyte structure has it in parallel with the double layer capacitance, as illustrated in Figure 2.8. Electrochemical impedance spectroscopy [60] has been used to characterize the polarization resistance and other attributes of the equivalent circuit, demonstrating the dependence of  $R_p$  on electrode potential and indicating its tendency to be orders of magnitude larger than the solution resistance at low

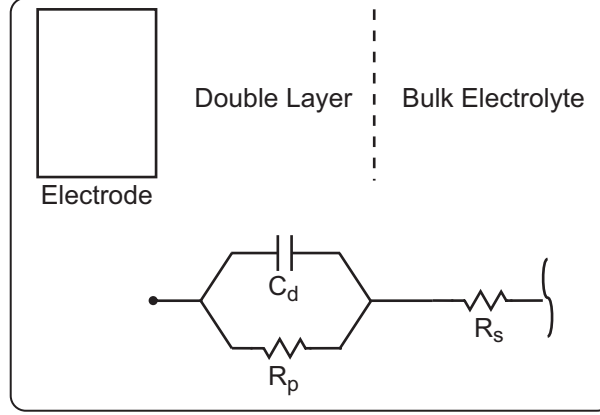


Figure 2.8: Equivalent circuit for an electrode-double layer-electrolyte half-cell. The double layer capacitance ( $C_d$ ) is in parallel with the polarization resistance ( $R_p$ ). Connections from this structure are made to the electrode and bulk electrolyte resistance ( $R_s$ ).

applied potentials [78]. The current response obtained from the equivalent circuit is as follows [77]:

$$i = \frac{V}{R_s} e^{-[(R_p + R_s)/R_p R_s C_d]t} + \frac{V}{R_p + R_s} \{1 - e^{-[(R_p + R_s)/R_p R_s C_d]t}\}, \quad (2.8)$$

where  $V$  is the applied potential,  $R_s$  is the electrolyte solution resistance, and  $R_p$  is the polarization resistance. In the limit of  $R_p \gg R_s$  and ignoring large values of  $t$ , Equation 2.8 reduces to

$$i = \frac{V}{R_s} e^{-t/R_s C_d}, \quad (2.9)$$

which describes the current decay of an RC circuit.



## Chapter 3

# Computational Modeling: ECM with Ultrashort Voltage Pulses

In this chapter, additional background on the ECM-USVP process is given, with a narrowing of focus to a specific system of interest. This is followed by a discussion of assumptions made and an overview of the computational model structure. Major model components will then be discussed in detail regarding relevant equations and numerical techniques used.

### 3.1 Background

The use of ultrashort voltage pulses for electrochemical modification was first reported by Schuster, et al. [64], extending the work of others who had been attempting nanoscale modification of surfaces using scanning tunneling microscope (STM) tips [42, 46]. The work was later refined into a micromachining system with the addition of 3D control of the movement of the tool electrode [63], allowing milling on the micron-scale of complex shapes into and selective deposition onto metal surfaces. This technique has since been extended to create sub-micron structures [41], allow the use of complex tool geometries [72], and modify doped semiconductor substrates [6].

In a typical machining application, the tool is held in close proximity to the substrate in the presence of electrolyte. An ultrashort (where “ultrashort”

is loosely defined as 100 ns or shorter) negative bias is applied to the tool, followed by a pause period, usually in a ratio of 1:10 pulse:pause. During the pulse, charge accumulates in the double layers at the tool and regions of the substrate in close proximity to the tool, building overpotentials and driving electrochemical reactions. The following pause allows the discharge of the double layers, preventing the region of electrochemical modification at the substrate from spreading.

A wide variety of compositions and concentrations has been used for the electrolytes in ECM-USVP. Nickel has been etched in HCl solutions with concentrations as low as 0.05 M [72]. Initial reports of machining of stainless steel used a 3 M HCl/6 M HF solution to prevent chromium film formation [39], but subsequently this was shown possible in 0.1 M  $\text{H}_2\text{SO}_4$  through use of a balance electrode [5]. Studies have shown that the critical limit at or below which machining will not occur is  $\sim 0.01$  M for both salts [64] and acids [72]. A typical choice of electrolyte is a moderate salt ( $\sim 0.1$  M) combined with acid at a lower concentration ( $\sim 0.01$ -0.1 M), with the salt often of the same material as the substrate.

Operating conditions vary based on the electrolyte, substrate, and application. The largest variation occurs with pulse duration, where pulses can reach as low as 500 ps [41], giving two orders of magnitude of flexibility. Pulse magnitudes have been reported in the range of -1.6 to -6 V. Tool scanning speeds are on the order of microns/min. The substrate electrode is adjusted to the equilibrium potential for dissolution/deposition, such that any movement in its potential during the pulse is essentially overpotential. In a similar fashion, the tool electrode is adjusted to slightly positive of this value to prevent deposition.

Resolutions of ECM-USVP systems range from 80 nm [41] to over 10  $\mu\text{m}$  [72], depending primarily on pulse duration and electrolyte strength, with marginal effects due to the applied potential and scanning speed of the tool electrode across or into the substrate surface. At the lower end of this range, the gap between tool and substrate electrodes is on the order of the thickness of the double layer for weak electrolytes. In these systems, depletion of charge in the gap may occur during the pulse period, when gap ions outside the double layer region are drawn into it to shield the additional charge on the electrode surfaces [64]. This depletion will result in a rapid increase in the electrolyte resistivity in the gap, thus decreasing the current density in the gap region and increasing the importance of mass transport of ions from the bulk electrolyte into the gap.

In this work, the modeling of micron-scale ECM-USVP of metals is considered. These systems typically employ pulse durations of 25-100 ns and tool sizes on the range of microns or larger. They have been the subject of much investigation, allowing for quantitative comparison between experimental and model results. In addition, for many micron-scale systems, the influence of mass transport is negligible, simplifying the model relative to that of the nanoscale case.

## **3.2 Computational Model**

### **3.2.1 Assumptions**

The primary assumptions made are as follows:

1. Charge accumulation in the double layers is not hindered by ion depletion.

This assumption relies on the combination of the micron length-scale of the gaps and the use of a moderately strong electrolyte. For such cases, ample ions for double layer charging should be available.

2. Dissolution products do not significantly impact electrolyte resistivity in the gap region.

Calculations of steady-state diffusion from the gap region to the bulk electrolyte have been made with the operating parameters used in the computational model and the most unfavorable geometry for buildup of reaction products. These calculations indicate a decrease in resistivity of less than 25% for an etch depth of 40  $\mu\text{m}$ , the largest etch depth considered. As this does not take into account other manners of mass transport (migration, convection), the choice of a constant resistivity appears reasonable.

Details of the diffusion calculation are given in Appendix B.

3. Double layer capacity is constant at both tool and substrate.

From the Gouy-Chapman-Stern model of the double layer structure (Figure 2.4), there is very little variation in double layer capacity for electrolytes with concentrations of 0.1 M and larger. This range entails the electrolytes to be used in the computational model.

4. Polarization Resistance is significantly larger than the solution resistance.

Experimental studies on electrode diameters and electrode separations on the order of millimeters give values of polarization resistance which are an order of magnitude larger than the solution resistance and often

larger [78]. As both the polarization and solution resistance scale inversely with the electrode area, this relationship should not only hold but be exacerbated when the system shrinks to the micron-scale, owing to the direct relationship between solution resistance and electrode separation. In addition, experimental evidence from an ECM-USVP system [63] displays a rapid decay in the transient current after application of a pulse indicates behavior similar to that of an RC circuit. Thus the polarization resistance is ignored, and the double layer is considered purely capacitive.

### 3.2.2 Overview

A flowchart depicting the major components and linkages of the computational model for ECM-USVP is given in Figure 3.1. The general strategy is to consider one voltage pulse with a transient charging simulation, use overpotential information from that simulation to determine etch rates at the substrate surface, then evolve the surface and move the tool. As the time-scales of the voltage pulse and tool movement are orders of magnitude apart (several nanoseconds vs. minutes for the tool to move the length of the gap between electrodes), the tool is considered stationary during the pulse for the electrochemical simulation. Once the etch rate information is obtained, the surface is evolved and the tool moved for a duration on the tool timescale. Another electrochemical simulation follows, and the process repeated until the desired tool movements are completed. In essence, each electrochemical simulation provides an estimate of etch rate behavior for a large number ( $\sim 10^9$ ) of pulses not simulated.

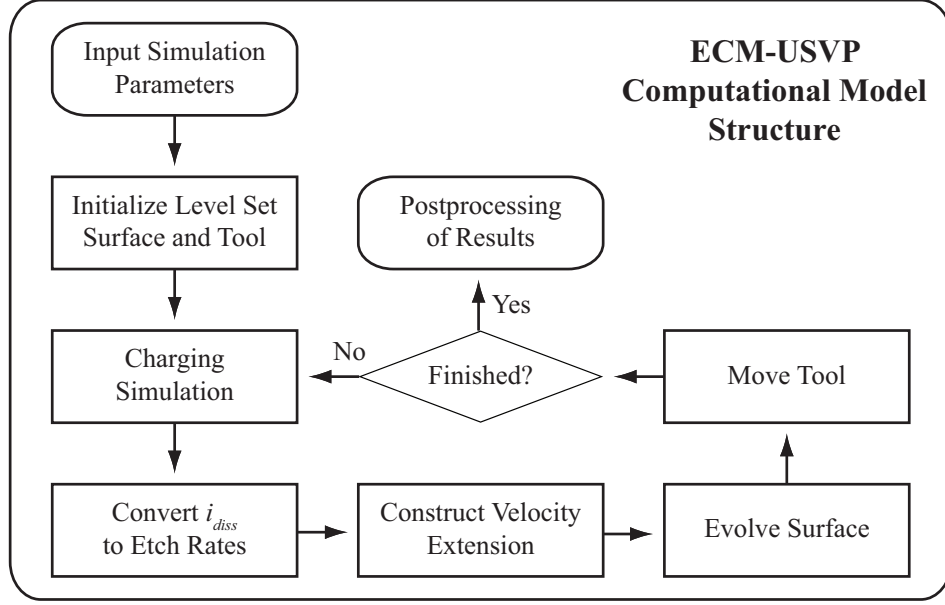


Figure 3.1: Flowchart depicting the major components and linkages for the ECM-USVP Computational Model.

### 3.2.3 Transient Charging Simulation

In order to generate overpotential information for use in determining etch rates, the ECM-USVP system is considered in terms of equivalent circuits, as depicted in Figure 3.2. After a mesh is applied to a domain enclosing regions of the tool, substrate, and electrolyte, nodes in the electrolyte region are connected to each other by resistors, which represent the resistance of the electrolyte. Connections are made to the tool and workpiece surfaces through capacitors in parallel, representing the capacitances of the electrochemical double layers at the respective surfaces. Completing the model, the tool and workpiece are considered as equipotential surfaces, and reflective boundary conditions are used as appropriate.

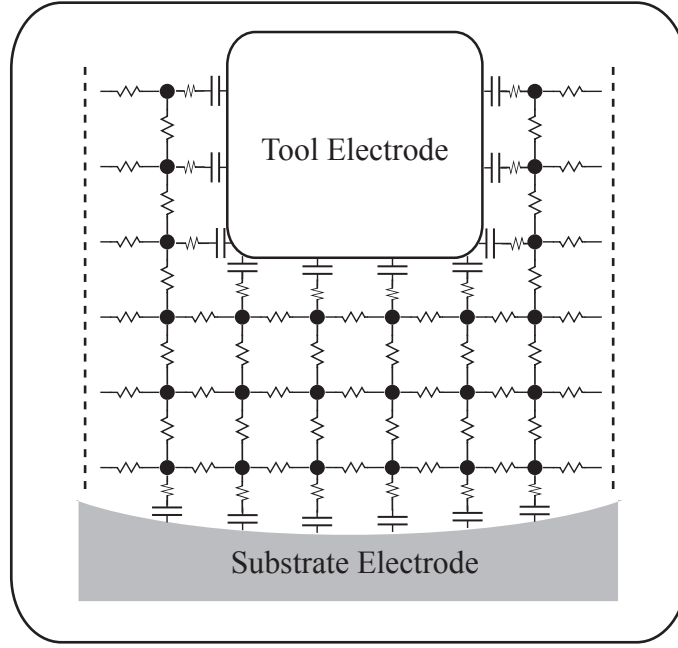


Figure 3.2: Schematic of the equivalent circuit used in the ECM-USVP Computational Model. The electrolyte takes the form of a resistor mesh. Connections are made to the tool and substrate electrodes through capacitors in parallel, representing the double layers at those surfaces. Black dots indicate nodes in the electrolyte where potentials are found during the transient charging simulation. Reflective boundary conditions indicated with dashed lines.

In order to find the initial potential of each node in the electrolyte region upon the application of a voltage pulse to the tool, Kirchoff's Law is applied (sum of currents is zero), generating a system of linear equations. Due to the size of this system, a conjugate gradient technique is used to approximate the solution, thus care must be taken to form a proper positive-definite, symmetric matrix. Assuming a uniform mesh of length  $h$  in both  $x$  and  $y$  directions, for a typical 2D node in the electrolyte away from the tool, workpiece, and

boundaries, the equation may be written

$$\frac{4}{R}\phi_{(x,y)} - \frac{1}{R}\phi_{(x-h,y)} - \frac{1}{R}\phi_{(x+h,y)} - \frac{1}{R}\phi_{(x,y-h)} - \frac{1}{R}\phi_{(x,y+h)} = 0, \quad (3.1)$$

where  $R$  is the unit resistance and each  $\phi$  represents the potential in the appropriate direction, with  $\phi_{x,y}$  the node in question. For nodes near a boundary condition, Equation 3.1 is simplified according to the direction in which the boundary condition is encountered. For a boundary condition in the  $+x$  direction:

$$\frac{3}{R}\phi_{(x,y)} - \frac{1}{R}\phi_{(x-h,y)} - \frac{1}{R}\phi_{(x,y-h)} - \frac{1}{R}\phi_{(x,y+h)} = 0 \quad (3.2)$$

Finally, for nodes adjacent to the tool or workpiece, the resistance between the node and the surface ( $R'$ ) is noted (as this resistance will most likely differ from  $R$  as the length of the connection between node and surface is typically a fraction of the mesh length), and the known potential of the surface incorporated. Thus, for a surface encountered in the  $+y$  direction, Equation 3.1 is rewritten

$$\left(\frac{3}{R} + \frac{1}{R'}\right)\phi_{(x,y)} - \frac{1}{R}\phi_{(x-h,y)} - \frac{1}{R}\phi_{(x+h,y)} - \frac{1}{R}\phi_{(x,y-h)} = \frac{1}{R'}\phi_{Surface} \quad (3.3)$$

Once the initial potential is established at each node, subsequent potentials are found at set intervals during the lengths of the pulse and pause periods. For the pulse period, the form of the equations for the nodes within the bulk electrolyte region and those adjacent to a boundary match those above. For nodes adjacent to the tool and workpiece surfaces, the equations are rewritten to take into account the charge stored in the electrochemical double layer. This charge changes during the time interval based on the local transient current, however, so the situation is simplified using a mean current during the interval, defined as the average of the local transient current at the



beginning and end of the interval. The proper form can be generated by the following equation:

$$\phi_{DL,i+1} = \phi_{DL,i} + \frac{\left[ \frac{(\phi_{(x,y),i+1} - \phi_{DL,i+1})}{R'} + \frac{(\phi_{(x,y),i} - \phi_{DL,i})}{R'} \right]}{2} \left( \frac{\Delta t}{C_d} \right), \quad (3.4)$$

where  $\phi_{DL}$  is the potential at the interface between the double layer and the electrolyte,  $\Delta t$  is the time step,  $C_d$  is the capacitance of the double layer, and the  $i$  and  $i+1$  subscripts indicate the known values at time step  $i$  and unknown values at time step  $i+1$ . To insure the appropriate form for a positive-definite symmetric matrix, the form of Equation 3.3 must first be modified. Again, for a surface encountered in the  $+y$  direction, the expression becomes

$$\left( \frac{3}{R} + \frac{1}{R'} \right) \phi_{(x,y)} - \frac{1}{R} \phi_{(x-h,y)} - \frac{1}{R} \phi_{(x+h,y)} - \frac{1}{R} \phi_{(x,y-h)} - \frac{1}{R'} \phi_{DL} = 0 \quad (3.5)$$

Thus it is required that the coefficient of the  $\phi_{(x,y),i+1}$  term to be  $-1/R'$  in Equation 3.4. Rearranging gives

$$-\frac{1}{R'} \phi_{(x,y),i+1} + \frac{1}{R'} \left( 1 + \frac{2R'C_d}{\Delta t} \right) \phi_{DL,i+1} = \frac{1}{R'} \left[ \phi_{(x,y),i} + \left( -1 + \frac{2R'C_d}{\Delta t} \right) \phi_{DL,i} \right] \quad (3.6)$$

The discharging of the double layers during the pause period follows a similar treatment. The initial potentials upon the discontinuation of the pulse are found at each node in the electrolyte relative to the potentials of the charges stored in the double layer capacitors. Here, the potentials at the capacitors are redefined based on their potentials at the end of the pulse and the potentials of their respective surfaces to account for their charge accumulation,  $\phi'_{DL} = \phi_{DL} - \phi_{Surface}$ . These new capacitor potentials are equivalent to the surface potentials in Equation 3.3 for calculating the initial potentials in the bulk

electrolyte, thus Equation 3.3 and its equivalents are modified following the form below:

$$\left(\frac{3}{R} + \frac{1}{R'}\right) \phi_{(x,y)} - \frac{1}{R} \phi_{(x-h,y)} - \frac{1}{R} \phi_{(x+h,y)} - \frac{1}{R} \phi_{(x,y-h)} = \frac{1}{R'} \phi'_{DL} \quad (3.7)$$

The stored charge, and hence the potential, of each capacitor is reduced as current flows. Treatments follow directly from Equations 3.5 and 3.6 above with the proper substitution of  $\phi'_{DL}$ , noting that  $\phi'_{DL}$  will be a variable in these equations rather than appearing as a constant as in Equation 3.7. Here it is also noted that nodes adjacent to multiple boundary conditions and/or capacitors are handled by modifying the bulk electrolyte form of Equation 3.1 for each special case. For example, a node with a boundary condition in the  $+y$  direction and a capacitor in the  $-x$  direction would have the form

$$\left(\frac{2}{R} + \frac{1}{R'}\right) \phi_{(x,y)} - \frac{1}{R} \phi_{(x+h,y)} - \frac{1}{R} \phi_{(x,y-h)} - \frac{1}{R'} \phi_{DL} = 0 \quad (3.8)$$

during the pulse. Extending into 3D follows the above formulae, with the addition of  $\pm z$  direction terms.

As mentioned above, the conjugate gradient method [27] is used to solve the system of equations generated. It is an iterative method applicable to symmetric, positive-definite matrices, primarily for sparse systems with a large number of unknowns. Because it does not modify matrices like direct methods, storage complexity can be minimized from  $\mathcal{O}(n^2)$  to  $\mathcal{O}(n)$ . Time complexity is estimated as  $\mathcal{O}(n^{3/2})$  for 2D systems and  $\mathcal{O}(n^{4/3})$  for 3D [67]. These compare favorably with other methods used on sparse matrices such as the iterative method of steepest descent ( $\mathcal{O}(n^2)$  and  $\mathcal{O}(n^{5/3})$  for 2D and 3D, respectively) and the direct Cholesky decomposition ( $\mathcal{O}(n^3)$  for both cases) [61].

A Jacobi preconditioner is also used to increase computational speed moderately [67]. More complex preconditioning strategies were not considered, as the form of matrix changes during from pulse to pulse (one pulse typically involves solving a system with the same matrix and different product vector  $\sim 20$  times). This is another reason not to use a method such as LU-decomposition, beyond the storage requirement.

For each time step during the transient charging simulation, overpotential information for each capacitor is stored. These values are then used with the anodic Tafel form (Equation 2.7) to find the transient dissolution current. Integrating over the length of the pulse and normalizing by the total length of the pulse and pause periods then yields the average dissolution current for each capacitor.

### 3.2.4 Profile Evolution

Both 2D and 3D feature profile evolution tools have been developed using the above transient charging model to generate etch rates. The 2D tool can be used to describe vertical etching into the workpiece or lateral etching of the workpiece in a plane parallel to the initial workpiece surface, as would occur when forming a deep trench. For vertical etching, comparisons of the etch resolutions at the workpiece surface and along the etch depth of the tool can be made as well as a description of the corresponding sloping of the sidewalls and sharpness of the corners of etched features. With the lateral etching model, in addition to capturing the features of the etched plane, trends in etch resolution as a function of pulse duration and other system parameters can be found for a fully 2D region.

The 3D tool has been designed to accommodate any sequence of mo-

tions of the tool in the  $x$ ,  $y$ , and  $z$  directions, with movement in multiple directions simultaneously. It also allows for the specification of any desired tool electrode shape. As such, it should be able to mimic any ECM-USVP machining application. In addition, with selective use of the reflective boundary conditions, multi-tool electrode arrays can be simulated.

All forms of the profile evolution tool follow the same general algorithm. The tool and surface locations are used to form the simulation domain for the charging simulation (as the discharge during the pause period does not contribute to the modification of the tool or workpiece, it is ignored). Following the charging simulation, the average dissolution currents at each capacitor are then compared to a dissolution current for which the etch rate is known (obtained earlier through an iterative process to match an experimental resolution). The surface is then evolved for a set duration (with care taken to insure the surface moves less than one-half of a mesh length in any given time step), and the tool is moved as appropriate. This overall process is repeated until the desired tool movements have been completed.

The level set method [66] was chosen for interface tracking as this technique allows for robust handling of complicated etch features as well as simple manipulation of surface properties. This is particularly important for accurately estimating the resistances of connections to the workpiece from nodes in the electrolyte. In addition, the ability to resolve the properties of features at sizes below the length of the mesh allows for the use of less dense meshes, significantly increasing computational speed and allowing for the extension of this model into three dimensions. A final benefit is the ease with which the level set technique handles the merging of surface features such as occurs with holes being etched in close proximity.

The formulation of the level set mathematically is relatively straightforward. For a given surface which evolves  $\Gamma(t)$ , a level set function is defined such that its value is equal to 0 at locations on the surface and nonzero otherwise, for all  $t$ . A typical choice for the function is a signed distance function, where each point  $x \in R^N$  is assigned a value equal to its distance to the surface, with the sign distinguishing between inside(-) and outside(+). Assuming the initial surface  $\Gamma(t = 0)$  is available, one can easily initialize the level set function:

$$\varphi(x, t = 0) = \pm d \quad (3.9)$$

Next, the path of each point on the initial surface is tracked as it evolves with time, giving a series of points  $x(t)$  for each, with the caveat that the path of each point is always normal to the surface as it evolves. Thus,

$$x'(t) \cdot n = F(x(t)), \quad (3.10)$$

where  $x'(t)$  is a vector for each point giving the outward normal velocity,  $n$  is its outward normal vector, and  $F(x(t))$  is the scalar speed in the outward normal direction of point  $x$  at time  $t$ . Now, using the definition of the level set,

$$\varphi(x(t), t) = 0 \quad (3.11)$$

Differentiating with respect to the chain rule gives

$$\varphi_t + \nabla \varphi(x(t), t) \cdot x'(t) = 0 \quad (3.12)$$

As  $n = \nabla \varphi / |\nabla \varphi|$ , Equation 3.12 can be rewritten and combined with the initial condition to give

$$\begin{aligned} \varphi_t + |\nabla \varphi| F &= 0 \\ \text{given } \varphi(x, t = 0), \end{aligned} \quad (3.13)$$

and thus the evolution of  $\Gamma$  can be determined.

As a practical matter, the level set method requires the outward normal speed  $F$  to be defined at all nodal points, not merely those along the front of the evolving surface. This may require extending the velocity away from the front in problems where non-interfacial regions do not have a physical interpretation for velocity. Various schemes have been developed for calculating these extension velocities ( $F_{ext}$ ), with simple averaging schemes often used. In some cases, this can lead to errors which fail to preserve the signed distance function at regions away from the front. These errors propagate toward the front with the  $|\nabla\varphi|$  term, eventually resulting in a requirement to reinitialize the signed distance function and most likely causing loss of mass. To overcome this problem, a method of extending velocities has been developed which assures the signed distance function remains valid in regions away from the front [3], using:

$$\nabla F_{ext} \cdot \nabla \varphi = 0 \quad (3.14)$$

In order to increase the speed of the level set calculations, the narrow band method [2] has been implemented. In this technique, only nodes falling within a certain range of the surface are updated, usually a range of 6-10 nodes on either side. As the surface moves toward the edge of the narrow band, marker points located 2-4 points inward from the edge act as landmines, initiating an update of the narrow band structure. This results in a reduction in time complexity from  $\mathcal{O}(n^2)$  to  $\mathcal{O}(nk)$  when evolving the surface, where  $k$  is the width of the band. The narrow band also requires reinitialization steps of  $\mathcal{O}(nk^2)$ , but they are infrequent enough that the evolution steps still dominate processing time within the method. Space complexity can be reduced to as low as  $\mathcal{O}(nk)$  from  $\mathcal{O}(n^2)$ .

# Chapter 4

## Simulation Results: ECM with Ultrashort Voltage Pulses

As with many modeling processes, the strategy used here is to evaluate the performance of the model against known experimental values before using the model for predictive purposes. To that end, comparisons are made with the transient current response [63] and the machining resolution [72]. Alongside these results are a discussion of the nature of the overpotential and dissolution current during the pulse period, examples of etch profiles from both 2D and 3D simulations, and a theoretical treatment of the relationships between pulse duration, tool diameter, and resolution. This is followed by an illustration of the predictive capabilities of the computational model when used with complex multi-tip tool arrays.

Much of the work in this chapter has been published previously [31–33, 35].

### 4.1 Transient Current Response

Schuster *et al.* [63] reported the transient current response of a single voltage pulse when first demonstrating the ECM-USVP technique. A tool electrode was held at separations ranging from less than 1 to 20  $\mu\text{m}$  from an unmodified substrate electrode, and a -1.6 V pulse was applied to the tool

for 50 ns, followed by an off-period of 500 ns. The electrolyte composition was not specified, nor the tool diameter. Measurements obtained indicated a rapid decay in the direct current during the pulse for separations at or below 1  $\mu\text{m}$ . At a separation of 20  $\mu\text{m}$ , the current decayed slowly. During the off-period, a large reverse current was found for the smaller separations, with a negligible current for the separation of 20  $\mu\text{m}$ . These findings were attributed to the charging and subsequent discharge of the double layers at the tool and substrate for the small separations.

Due to the difficult geometry involved, computational studies focused on separations of 1, 2, and 10  $\mu\text{m}$ , using a 10  $\mu\text{m}$  diameter tool. A resistivity of 30  $\Omega\cdot\text{cm}$  was selected in the absence of electrolyte information, a value typical for the electrolytes used in ECM-USVP. The capacity of the double layers was also set to a typical value, 10  $\mu\text{F}/\text{cm}^2$ .

Both 2D and 3D simulations of the transient current were performed, with similar results. For the 2D case, a cross-section of the cylindrical tool was considered, giving it the appearance of a rectangle. The domain was set at a width of 50  $\mu\text{m}$ , centered on the tool center, and extended from the substrate surface to a height of at 40  $\mu\text{m}$  above it. The mesh applied to the domain had a spacing of 0.2  $\mu\text{m}$  in both dimensions, putting a total number of nodes in the electrolyte at  $\sim 40,000$  after removing locations occupied by the tool. The 50 ns pulse duration was broken into 20 time steps, a common feature of all the simulations contained herein. The form of the pulse was a boxcar function; upon application of the pulse, the tool electrode immediately reached the full applied voltage and remained there until the end of the pulse, at which time it immediately returned to zero. This differs from the pulse generator used in the experiment, which required  $\sim 5$  ns of ramping to achieve the full applied



potential as well as return the potential to zero. This difference is relevant when comparing the transient currents, as the peaking of the current at the initial charging and discharging stages will be much larger for the simulation. The decision was made not to attempt to match the performance of the pulse generator from this experiment as it would have limited applicability to other ECM-USVP systems or even to the same system when using a different pulse duration. For this simulation, the discharge behavior was also calculated, using the same 2.5 ns time step for 500 ns of off-time.

For the 3D case, the same time steps and tool diameter were used, although naturally with a true cylindrical geometry. Due to the increased memory requirements of the extra dimension, the domain used was smaller, ranging 40  $\mu\text{m}$  in both dimensions parallel to the flat substrate surface, and 20  $\mu\text{m}$  above it, with the parallel dimensions centered on the tool. The mesh size was also increased to 0.33  $\mu\text{m}$  in all dimensions, giving  $\sim 800,000$  nodes.

Figure 4.1 contains comparisons of the transient current responses for different tool-substrate separations, using both the 2D and 3D models. For the 2D case, the data are plotted on a relative basis, normalized by the average current density upon the initial application of the pulse. For the 3D case, the absolute values of the currents are smaller than those reported experimentally by roughly two orders of magnitude. This is most likely explained by a difference in the tool diameter used and its effect on the overall surface area available to transfer current, as tool diameters used in accompanying experiments ranged from 10 to 50  $\mu\text{m}$ . A 50  $\mu\text{m}$  tool could likely give an increase of well over an order of magnitude relative to that of the 10  $\mu\text{m}$  tool used computationally, taking into account increased surface area both within the computational domain and outside of it. However, the difficulty in creating

an adequate mesh for the combination of such a large tool electrode and small separation prevented testing of this hypothesis. Both 2D and 3D models exhibit decays in the transient current and varying levels of discharge current consistent with the charging and discharging behavior seen in the ECM-USVP experimental system, with the decay slightly more rapid in the 2D case. Due to these results, no modifications were made to the charging simulation when used subsequently in the profile evolution simulation.

## 4.2 Overpotential and Dissolution Current Evolution

Additional 2D simulations were performed in order to look at how the overpotential and dissolution current evolve during the pulse period. Simulation parameters and the domain size, mesh, and geometry matched those of the above transient current studies, with separations between tool and substrate of 1, 3, 5, and 10  $\mu\text{m}$ . The results give additional insight into the localization of the modification of the substrate during etch conditions.

The evolution of the overpotential is illustrated in Figure 4.2. Here the range of  $-5 \leq x \leq 5$  represents the region of the substrate shadowed by the tool. It is apparent that the evolution of the overpotential is more pronounced in this region at all separations, but the degree to which this is exhibited varies significantly. At 1  $\mu\text{m}$  of separation, the overpotential maintains an almost uniform level in the shadowed region throughout the pulse. This gives way to a peaking and gradual decline for a separations of 3 and 5  $\mu\text{m}$ . At 10  $\mu\text{m}$  very little peaking is evident as very little overpotential has accumulated even by the end of the pulse. For all separations there is some level of overpotential at the edges of the domain ( $\sim 0.1$  V), which is a mixture of the naturally occurring evolution and possible contributions from the mirrored tool arising from the

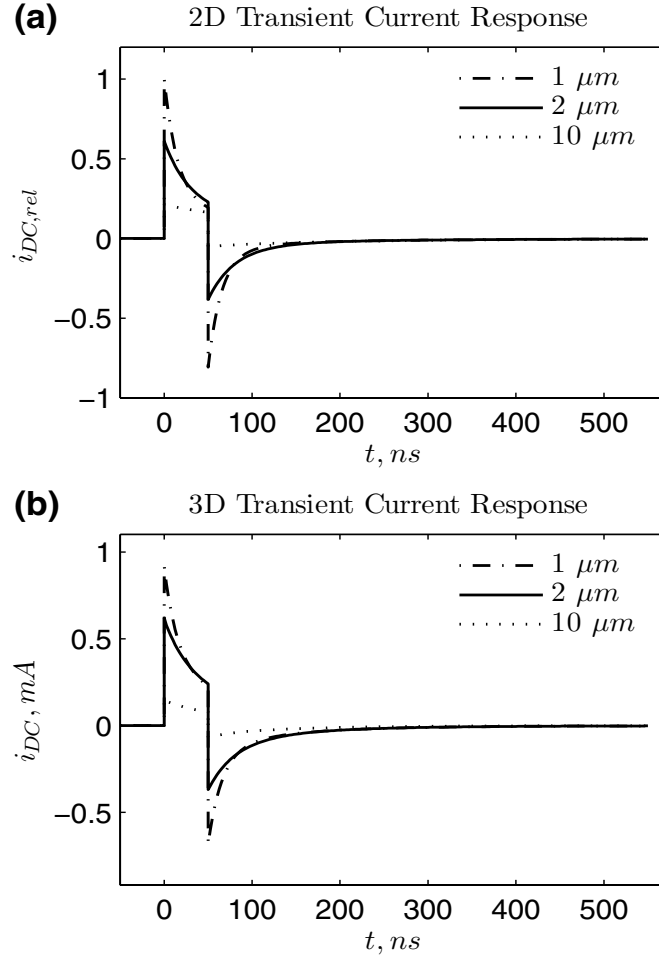


Figure 4.1: Transient current response during one 50:500 ns pulse:pause period for (a) 2D and (b) 3D computational models.

reflective boundary conditions.

A similar treatment of the dissolution current is given in Figure 4.3, using the anodic Tafel equation (Equation 2.7). For these calculations, the transfer coefficient  $\alpha$  is set equal to 0.5 (indicating a symmetric energy barrier between oxidation and reduction, an appropriate choice in the absence of experimental information [14]), and all values are made relative to the maximum value occurring at a separation of 1  $\mu\text{m}$ . Here the exponential nature of the dissolution current with overpotential is made apparent, as the gradual declines in the overpotential treatment become sharp cutoffs between regions of significant dissolution current and those without for the smaller separations. Significant etching outside of the shadowed region only occurs at a separation of 10  $\mu\text{m}$ , and that only in a relative sense. Beyond demonstrating this localization of the etching, the behavior shown precludes the possibility of artifacts arising from the use of reflective boundaries, provided a large enough domain is chosen.

### 4.3 Lateral Etch Resolution

Hudson *et al.* [72] reported on the relationship between pulse duration, electrolyte strength, and etch resolution in ECM-USVP. In their experiments, a tool was first etched vertically into the substrate to a depth of 5  $\mu\text{m}$ , then moved laterally along the surface until a steady-state gap width was found in the wake of the tool. For these studies, pulse durations ranged from 10 to 100 ns, and the electrolyte consisted of 0.1 M  $\text{CuSO}_4$  mixed with  $\text{H}_2\text{SO}_4$  in concentrations varying from 0.01 M ( $\rho \sim 85 \Omega\cdot\text{cm}$ ) to 0.075 M ( $\rho \sim 30 \Omega\cdot\text{cm}$ ). Their findings indicated a linear increase in resolution with pulse duration for each electrolyte composition, with resolutions ranging from  $\sim 1$  to above

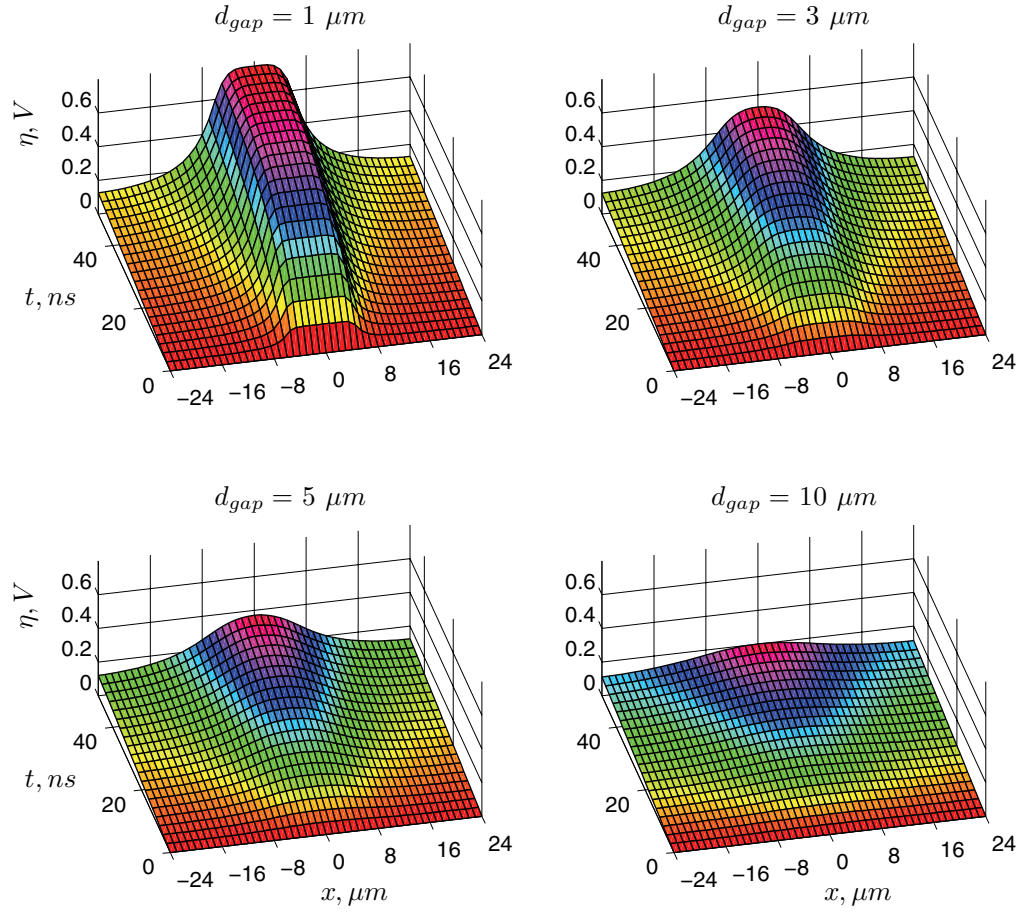


Figure 4.2: Evolution of the overpotential along the substrate for a 50 ns, -1.6 V pulse and the indicated tool-substrate separations. Tool diameter is  $10 \mu m$ .

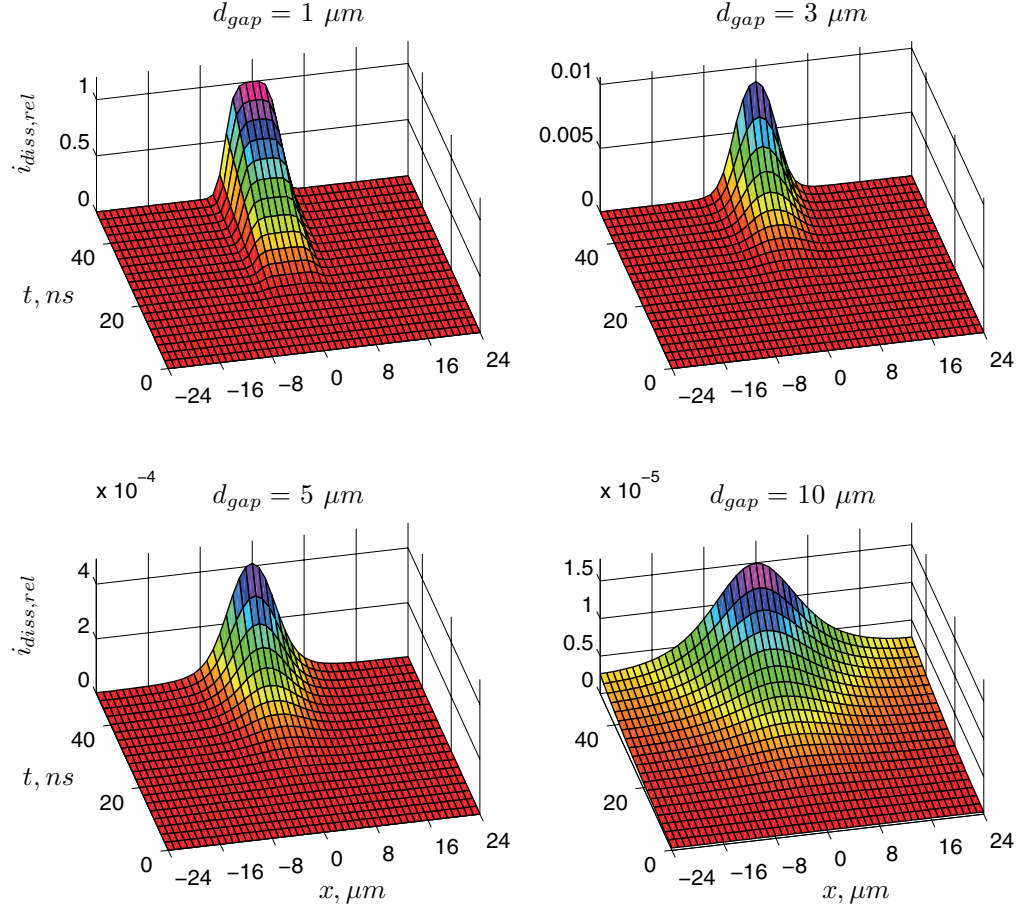


Figure 4.3: Evolution of the dissolution current along the substrate for a 50 ns, -1.6 V pulse and the indicated tool-substrate separations. Tool diameter is 10  $\mu m$ . All values are normalized by the largest value obtained at a separation of 1  $\mu m$ .

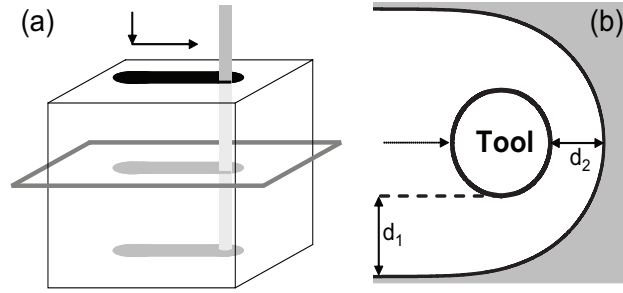


Figure 4.4: (a) Machining system used to measure resolution. 2D region used in computational model indicated by plane. (b) Definition of resolution ( $d_1$ ) and gap space at the leading edge of the tool ( $d_2$ ).

12  $\mu\text{m}$ .

#### 4.3.1 2D Computational Model Calculations

The lateral etch process was first modeled using 2D simulations (see schematic in Figure 4.4) with small diameter ( $\leq 10 \mu\text{m}$ ) tools and a resistivity measuring that of the strongest electrolyte used experimentally. This failed to capture the experimentally-observed linear trend in etch resolution with pulse duration, instead giving sub-linear behavior. Subsequent 2D simulations with larger tools, however, gave behavior which more closely matched that observed experimentally, approaching linearity for a tool diameter of 40  $\mu\text{m}$ . Thus it was determined that the size of the tool had significant impact on the etch resolution.

The 2D computational resolutions and the accompanying ratios of resolutions normalized by that of a 25 ns pulse are given in Figure 4.5 for several tool diameters. The data were obtained through use of parameters matching experimental values when given and otherwise substituting typical values. In

all cases, a resistivity of  $27.7 \Omega\cdot\text{cm}$  was used for the electrolyte, matching that of a  $0.1 \text{ M CuSO}_4/0.075 \text{ M H}_2\text{SO}_4$  mixture (see Appendix C for calculation details). Also from the experiment were the tool speed ( $1.5 \mu\text{m}/\text{min}$ ) and applied potential ( $-2.3 \text{ V}$ ). The capacity was set at  $10 \mu\text{F}/\text{cm}^2$  at both electrodes.

For all calculations, a mesh length of  $0.5 \mu\text{m}$  was used for both charging simulations and profile evolution, with domains of the former ranging  $25 \mu\text{m}$  from the tool in all directions (although in most cases a large portion of this range was within the body of an electrode). As the tool was moved laterally  $100 \mu\text{m}$  to insure a steady-state resolution was reached, narrow banding was employed for the level set calculations, with 6 nodes on either side of the interface. The resulting etch profiles are given in Figure 4.6 for a  $5 \mu\text{m}$  diameter tool.

Prior to obtaining the results, an iterative process was used to determine the relationship between the dissolution current and surface velocities for the level set calculations, in effect an attempt to determine the exchange current density,  $i_0$ . These calculations were performed with a  $40 \mu\text{m}$  diameter tool, as its behavior most closely resembled linear behavior, and were designed to match the etch resolution reported for a  $25 \text{ ns}$  pulse. Following the determination of this parameter, all subsequent 2D calculations used this value.

### 4.3.2 2D Theory

A theoretical analysis of a 2D stationary system (no tool movement) explains in large part the observed trends in the computational model. Here a fixed cylindrical tool is considered, located within a substrate in a concentric arrangement, with electrolyte in the annular region. The resolution is now



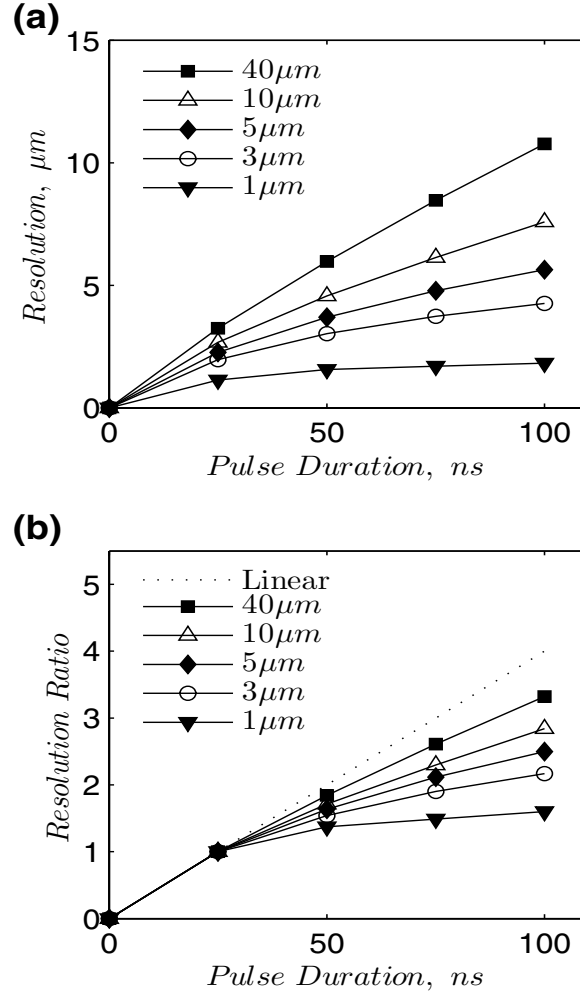


Figure 4.5: (a) 2D etch resolutions with pulse duration for a lateral etching process using the indicated tool diameters. (b) Ratios of the 2D resolutions relative to those obtained at 25 ns for each tool diameter. Degree of sub-linearity increases with decreasing tool diameter.

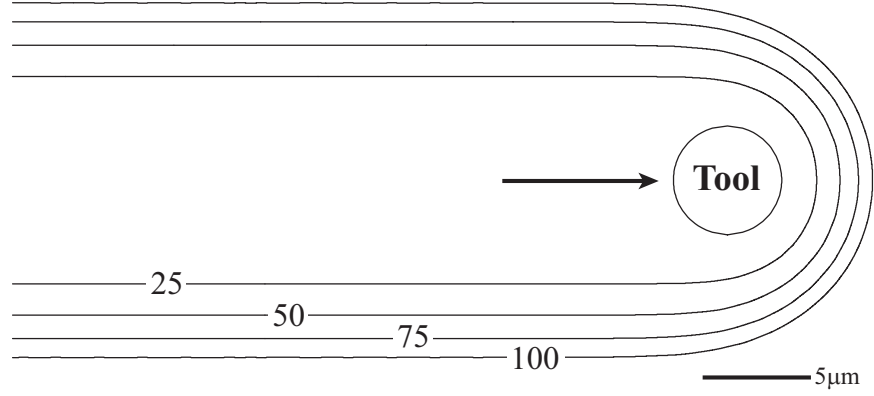


Figure 4.6: Profile evolution of a lateral etch of the substrate by a 5  $\mu\text{m}$  diameter tool moving at 1.5  $\mu\text{m}/\text{min}$ . Pulse durations as indicated (ns)

defined as the width of the annular region,  $r_2 - r_1$ , where  $r_2$  is the radius at which the substrate region begins and  $r_1$  is the radius of the tool (see schematic, Figure 4.7). For any such system, the etch rate can be found as in the computational system by first deriving the evolution of the overpotential at the substrate surface, then integrating the resulting dissolution current and normalizing by the pulse-pause cycle length. For the model system, an applied potential  $E$  is considered, with a pulse duration of length  $t$ . At any time, the applied potential is equal to the resistive potential of the electrolyte plus the overpotentials at the tool ( $\eta_1$ ) and substrate ( $\eta_2$ ):

$$E = \frac{dq}{dt}R + \eta_1 + \eta_2, \quad (4.1)$$

where  $q$  is charge and  $R$  is the electrolyte resistance. For a constant capacity  $C_d$  at both surfaces and electrolyte resistivity  $\rho$ , further substitution obtains

$$E = \frac{dq}{dt} \frac{\rho}{2\pi z} \ln \frac{r_2}{r_1} + \frac{q}{2\pi C_d z r_1} + \frac{q}{2\pi C_d z r_2}, \quad (4.2)$$

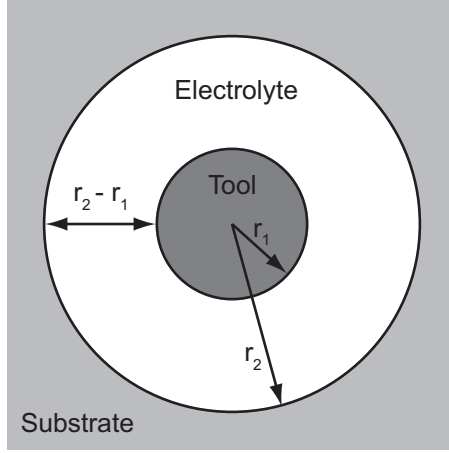


Figure 4.7: Schematic of the geometry used in the 2D stationary system. Resolution is indicated by the quantity  $r_2 - r_1$ .

with  $z$  an arbitrary system height. Solution and rearrangement of the above equation gives

$$\eta_2 = \frac{Er_1}{r_1 + r_2} \left\{ 1 - \exp \left[ -\frac{t}{\rho C_d \ln \left( \frac{r_2}{r_1} \right) \frac{r_1 r_2}{r_1 + r_2}} \right] \right\} \quad (4.3)$$

This overpotential information is then incorporated into the anodic Tafel equation (Equation 2.7) to obtain the transient dissolution current  $i_{diss}$ . Integration and normalization of the subsequent equation as described above results in the expression for average dissolution current,  $\bar{i}_{diss}$ , which is proportional to the etch rate:

$$\bar{i}_{diss} = \frac{\int_0^t i_0 \exp \left( \frac{(1-\alpha)F}{RT} \frac{Er_1}{r_1 + r_2} \left\{ 1 - \exp \left[ -\frac{t}{\rho C_d \ln \left( \frac{r_2}{r_1} \right) \frac{r_1 r_2}{r_1 + r_2}} \right] \right\} \right) dt}{\left( \frac{1}{m} + 1 \right) t}, \quad (4.4)$$

where  $m$  is the pulse-to-pause ratio.

In Figure 4.8(a), the resolutions of stationary two-dimensional systems of varying tool radii and pulse durations are shown. In this case, resolutions were found at each tool radius and pulse duration combination by matching the etch rate characteristics of the computational model in the region near the leading edge of the moving tool: a steady-state etch rate of  $1.5 \mu\text{m}/\text{min}$  (matching that of the tool) for a tool of radius  $5 \mu\text{m}$ , 25 ns pulse, and 1:10 pulse-to-pause ratio, giving rise to a separation of  $1.83 \mu\text{m}$  between the leading edge of the tool and the substrate [ $d_2$  in Figure 4.4(b)]. Despite the differences in substrate geometries, the resolutions given here closely match the separations between the leading edge of the tool and substrate for the computational model. For pulse durations of 50 ns or less, deviations are below 6% over the range of tool radii, owing to similar curvatures of the substrates. With longer pulse durations, the deviations for smaller tool radii increase, but still remain below 13%. Due to this similarity, the stationary model can be used to gain insight into etching trends for regions with significant etch rates.

In Figure 4.8(b), the ratios of the above stationary resolutions to their respective pulse durations are shown, normalized by the limiting value at a pulse duration of 0 for the respective tool radius. Thus, regions where the normalized ratios approach a value of 1 see a nearly linear increase in resolution with pulse duration. As with the computational model, this occurs primarily in regions where the ratio of the resolution to the tool radius is small, such as for large tool radii or short pulse durations. In these regions, the system acts as a one-dimensional system, for which the linear relationship can easily be derived following the above treatment for the stationary two-dimensional case. Here, it is assumed the overpotentials at the tool and substrate are equivalent

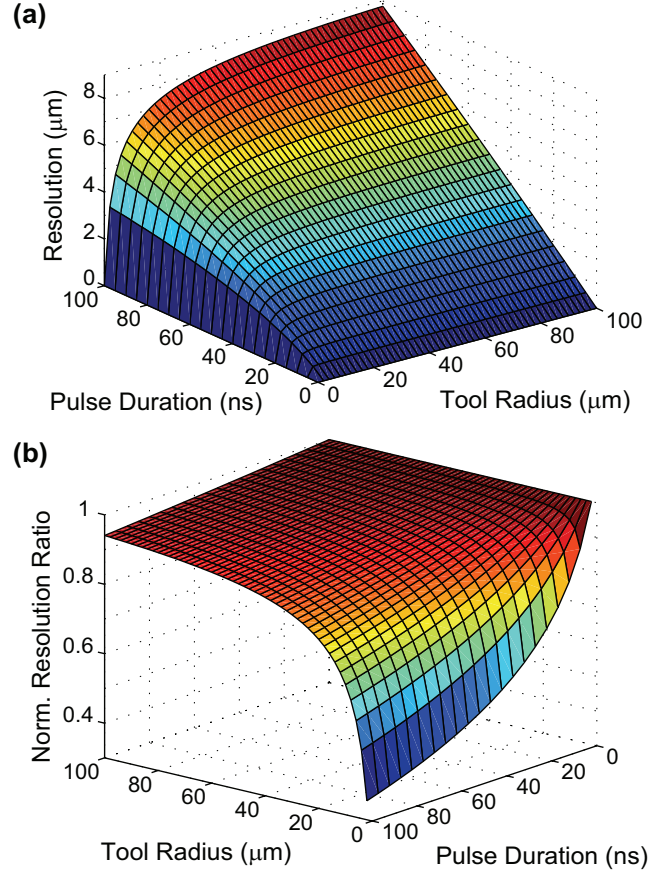


Figure 4.8: (a) Etch resolutions derived from a stationary two-dimensional model as a function of tool radius and pulse duration. (b) Ratio of etch resolution to pulse duration, normalized by limiting values at pulse durations of 0, for stationary two-dimensional model. Value of 1 indicates a linear increase in resolution with pulse duration.

and the resolution is of length  $x$ , giving

$$E = \frac{dq}{dt} \frac{\rho x}{yz} + \frac{2q}{C_d yz} \quad (4.5)$$

where  $y$  and  $z$  are arbitrary system dimensions. The evolution of the overpotential is then given by

$$\eta = \frac{E}{2} \left[ 1 - \exp \left( -\frac{2t}{\rho C_d x} \right) \right] \quad (4.6)$$

for which the following average dissolution current expression is obtained:

$$\bar{i}_{diss} = \frac{\int_0^t i_0 \exp \left\{ \frac{(1-\alpha)F}{RT} \frac{E}{2} \left[ 1 - \exp \left( -\frac{2t}{\rho C_d x} \right) \right] \right\} dt}{\left( \frac{1}{m} + 1 \right) t} \quad (4.7)$$

If a similar system with pulse duration  $nt$  and resolution  $nx$  is considered, the etch rates are found equivalent, and thus resolution scales linearly with pulse duration:

$$\frac{\int_0^t i_0 \exp \left\{ \frac{(1-\alpha)F}{RT} \frac{E}{2} \left[ 1 - \exp \left( -\frac{2t}{\rho C_d x} \right) \right] \right\} dt}{\left( \frac{1}{m} + 1 \right) t} = \frac{\int_0^{nt} i_0 \exp \left\{ \frac{(1-\alpha)F}{RT} \frac{E}{2} \left[ 1 - \exp \left( -\frac{2t}{\rho C_d nx} \right) \right] \right\} dt}{\left( \frac{1}{m} + 1 \right) nt} \quad (4.8)$$

To achieve a similar linear increase in resolution with pulse duration for a stationary two-dimensional system, the tool radius must also be scaled linearly:

$$\frac{\int_0^t i_0 \exp \left( \frac{(1-\alpha)F}{RT} \frac{Er_1}{r_1+r_2} \left\{ 1 - \exp \left[ -\frac{t}{\rho C_d \ln \left( \frac{r_2}{r_1} \right) \frac{r_1 r_2}{r_1+r_2}} \right] \right\} \right) dt}{\left( \frac{1}{m} + 1 \right) t} = \frac{\int_0^{nt} i_0 \exp \left( \frac{(1-\alpha)F}{RT} \frac{Enr_1}{nr_1+nr_2} \left\{ 1 - \exp \left[ -\frac{t}{\rho C_d \ln \left( \frac{nr_2}{nr_1} \right) \frac{nr_1 nr_2}{nr_1+nr_2}} \right] \right\} \right) dt}{\left( \frac{1}{m} + 1 \right) nt} \quad (4.9)$$

An additional stationary two-dimensional system was used to investigate the etch rate characteristics in regions of low etch rates, such as those at the full resolutions of the computational model [ $d_1$  in Figure 4.4(b)]. A system with the same characteristics as the earlier basis system was used to generate resolution data, only this time the targeted etch rate was that occurring at the full resolution downstream of the tool. Again the stationary model gave similar results to the computational model, generating etch resolutions within 3% for all tool radii above  $0.5\ \mu\text{m}$ . The associated normalized resolution ratios were largely similar to those of the earlier stationary model, with deviations of greater than 5% occurring only at a tool radius of  $0.5\ \mu\text{m}$ .

### 4.3.3 3D Computational Model Calculations

A large reason for the mismatch between computational model and experimental data, besides the lack of information about tool diameter, was the low aspect ratio of the trenches formed. With vertical etching to a depth of only  $5\ \mu\text{m}$  and reported resolutions of over  $12\ \mu\text{m}$ , some of the trenches formed must have aspect ratios at or below  $\sim 0.2$ . Etching under these conditions clearly will result in end effects at both the top and bottom of the trench that cannot be accounted for with a 2D model. In addition, due to rounding of the trench walls under such conditions, the location of the measurement of the resolution can significantly effect the ratio of resolutions at differing pulse durations.

This effect is illustrated in Figure 4.9. A series of 2D vertical etches were made into the substrate surface to a depth of  $5\ \mu\text{m}$ , simulating the initial vertical etch of the tool for the lateral resolution experiment. While this behavior will differ somewhat from the steady-state etching of the tool once

lateral etching has begun, the results provided here are illustrative of the problems with the measurements in low aspect ratio structures. For these simulations, a 5  $\mu\text{m}$  diameter tool and pulse durations ranging from 25 to 100 ns were used. In Figure 4.9(a), the resulting etch profiles are plotted, demonstrating the rounding of the profiles. In Figure 4.9(b), the resulting resolution ratios are plotted as a function of etch depth for the 50, 75, and 100 ns series, normalized by the resolution of the 25 ns pulse. The results vary from sub-linear to super-linear ratios with pulse duration.

These results provided the initial motivation to extend the computational model into three dimensions. Lateral etch simulations were performed with the same electrolyte, capacity, applied potential, pulse:pause ratio, and tool speed as the 2D simulations, for a similar range of pulse durations. Both 10 and 30  $\mu\text{m}$  diameter tools were considered. The simulation domain for the transient charging simulation ranged 72  $\mu\text{m}$  in both  $x$  and  $y$  dimensions, again centered on the tool, and extended above the surface to a height of 20  $\mu\text{m}$ . Due to memory limitations, the mesh size was increased to 0.75  $\mu\text{m}$ , and again narrow banding was employed for the level set calculations, this time with a width of 10 nodes on both sides of the interface. The tool began 10  $\mu\text{m}$  above the unmodified substrate surface, etched into the surface to a depth of 5  $\mu\text{m}$ , and then proceeded laterally a distance of 60  $\mu\text{m}$ . Figure 4.10 gives a sample profile of a lateral etch with a 10  $\mu\text{m}$  diameter tool and pulse duration of 100 ns.

The iterative process was again used to match experimental resolution to that obtained computationally. A 30  $\mu\text{m}$  diameter tool was used in this process, with the target to match the resolution given by a 25 ns pulse with the 0.1 M  $\text{CuSO}_4$ /0.075 M  $\text{H}_2\text{SO}_4$  mixture. This required the selection of a



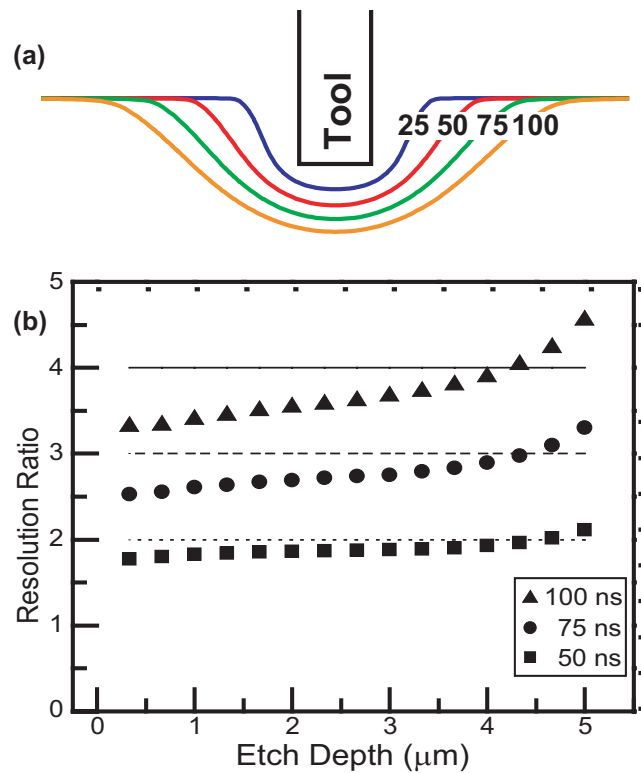


Figure 4.9: (a) Etch profiles for a tool of radius  $2.5 \mu\text{m}$  etched to a depth of  $5 \mu\text{m}$ . Pulse duration as indicated (ns). (b) Etch resolution ratios relative to that of a 25 ns pulse at varying etch depths. Horizontal lines indicate linear behavior.

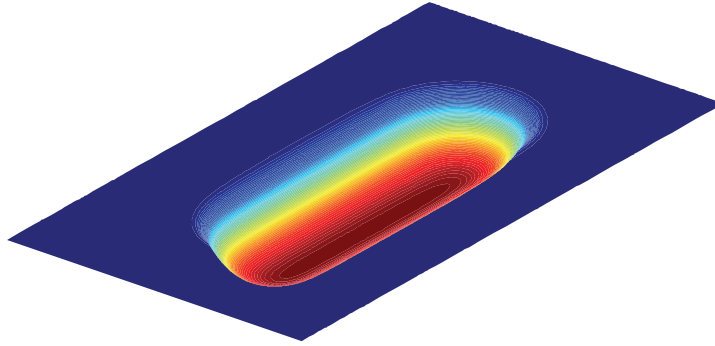


Figure 4.10: Underside of surface etched laterally at a depth of  $5\ \mu\text{m}$  for a distance of  $60\ \mu\text{m}$ . A  $10\ \mu\text{m}$  diameter tool moving at  $1.5\ \mu\text{m}/\text{min}$  was used, along with  $100\ \text{ns}$  pulses of  $-2.3\ \text{V}$  applied to the tool with a 1:10 pulse:pause ratio.

location at which to take the measurement due to the rounding of the profiles. The choice made was the resolution at a depth of  $5\ \mu\text{m}$ , the level of the bottom of the tool during the lateral etch.

Results of the 3D lateral etching simulations are given in Figure 4.11. The trend is similar to that in the 2D simulations. At the larger tool diameter, the resolution more closely resembles linear behavior, while sub-linear behavior occurs when the ratio of the resolution to the tool diameter increases. As a final note, it was subsequently discovered that this effect has been seen experimentally [41] but not quantified.

#### 4.4 Tool Templates

At present, ECM-USVP suffers from limited processing speeds relative to competing technologies for micron-scale processing, such as EDM. This is exacerbated by the nature of the tool electrode and how it is used to create

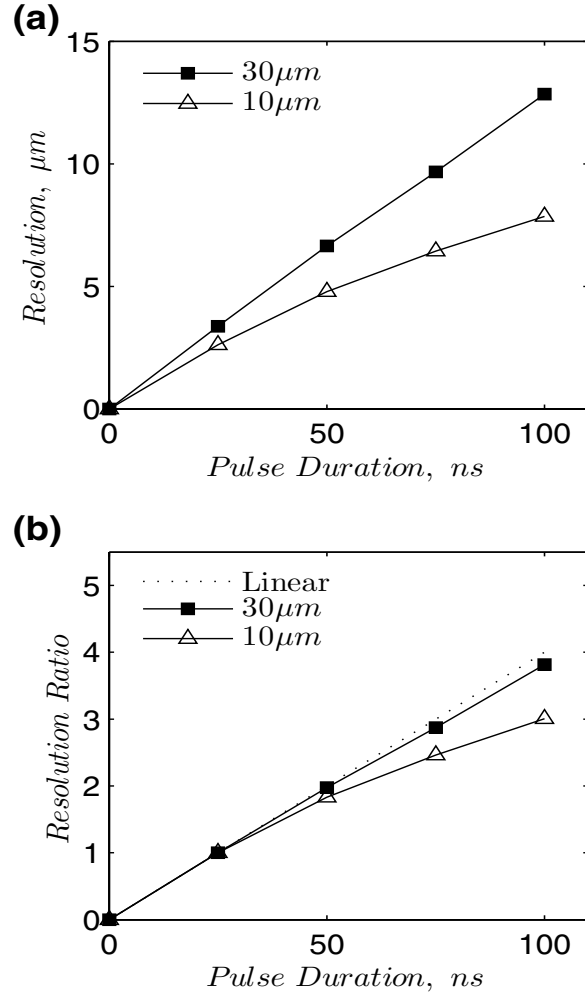


Figure 4.11: (a) 3D etch resolutions with pulse duration for a lateral etching process using the indicated tool diameters. (b) Ratios of the 3D resolutions relative to those obtained at 25 ns for both tool diameters.

patterns in the substrate surface in many experimental systems. At present, the majority of experimental studies employ a simple tool electrode (such as an STM tip) which is used to trace out the entire design in the substrate in series. For many patterns, however, this process could be parallelized with the appropriately-shaped tool template [36, 72]. This approach is made more viable by the lack of degradation of the tool electrode during electrochemical processing but may be hindered by reduced fidelity in the communication of the tool shape to the substrate relative to that of the simple tool electrode.

In order to investigate the use of complex templates for tool electrodes, the etching of two high aspect ratio holes in close proximity to one another was considered, as depicted in Figure 4.12. These holes may be etched by a tool consisting of a single cylinder with two vertical etches in series or in a single etch by a more complex tool consisting of two cylinders with the appropriate spacing, generating the two holes in parallel. Upon simulation of these two methods, however, significant differences in the substrate surface morphologies were noted, particularly when comparing the region lying between the holes. For the series case, little etching occurred in this region unless the holes themselves overlapped—that is, a single hole generated by the tool extended beyond the midpoint between the holes. In contrast, the parallel process often gave rise to significant etching in this region, even when the resolution of a single hole did not contain the midpoint.

To quantify the difference between the parallel and series etch behaviors, the etch depth at the midpoint between the hole centers was compared for a variety of pulse durations and tool separations, as shown in Figure 4.13. Here, tools consisting of one or two  $5\text{ }\mu\text{m}$  diameter cylinders were lowered  $40\text{ }\mu\text{m}$  into a copper substrate under conditions matching the lateral etch systems

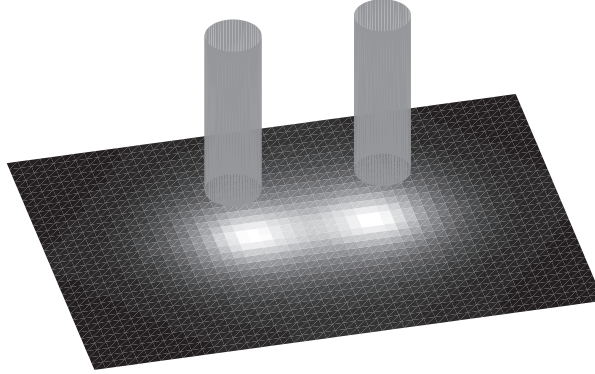


Figure 4.12: Schematic of the parallel etching system.

presented earlier, derived from Hudson *et al.* [72]: a velocity of  $1.5 \mu\text{m}/\text{min}$ ,  $-2.3 \text{ V}$  pulses ranging from 25 to 100 ns, a 1:10 pulse:pause ratio, and a  $0.1 \text{ M CuSO}_4/0.075 \text{ M H}_2\text{SO}_4$  electrolyte solution. In the case of one cylinder, the tool was removed after the initial etch and moved laterally across the substrate surface (both without voltage pulsing), then lowered to a depth of  $40 \mu\text{m}$  a second time under etch conditions. The separation between tools was defined as the minimum distance between the outer circumferences of the tools for the parallel etching case or the analogous minimum distance between the outer circumferences of the initial tool positions for the series cases. It was noted that, for both parallel and series etching, the trend in midpoint etch depth vs. tool separation was the same for all pulse durations: For small separations, the etch depth is roughly equal to the tool etch depth. As the separations get larger, a critical separation is reached at which the etch depth declines rapidly, ultimately leading to no significant etching in the midpoint region.

The disparities in the behaviors become clearer when looking at the

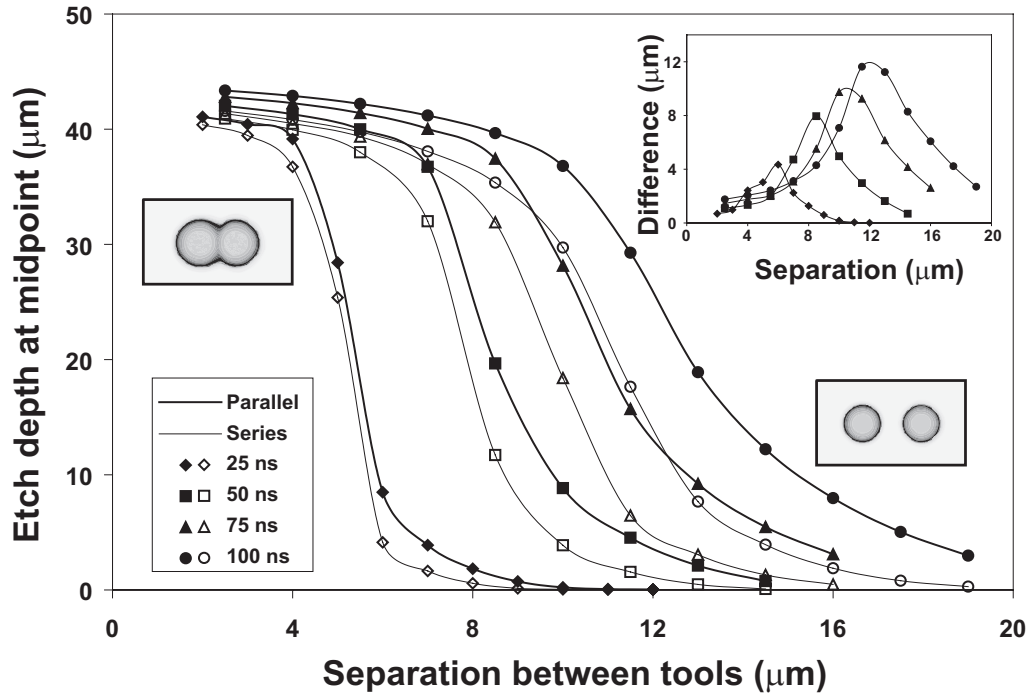


Figure 4.13: Midpoint etch depth vs. tool separation for the parallel and series cases at the indicated pulse durations. Schematics indicate joining and separation of the holes formed at the different tool separations. Inset: Difference in midpoint etch depth (parallel case - series case).

difference in etch depth between the parallel and series cases at the same tool separation, as illustrated in the inset in Figure 4.13. Here it is seen that, for each pulse duration, there was a critical separation between tools at which a maximum disparity was found between the series and parallel etching cases, with both the critical separation and disparity increasing with increasing pulse duration. Thus, as the pulse duration is decreased to allow a smaller resolution and better communication of the tool shape to the substrate surface, the advantage of the series case over the parallel case shifts to tool features in closer proximity to each other, with such an advantage illustrated in Figure 4.14.

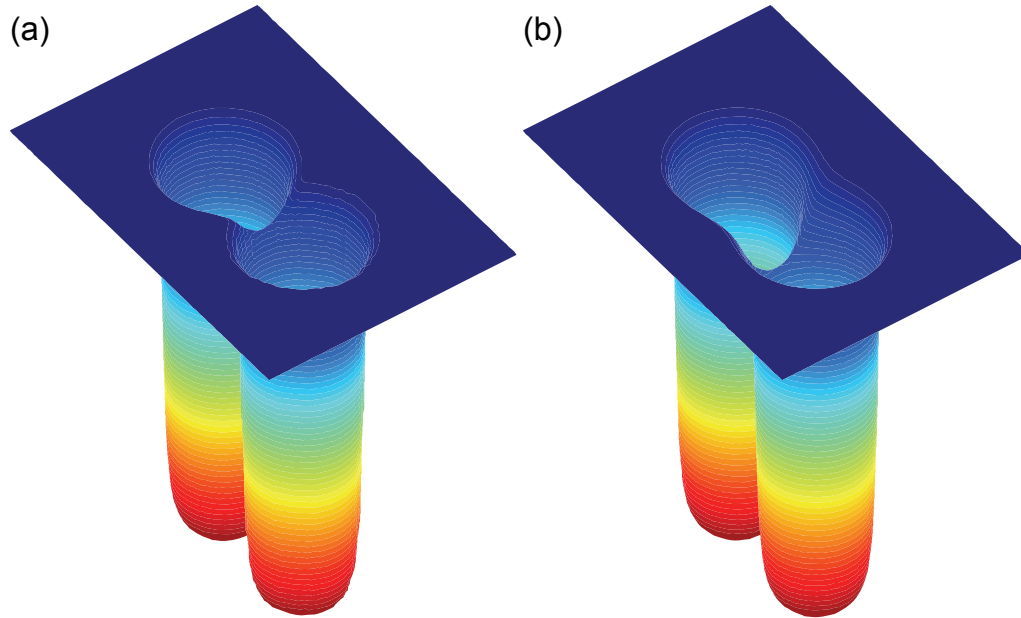


Figure 4.14: Profiles of the resulting holes after etching with 25 ns pulses at a separation of  $6\text{ }\mu\text{m}$ , edge-to-edge, with tool(s) of diameter  $5\text{ }\mu\text{m}$ , for (a) series and (b) parallel cases.

To further understand the different etch behaviors for the two cases, the overpotential on the substrate surface throughout the duration of the pulse was examined, as described in Figure 4.15. For this analysis, a 50 ns pulse and a separation of  $8\text{ }\mu\text{m}$  between tools was chosen, near the critical separation for this pulse duration where any discrepancies between the behaviors should be at a maximum. Two etch conditions were considered: an early stage when the tools had just reached the initial substrate surface and when the tools were  $40\text{ }\mu\text{m}$  below the initial surface (and etching was steady-state). For both conditions, the substrate formed during the parallel etch process was used as a basis and the evolution of the overpotential was calculated for both the parallel and series cases (with the calculations for the two series locations

made individually). The overpotentials at the end of the pulse for the parallel case were then compared with the addition of the overpotentials for the series cases, for both the initial etch (Figure 4.15(a)) and steady-state condition (Figure 4.15(b)). Discrepancies reached a maximum of 0.10 V between the two cases, less than one-sixth of the maximum overpotential for the parallel case, with all differences revealing higher values for the combined series case. Thus, adding the overpotentials of individual tools from the series cases gave approximately the overpotential of the parallel case, with any interaction between the tools resulting in a decreased rather than increased overpotential, relative to the series sum.

A similar analysis for the dissolution current gave markedly different results, as shown in Figure 4.16. Here, the dissolution currents at the end of the pulse for the parallel cases were greater than the addition of their respective series cases in almost all regions. For the initial etch stage (Figure 4.16(a)), this difference was largest at the regions of the substrate shadowed by the tool but was also significant in the region lying between the tools. Once steady-state etching began, however, the difference was largely confined to the area of the substrate between the tools (Figure 4.16(b)). This behavior can be explained by the exponential nature of the dissolution current with respect to the overpotential, following the Tafel model. Assuming that the overpotential for the parallel case was essentially additive of the series cases in all regions, the comparison for the dissolution current was between quantities of the form  $\exp(\eta_{Tool_1} + \eta_{Tool_2})$  and  $\exp(\eta_{Tool_1}) + \exp(\eta_{Tool_2})$  for the parallel and series cases, respectively. Thus, the dissolution current was significantly larger for the parallel case, particularly in those regions having the largest overpotentials, such as those opposite the cylindrical tools and lying between them. As the



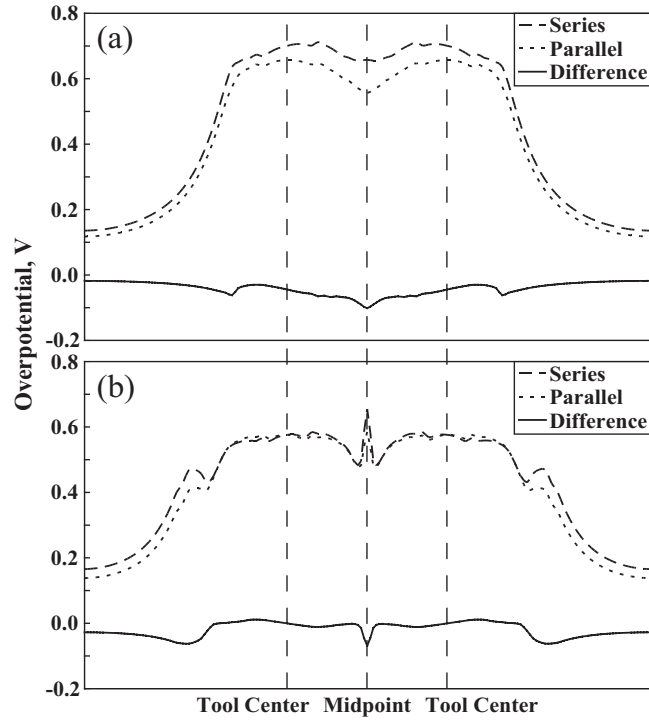


Figure 4.15: Cross sections showing the overpotential at the end of a 50 ns pulse at the substrate surface for tool located at (a) the initial substrate surface and (b)  $40\text{ }\mu\text{m}$  below the initial substrate surface. Tool Separation is  $8\text{ }\mu\text{m}$ . The series overpotential is the sum of the individual tool contributions. The difference is defined as parallel - series.

vertical etching process began, the contribution of one tool to the hole formed by the other was decreased due to the obstruction of the substrate itself, leading to the bottoms of the holes for the parallel case generally matching those of the series case. The region lying between the holes, however, was still affected by phenomenon described above, leading to the increased etching seen for the parallel case.

As larger arrays of tools were considered, the combination of overpoten-

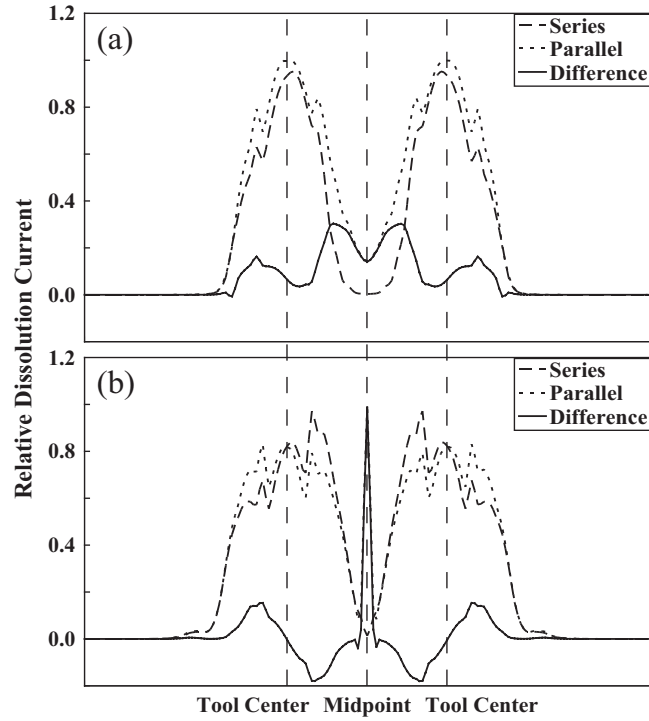


Figure 4.16: Cross sections showing the relative dissolution current at the end of a 50 ns pulse at the substrate surface for tool located at (a) the initial substrate surface and (b)  $40\text{ }\mu\text{m}$  below the initial substrate surface. Tool Separation is  $8\text{ }\mu\text{m}$ . The series dissolution current is the sum of the individual tool contributions. The difference is defined as parallel - series.

tial contributions from individual tools was no longer a good approximation of that generated by the tools in parallel, as illustrated in Figure 4.17(a). Here the overpotential at the end of a 50 ns pulse from an array of  $5\text{ }\mu\text{m}$  diameter tools separated by  $8\text{ }\mu\text{m}$  in both the  $x$  and  $y$  dimensions (simulation surface of size  $13\times 13\text{ }\mu\text{m}$ ) was compared with the combined overpotential of 25 individual tools, each using a simulation surface of size  $65\times 65\text{ }\mu\text{m}$ . For these calculations, an unmodified substrate a distance of  $3\text{ }\mu\text{m}$  from the tool tip(s) was used, and

the 25 individual tools were located to match the locations of the tools of a  $65 \times 65 \mu\text{m}$  portion of the tool array. In all regions, the combined overpotential was larger than that of the parallel case. Further analysis revealed the discrepancies decreased with increasing tool separation, with the system reaching the limiting case of approximately additive behavior at a separation of  $16 \mu\text{m}$  in both  $x$  and  $y$  dimensions. A similar pattern of behavior was observed for a variety of pulse durations and separations between tool(s) and substrate: At small separations between tools in the array, the combined overpotential of individual tools exceeded that of the parallel tool in all regions, while at larger separations the system became additive, and thus  $\eta_{\text{parallel}} \leq \Sigma \eta_{\text{series}}$ .

This behavior of the dissolution current was as before, however, as shown in Figure 4.17(b). Discrepancies in all regions of the simulation domain were in favor of the parallel case over that of the combined series cases. Similar to the overpotential case, further studies indicated these differences decreased as the tool separation increased. This was once again a function of the exponential nature of the dissolution current with regards to the overpotential but was now not so simply deconstructed as the earlier case with two tools, as  $\eta_{\text{parallel}}$  is no longer approximately equal to  $\Sigma \eta_{\text{series}}$  at small separations.

In closing, this work has shown that the use of tool templates can lead to a degradation in the communication of features to the substrate surface relative to that of a simple tool, depending on the proximity of those features to one another and the pulse duration used during the etch process. This phenomenon can be explained by the exponential nature of the dissolution current with respect to the overpotential. While the overpotential generated by the tool template is often roughly equivalent to that of the sum of its parts considered individually, the corresponding dissolution currents can vary widely,

as the comparison is between a summing of exponents (thus, multiplicative) and the sum after individual exponentiation (additive). Therefore, care must be taken when designing tool templates to account for the pulse duration to be used, insuring that features in close proximity to each other do not merge.

## 4.5 Summary

The ECM-USVP process has proven to be accurately modeled by use of an equivalent circuit model. Trends from the experimental transient current response have been captured during simulation of individual pulse and periods, while the linear increase in etch resolution with pulse duration has been matched for large diameter tools. In addition, the predictive capabilities of the model have been shown in quantifying the influence of the tool diameter on etch resolution for regions exhibiting two-dimensional behavior, an effect seen but not quantified experimentally. The model has also been used to predict the degradation in performance if using complex tool shapes or arrays, an important consideration as single-step processing is increasingly being employed.

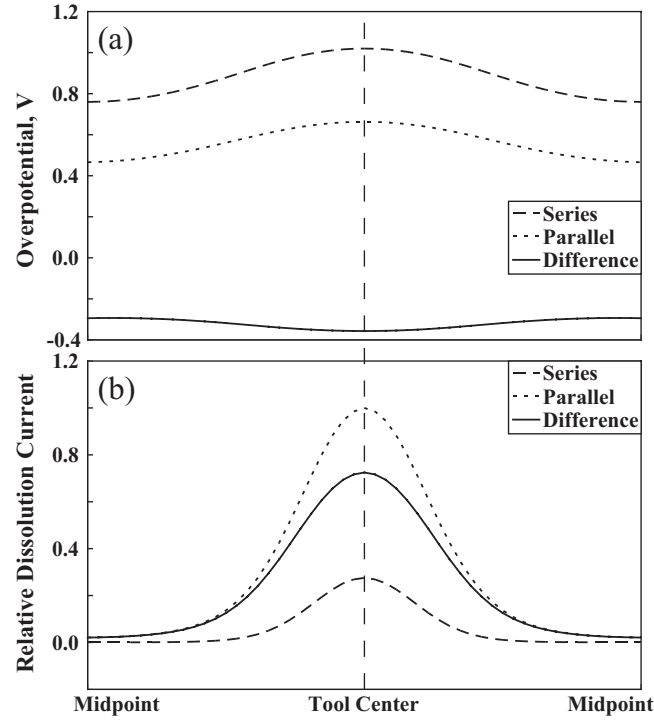


Figure 4.17: Cross sections showing the (a) overpotential and (b) relative dissolution current at the end of a 50 ns pulse at the substrate surface for the unit cell of an array of tools separated by  $8\text{ }\mu\text{m}$  in both  $x$  and  $y$  dimensions. Tools were held  $3\text{ }\mu\text{m}$  above an unmodified substrate. The series quantities are the sum of the individual tool contributions to the central unit cell of a  $5\times 5$  cell region. The difference is defined as parallel - series.

## Chapter 5

### Vacuum-Solid Interface: Differential Surface Charging of Dielectric

Differential surface charging of insulating or partially conducting materials is commonly caused by unbalanced fluxes between oppositely charged impinging species and/or inhomogeneities in surface electrical properties. Precise determination of the rate and asymmetry of surface charging has been an issue of great importance in a range of scientific and technological areas, such as X-ray photoelectron spectroscopic measurements [30], dusty plasma studies [15, 58], spacecraft design and operation [22], and microelectronic device fabrication [24, 25, 68]. In particular, differential charging is often a serious drawback in applying plasma processing technology to define high aspect ratio structures in the manufacturing of modern microelectronic and photonic devices and micro- and nanoelectrochemical systems. Moreover charging-induced discharges can significantly affect product yields.

#### 5.1 Plasma Background

A plasma consists of a collection of charged particles, formed when atoms or molecules within a gas are heated to or beyond the ionization energy. Such high temperatures liberate electrons and leave positively-charged ions behind. This results in a cloud of charged species which, while free, still interact with each other through electromagnetic fields.

Several varieties of plasmas exist, characterized by their densities, magnetic fields, ion and electron temperatures, and degrees of ionization. Belan [16] has classified them into three categories. Non-fusion terrestrial plasmas are weakly ionized, with ion temperatures that are colder than electron temperatures, often near room temperature, and densities ranging from  $10^{14}$  to  $10^{22} \text{ m}^{-3}$ . They are found in neon signs, fluorescent lamps, and processing plasmas. Fusion-grade terrestrial plasmas, on the other hand, are fully ionized, with temperatures ranging from 10-10,000 eV or above. Densities are on the range of  $10^{19}$  to  $10^{21} \text{ m}^{-3}$  for certain magnetic confinement devices, which much larger densities found in those used in inertial fusion studies. Finally, space plasmas is a general term for wide range of plasmas found away from Earth. These have densities ranging from  $10^6 \text{ m}^{-3}$  for interstellar space to  $10^{20} \text{ m}^{-3}$  in the solar atmosphere. They are usually fully ionized, with most having temperatures in the range of 1-100 eV.

Much effort has gone into the modeling of the plasmas used in plasma processing applications [47]. Of key importance is the behavior of ion and electron species interacting with surfaces surrounding the plasma. Due to higher electron mobility than that of the ions, these surfaces are typically negative with respect to the quasi-neutral regions of the plasmas with which they interact, a situation often exacerbated by the application of a potential. This gives rise to a non-neutral region with thickness of several Debye lengths through which the plasma potential is decreased to that of the wall, known as a sheath. Ions with sufficient velocities to enter the sheath are accelerated through it, whereas electron densities are decreased relative to that of the bulk plasma according to a Boltzmann factor.

It is not the goal of this work to model the behavior of the plasma and

sheath regions. Rather, plasma characteristics will be assumed from known experimental and simulation data as needed. In addition, only a small portion of the sheath region will be considered.

## **5.2 Plasma Etching and Deposition**

### **5.2.1 Overview**

Plasma processing is a widely-used technology, most often associated with the manufacture of integrated circuits. In a typical application, a plasma is created and subsequently used to modify a substrate surface through the initiation of chemical reactions or physical sputtering. For etching, advantages include the ability to etch surfaces in an anisotropic fashion and the ability to selectively etch different types of substrates according to the plasma chemistry and energy. In deposition applications, plasmas are capable of creating films unattainable by other means due to temperature requirements or the ability to create non-equilibrium compositions. Finally, ion implantation allows the doping of semiconductors and the hardening of metals.

A common feature of the integrated circuits created through plasma processing is a series of conducting and insulating layers. In a typical process, a conducting layer is deposited on top of an insulating material, followed by a patterning of the conductor surface and subsequent etching away of unwanted material. The etching of insulating materials has become more important, however, with the advent of damascene processes for the deposition of metal interconnects. In addition, heterogeneous structures such as those found in flash memory have become more important in recent years. Thus, regardless of the specific layer being modified during an integrated circuit processing step, there is a high probability of exposure of insulating materials to plasma.



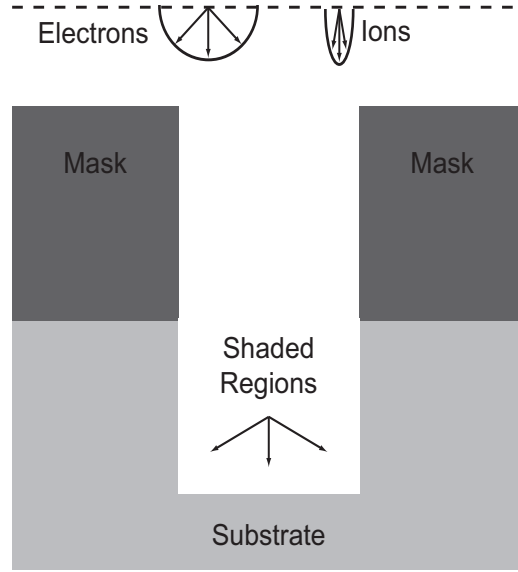


Figure 5.1: Schematic of the differential charging process for masked substrates under plasma exposure. High aspect ratio features receive reduced electron flux at the lower trench sidewalls and bottom due to shadowing effects. For the case of insulating materials in either of these regions, surface charging phenomena can result.

### 5.2.2 Differential Charging

It is well established that charges can accumulate on the exposed insulating surfaces of patterned structures during plasma etching and deposition, due to the directionality differences between impinging ions and electrons. This, in turn, gives rise to electric fields which can alter the trajectory, flux, and kinetic energy of incident ions, often resulting in undesirable side effects in the plasma-assisted processes. A schematic of the system geometry and ion and electron angular distributions is given in Figure 5.1.

Many theoretical studies [9, 21, 29, 38, 53] have been undertaken to elucidate this charging behavior and how ion and electron trajectories are mod-

ified by electric fields, in terms of plasma conditions, surface topologies, and surface electrical properties. In most of these earlier studies, charge accumulation and potential distribution were updated on set intervals using average fluxes of the impinging species. This approach may be suitable for finding the mean behavior of surface charge densities and potential distributions when the dimension of patterned structures is sufficiently large. However, as device feature sizes shrink into the nanometer-scale regime, the influence of an individual charge transferred to the surface will be larger, leading to an increase in the variability of potentials within the charging area. This leads to the question of whether a true steady-state-like behavior will be reached for high aspect ratio dielectric structures with small absolute dimension or will large oscillations in potential lead to essentially stochastic behavior.

# Chapter 6

## Computational Modeling: Plasma Charging of Nanopatterned Dielectric

Herein, details of the specific plasma systems of interest are given, including the geometry and dimensions of the dielectric structures used. This is followed by development of a computational model. Assumptions are presented and an overview of the model components is given, with relevant equations and numerical techniques discussed.

### 6.1 Background

Studies on the charging of insulating surfaces have typically involved high aspect ratio structures with both insulating sidewalls and bottoms. As a consequence, potentials rapidly build within these structures to match that of the impinging high energy ion species, significantly reducing ion flux to the bottom surface. In this study, an open bottom trench is considered instead. This structure may have bearing on the processing of structures with conducting materials at the bottom or heterogeneous dielectric-conductor structures.

The geometry of the two-dimensional open-bottom trench and simulation domain is given in Figure 6.1. The trench structure has an aspect ratio of 5, with the trench width varied from 500 nm to 100 nm to 50 nm. In each case, the width of the simulation domain is three times the trench width,

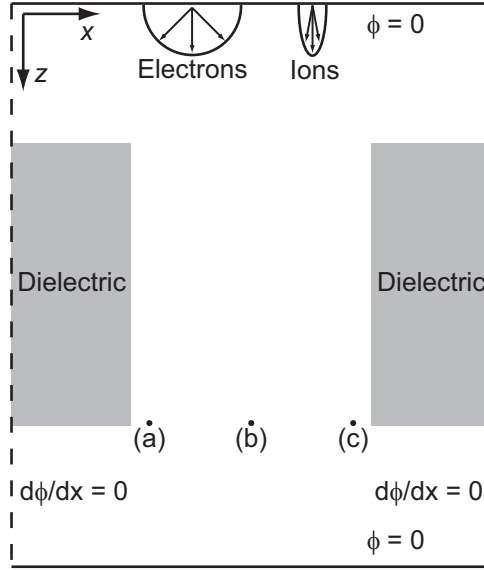


Figure 6.1: Schematic of the simulation domain used in this study (not to scale). Dielectric structures are represented by the gray rectangles. Upper and lower boundaries indicate the locations from which ions and electrons emerge and may exit, respectively. At these locations, the potential is fixed. Dashed side boundaries indicate reflective boundary conditions. Labeled points indicate locations where potential measurements are taken: (a) trench exit left, (b) trench exit center, and (c) trench exit right.

and the upper/lower boundary plane is located four times the trench width above/below the trench structure.

For these studies, simulation of the plasma is not considered. Rather, characteristics of high density plasmas from prior experimental and simulation studies are adopted. For the ion energy distribution function, a bimodal distribution is considered, matching recent results for the simulation of a collisionless rf sheath in a high density plasma [49]. The ion temperature from this study was 300 K, but this value is varied from 1 K to 10,000 K to examine the impact of the ion angular distribution. The electron temperature is 4 eV,

typical of high density plasmas. The flux of both ion and electron species is assumed equal to  $1.0 \cdot 10^{16} \text{ cm}^{-2} \text{ s}^{-1}$ , a value typical of etching applications [71].

## 6.2 Computational Model

### 6.2.1 Assumptions

The primary assumptions made are as follows:

1. Ion and electron densities are such that the Laplace equation can be used to determine the potential.

As described below, the cross-section of the largest simulation domain has an area of  $1.5 \text{ } \mu\text{m} \times 62.5 \text{ nm} = 9.375 \cdot 10^{-10} \text{ cm}^2$ . For the combined ion and electron fluxes, this gives, on average, one particle entering the simulation domain every  $5.3 \cdot 10^{-8} \text{ s}$ . With the  $z$  velocity of low energy ion species on the order of  $1 \cdot 10^4 \text{ m/s}$  and distance of at most  $6.5 \cdot 10^{-6} \text{ m}$  to cover in the  $z$  direction, this gives a residence time of at most  $6.5 \cdot 10^{-10} \text{ s}$  for any given particle. Thus, on average the domain is void of particles and the Laplace equation is appropriate.

2. Ion and electron impingement occurs randomly, not influenced by the rf-bias cycle.

In a similar derivation to the above, both ions and electrons enter the largest domain with a frequency of 3.1 MHz. The plasmas from which the plasma characteristics used in this study were obtained have frequencies of 13.56 MHz [49] and 27 MHz [71]. Thus, several rf-bias cycles should occur between the arrival of consecutive ion or electron species, making the matter of when during the rf-bias cycle an ion or electron is more likely to emerge unimportant.

3. The location of the upper boundary from which ions and electrons emerge can vary along with the variation in trench width.

As the upper surface of the dielectric structure receives equal ion and electron fluxes without shadowing, the surface charge densities there should be approximately neutral. Thus the electric fields experienced by ions and electrons as they emerge from the boundary and approach the dielectric structure should be small in magnitude and the cumulative potential imparted to the particles in that region minimal.

4. Impinging ions and electrons transfer their charge to the surface with 100% probability.

This assumption follows those from other studies [29, 53]. Transfer of charge from ions to the surface is most likely via Auger neutralization prior to impact, but the exact mechanism is considered unimportant.

### 6.2.2 Overview

The simulation strategy, as depicted in the flowchart in Figure 6.2, is as follows: (1) generate an ion or electron by sampling from a given energy distribution function and randomly determining a position at the upper boundary plane; (2) track the motion of the generated species in the electric field arising from the differential charging of the trench; (3) transfer the charge of the species to the dielectric structure in the event of a collision; and (4) update the potential and electric field after each collision. Ions which travel through the structure without colliding are tracked until they reach the lower boundary plane, and their energies are recorded. At set intervals, conduction of charge along the surface is calculated and the potential and electric field updated.

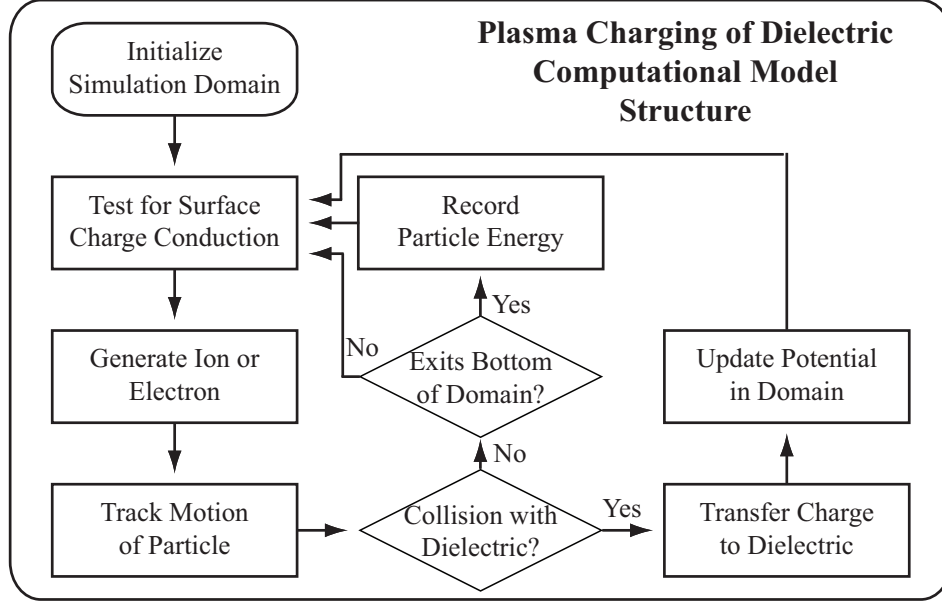


Figure 6.2: Flowchart depicting the major components and linkages for the Plasma Charging of Dielectric Computational Model.

### 6.2.3 Ion and Electron Generation

As mentioned above, a flux of  $1.0 \cdot 10^{16} \text{ cm}^{-2} \text{ s}^{-1}$  is assumed for both ions and electrons, giving an equal probability for either when randomly choosing the next particle type. For the electrons, the average temperature of  $kT_e = 4 \text{ eV}$  is used for the Boltzmann distribution, from which  $x$  and  $z$  velocities are obtained. Similarly, ions (assumed to be  $\text{Ar}^+$ ) are assumed to have average temperatures ranging from 1 to 300 to 10,000 K in order to generate thermal  $x$  and  $z$  velocities. To the thermal  $z$  component, a directed  $z$  velocity is added, sampled from a bimodal energy distribution, given in Figure 6.3. Thus, each ion temperature used generates a bimodal ion energy distribution with angular distributions which are correlated to ion energy. All particles emerge from

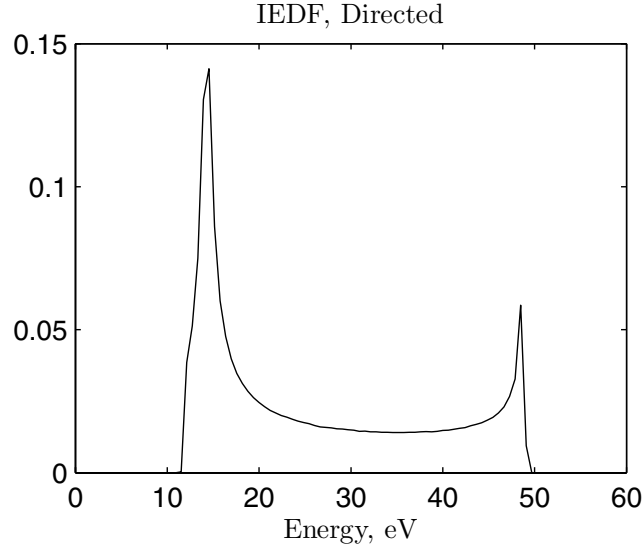


Figure 6.3: Ion energy distribution function (IEDF) for the directed  $z$  velocity. Adapted from [49].

the upper boundary, with their initial  $x$  positions along the boundary also determined randomly.

For all of the above, pseudorandom numbers are generated using a Mersenne Twister algorithm, MT19937 [54]. The pseudorandom numbers generated have a period of  $2^{19937} - 1$  and are 623-dimensional equidistributed. The former property essentially means there is no danger of exhausting the sequence of numbers generated. The latter property indicates there is negligible correlation between successive values.

#### 6.2.4 Potential Calculation

The potential distribution in the vacuum region is calculated with the Laplace equation ( $\nabla^2 \phi = 0$ ). Gauss's Law ( $\mathbf{n} \cdot \nabla \phi = -\frac{\sigma}{\epsilon_0}$ ) is used at locations



adjacent to the dielectric surface, where  $\mathbf{n}$  is the outward normal,  $\sigma$  is the surface charge density, and  $\epsilon_0$  is the permittivity of free space. The upper and lower boundaries in the simulation domain have the potential set to zero. Reflective boundary conditions are used at domain side boundaries. The simulation domain is divided into small square meshes: in  $x$  and  $z$  dimensions, the mesh length is one-eighth of the trench width, and a  $y$  dimension is assumed equal to one  $x/z$  mesh length where necessary.

The conjugate gradient method is employed to update the potential upon each collision of a particle with the dielectric surface or during calculation of surface conduction. Unlike the earlier ECM-USVP model, direct solution techniques such as LU-Decomposition are applicable, as the coefficients which form the matrix do not change once initialized. The conjugate gradient method still has two advantages over direct solution methods, however. As earlier, it reduces storage complexity over that of direct methods (although for the mesh sizes used here, memory requirements are much lower than that of the ECM-USVP model). More importantly, the previous conjugate gradient solution can be used as the initial guess for the subsequent system of equations following a change in the surface charge density, allowing for rapid convergence. Still, updating the potentials is by far the most computationally expensive step in the model, with profiling of the code revealing roughly two orders of magnitude difference between this step and those of generating a particle and tracking its path.

Obtaining the proper positive-definite, symmetric form of the equations for the conjugate gradient method is not difficult. The Laplace equation is

already in an appropriate symmetrical form:

$$\begin{aligned}\nabla^2\phi &= \frac{\partial^2\phi}{\partial x^2} + \frac{\partial^2\phi}{\partial z^2} \\ &\simeq \frac{\phi_{i+1,k} - 2\phi_{i,k} + \phi_{i-1,k}}{h_x^2} + \frac{\phi_{i,k+1} - 2\phi_{i,k} + \phi_{i,k-1}}{h_z^2},\end{aligned}\tag{6.1}$$

where  $\phi_{i,k}$  is a node in the vacuum away from any boundaries or surfaces, the remaining  $\phi_{x,z}$  are its neighbors in the  $x$  and  $z$  directions, and  $h_x$  and  $h_z$  are the mesh lengths in the  $x$  and  $z$  dimensions. This expression is negated to insure a positive-definite form, giving

$$\frac{-\phi_{i+1,k} + 2\phi_{i,k} - \phi_{i-1,k}}{h_x^2} + \frac{-\phi_{i,k+1} + 2\phi_{i,k} - \phi_{i,k-1}}{h_z^2} = 0\tag{6.2}$$

For reflective boundaries, this expression is simplified. For example, a reflective boundary encountered in the  $-x$  direction would have  $\phi_{i,k} = \phi_{i-1,k}$ , resulting in

$$\frac{-\phi_{i+1,k} + \phi_{i,k}}{h_x^2} + \frac{-\phi_{i,k+1} + 2\phi_{i,k} - \phi_{i,k-1}}{h_z^2} = 0\tag{6.3}$$

Similarly, the fixed potentials at the upper and lower boundaries are simply replaced with the appropriate potential (0 V). Thus, for a fixed potential encountered in the  $+z$  direction:

$$\frac{-\phi_{i+1,k} + 2\phi_{i,k} - \phi_{i-1,k}}{h_x^2} + \frac{2\phi_{i,k} - \phi_{i,k-1}}{h_z^2} = 0\tag{6.4}$$

Nodes adjacent to the dielectric surfaces must maintain the form given by Equation 6.2. Thus, nodes at the surface must obey Gauss's Law and also give a symmetric form. For a surface node connected to a node in the vacuum

in the  $+x$  direction, this is accomplished as follows:

$$\begin{aligned}
\mathbf{n} \cdot \nabla \phi &= -\frac{\sigma}{\epsilon_0} \\
\frac{\partial \phi}{\partial x} &= -\frac{\sigma}{\epsilon_0} \\
&\simeq \frac{\phi_{i+1,k} - \phi_{i,k}}{h_x} = -\frac{\sigma}{\epsilon_0} \\
\frac{-\phi_{i+1,k} + \phi_{i,k}}{h_x} &= \frac{\sigma}{\epsilon_0} \\
\frac{-\phi_{i+1,k} + \phi_{i,k}}{h_x^2} &= \frac{\sigma}{\epsilon_0 h_x}
\end{aligned} \tag{6.5}$$

This situation is somewhat complicated at nodes at the corners of the dielectric, which have two neighbors in vacuum. In this case, an averaging scheme is used. Assuming  $+x$  and  $+z$  neighbors for the surface node,

$$\begin{aligned}
\frac{-\phi_{i+1,k} + \phi_{i,k}}{h_x^2} &= \frac{\sigma}{\epsilon_0 h_x} \\
&= \frac{Q}{\epsilon_0 h_x h_y h_z} \\
\frac{-\phi_{i,k+1} + \phi_{i,k}}{h_z^2} &= \frac{\sigma}{\epsilon_0 h_z} \\
&= \frac{Q}{\epsilon_0 h_x h_y h_z} \\
\frac{-\phi_{i+1,k} + \phi_{i,k}}{h_x^2} + \frac{-\phi_{i,k+1} + \phi_{i,k}}{h_z^2} &= \frac{2Q}{\epsilon_0 h_x h_y h_z},
\end{aligned} \tag{6.6}$$

where  $Q$  is the total charge at the surface node.

### 6.2.5 Particle Trajectory Calculation

Tracking the motion of the charged particles in the electric field is accomplished through use of the equation of motion for each particle:  $m \frac{d\mathbf{v}}{dt} = q\mathbf{E}$ . The 4th-order Runge-Kutta method is employed, with a time step chosen

to insure the particle does not travel more than one-fourth of a mesh length in any dimension. Details of the handling of the local electric fields and the equations used in the Runge-Kutta method are given in Appendix E.

### 6.2.6 Surface Conduction

A sheet resistance of  $1 \cdot 10^{20} \Omega$  is assumed, which falls at the high end of experimentally reported values for  $\text{SiO}_2$  [26]. Calculation of surface conduction is accomplished by an explicit scheme: (1) the potentials of nodes on the dielectric surface are compared to their neighbors; (2) currents into and out of the nodes are determined based on these potential differences and surface resistances between nodes; (3) charge transfers are calculated for a specified time step; and (4) all potentials within the domain are recalculated. We choose a time step for surface conduction such that approximately one-tenth of the charge differential is transferred between nodes before updating all potentials within the domain. This time step is dependent on the mesh sizes used and is given by

$$\Delta t_{\text{Conduction}} = 0.1 R_S \epsilon_0 \min \left( \frac{h_x^2}{h_z}, \frac{h_z^2}{h_x} \right) \quad (6.7)$$

where  $R_S$  is the sheet resistance. For the sheet resistance and mesh sizes used here, this value ranges from  $\sim 0.5$  to  $\sim 5$  seconds, which is  $10^5$  to  $10^8$  times as large as the respective time per particle. The time step was derived according to the following assumptions: (1) neighboring nodes in the vacuum have approximately the same potential (e.g.,  $\phi_{i,k} \simeq \phi_{i+1,k}$ ); (2) surface nodes and their neighbors in vacuum have potentials governed by the Gauss's Law relationship (e.g.,  $\phi_{i,k+1} = \phi_{i,k} + \frac{\sigma}{\epsilon_0} h_z = \phi_{i,k} + \frac{Q}{\epsilon_0 h_x h_y} h_z$ ); (3) surface currents are governed by the difference in potential between neighboring surface nodes and the surface resistance between them (e.g.,  $R_S \frac{h_x}{h_y}$ ); and (4) at most one-tenth of

the charge difference between neighboring surface nodes should be transferred in any step. Thus, the charge transferred between neighboring surface nodes is given by

$$\begin{aligned}
Q_{Transferred} &= \frac{\phi_{i,k+1} - \phi_{i+1,k+1}}{R_S \frac{h_x}{h_y}} \Delta t_{Conduction} \\
&= \frac{(\phi_{i,k} + \frac{Q_{i,k+1}}{\epsilon_0 h_x h_y} h_z) - (\phi_{i+1,k} + \frac{Q_{i+1,k+1}}{\epsilon_0 h_x h_y} h_z)}{R_S \frac{h_x}{h_y}} \Delta t_{Conduction} \\
&= \frac{\frac{\Delta Q}{\epsilon_0 h_x h_y} h_z}{R_S \frac{h_x}{h_y}} \Delta t_{Conduction} \\
&= \frac{\Delta Q h_z}{R_S \epsilon_0 h_x^2} \Delta t_{Conduction}
\end{aligned} \tag{6.8}$$

Substituting  $Q_{Transferred} = 0.1 \Delta Q$  and rearranging gives

$$\Delta t_{Conduction} = 0.1 R_S \epsilon_0 \frac{h_x^2}{h_z} \tag{6.9}$$

The above can be repeated for surface-vacuum neighbors in the  $x$  direction, giving the other form found in Equation 6.7. If not using a square mesh, the smaller value is taken.

## Chapter 7

### Simulation Results: Plasma Charging of Nanopatterned Dielectric

Unlike the earlier electrochemical machining studies, the open geometry of the high aspect ratio dielectric structure used here does not lend itself to direct comparison with experiment or previous simulation studies. In addition, the properties investigated are difficult if not impossible to measure experimentally. These include measurements of the potential within the trench, ion and electron trajectories, and the transient flux and energies of ions exiting the trench. Due to the above, the observations made are presented in a relative sense, beginning with the largest structures which exhibit the least variation in behavior. Results from these structures closely match the behavior of closed-bottom structures previously investigated [53].

Some of the work which follows has recently been accepted for publication [34].

#### 7.1 Transient Potential

A large number of charged particles were generated and allowed to impinge on the dielectric structures, using all three ion temperatures as well as all three trench sizes. The transient potential was tracked at the three locations indicated in Figure 6.1 as a function of the total number of particles

generated, with the potential sampled after every 5,000 particles. The results are given in Figures 7.1, 7.2, and 7.3 for ion temperatures of 1 K, 300 K, and 10,000 K, respectively.

Within each of these figures, certain trends hold across all three ion temperatures. In general, it takes longer for the potential to approach a pseudo-steady-state value for the largest trench width of 500 nm. This is expected due to the relatively large surface area which must be saturated. Upon reaching the mean value, very little deviation in the potential is seen here. This is also expected, as individual ions and electrons have less impact on the surface charge density for the large trench. This can be contrasted by both the 100 and 50 nm results. For the 100 nm wide trench, the charging process to reach the pseudo-steady-state occurs much more rapidly, with the exception of the  $T_i = 300$  K data, where it appears a false steady-state value was approached before rapidly correcting itself. For all temperatures, the pseudo-steady-state achieved with the 100 nm trench has a similar mean potential to the 500 nm trench. The behavior is quite different as the trench width is reduced further to 50 nm. Here there is no distinct charging phase, and the mean potential is  $\sim 0$  V.

Among the different ion temperatures, variation is seen in the time required to reach the pseudo-steady-state for the larger trench widths. For the 1 K case, the almost purely  $z$  directed ions require over  $5 \cdot 10^6$  particles before the pseudo-steady-state is achieved with the 500 nm trench. Similarly, roughly  $2 \cdot 10^6$  particles are required for the 100 nm wide structure. This is expected as a large number of ions will simply pass straight through the trench until the upper trench sidewalls become saturated by enough electrons to influence the ion trajectories. As the ion temperature is increased, the amount of time

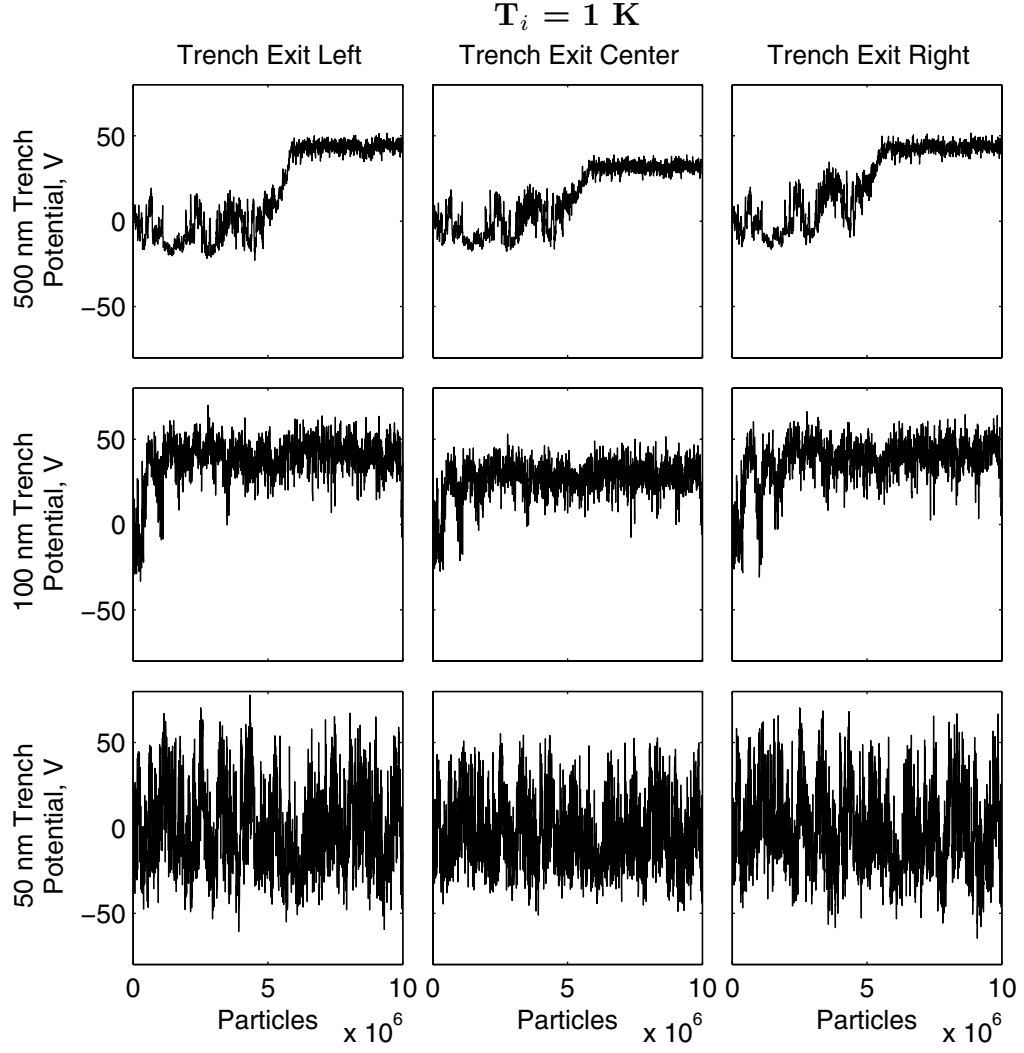


Figure 7.1: Potential with number of particles generated for the indicated trench widths and locations.  $T_i = 1 \text{ K}$ . The time-scale of each plot varies with trench width: 500 nm: 0.533 s, 100 nm: 13.3 s, 50 nm: 53.3 s.



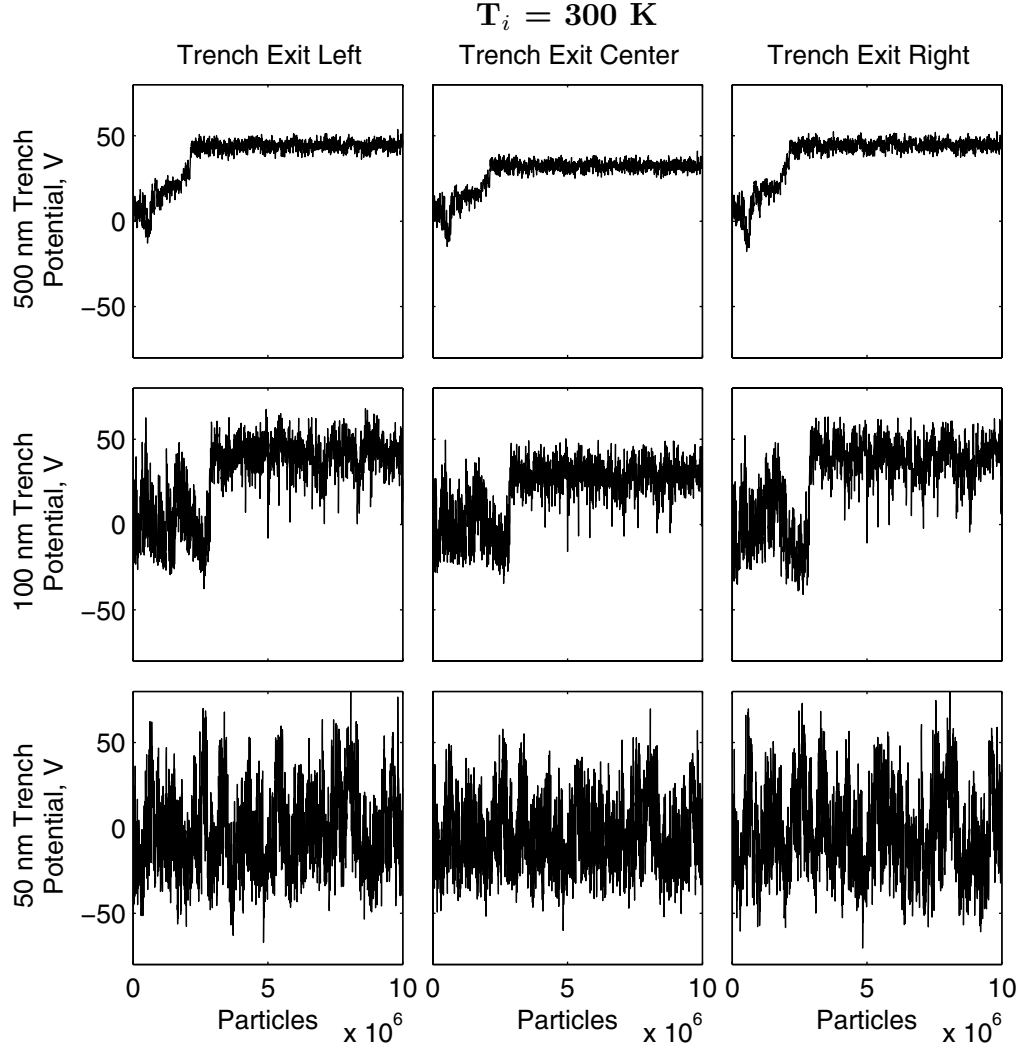


Figure 7.2: Potential with number of particles generated for the indicated trench widths and locations.  $T_i = 300 \text{ K}$ . The time-scale of each plot varies with trench width: 500 nm: 0.533 s, 100 nm: 13.3 s, 50 nm: 53.3 s.

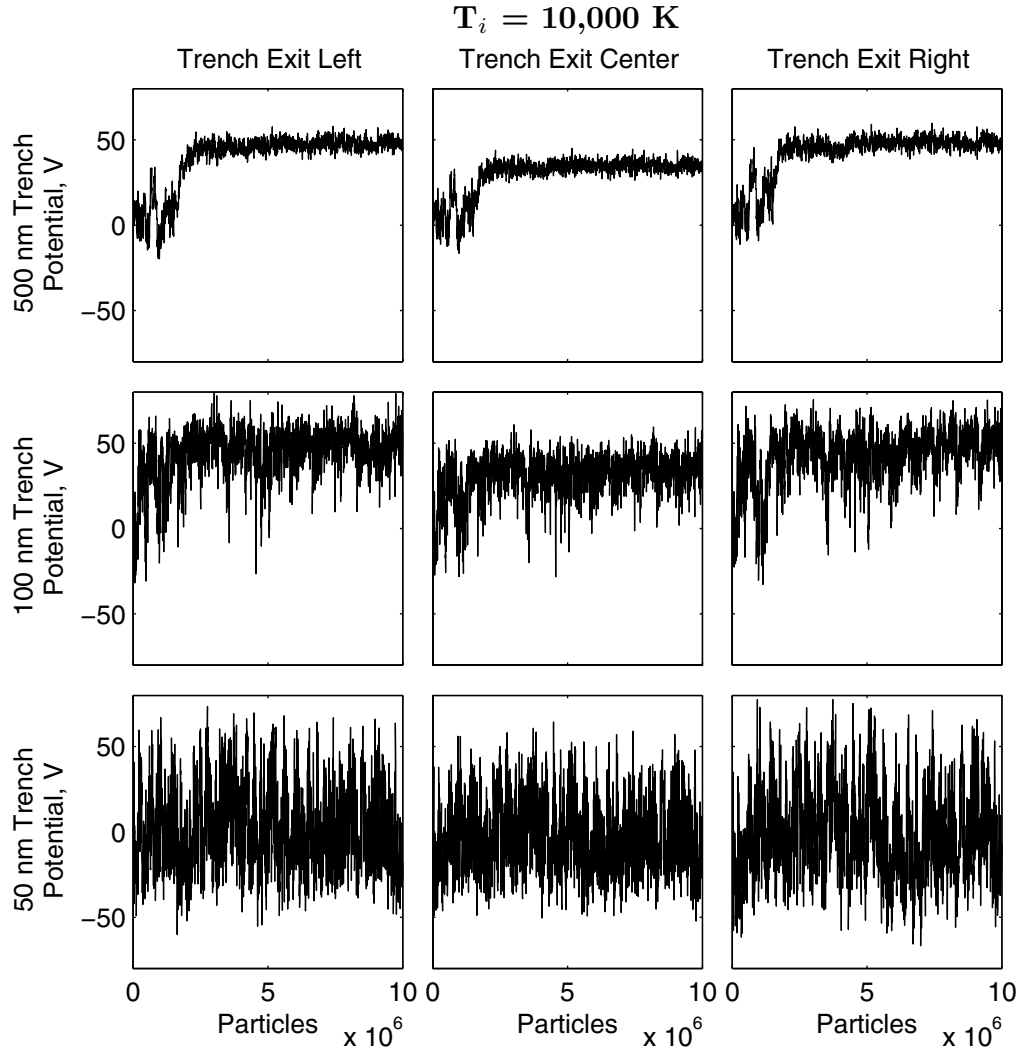


Figure 7.3: Potential with number of particles generated for the indicated trench widths and locations.  $T_i = 10,000 \text{ K}$ . The time-scale of each plot varies with trench width: 500 nm: 0.533 s, 100 nm: 13.3 s, 50 nm: 53.3 s.

Table 7.1: Transient Potential Statistics

Width	Loc.	Mean			Median			Range			Std. Dev.		
		T <sub>1</sub>	T <sub>2</sub>	T <sub>3</sub>	T <sub>1</sub>	T <sub>2</sub>	T <sub>3</sub>	T <sub>1</sub>	T <sub>2</sub>	T <sub>3</sub>	T <sub>1</sub>	T <sub>2</sub>	T <sub>3</sub>
500 nm	All	18.9	19.4	23.1	18.7	19.3	22.9	19.0	18.2	22.6	2.7	2.5	3.2
	(a)	43.6	44.2	47.8	43.8	44.0	47.8	16.8	17.4	17.3	2.9	2.6	3.0
	(b)	31.8	32.2	34.8	32.0	32.1	34.8	14.7	16.1	17.1	2.6	2.3	2.7
	(c)	43.6	44.2	47.8	43.8	44.0	47.8	16.8	17.4	17.3	2.9	2.6	3.0
100 nm	All	20.8	20.6	25.1	20.9	20.7	25.4	55.4	51.2	54.6	8.0	7.9	8.3
	(a)	40.2	41.0	48.4	40.8	41.7	49.1	70.9	67.3	69.0	9.7	10.3	10.0
	(b)	29.1	28.5	34.4	29.5	28.7	34.9	57.2	53.8	58.7	8.1	8.5	8.9
	(c)	40.2	41.0	48.4	40.8	41.7	49.1	70.9	67.3	69.0	9.7	10.3	10.0
50 nm	All	7.2	7.2	7.9	7.2	6.4	6.5	80.4	79.4	84.8	16.0	16.6	14.2
	(a)	0.7	1.7	-1.1	-4.5	-2.0	-6.1	126.9	137.6	114.4	26.5	26.8	23.8
	(b)	-3.0	-1.8	-4.8	-6.6	-5.4	-8.7	101.7	121.8	109.3	22.5	23.2	20.5
	(c)	0.7	1.7	-1.1	-4.5	-2.0	-6.1	126.9	137.6	114.4	26.5	26.8	23.8

Note: T<sub>1</sub>, T<sub>2</sub>, and T<sub>3</sub> refer to 1 K, 300 K, and 10,000 K, respectively. “All” indicates the average potential of the entire trench region. (a), (b), and (c) are the bottom left, center, and right locations, as indicated in Figure 6.1. All values in V.

to reach steady-state-like behavior is in general reduced. The broader angular distribution of ions allows for the transfer of charge from ions to the trench sidewalls without requiring the influence of electric fields.

## 7.2 Potential Statistics

Statistics were compiled from the above simulations at the three locations at the bottom of the trench as well as for the mean potential within the entire trench region. To insure the statistics are describing pseudo-steady-state behavior, samples were taken from the period between when the  $7.5 \cdot 10^6$  and  $1 \cdot 10^7$  particles impinged the surface, which appears well beyond the initial charging stage for all cases. This gives roughly 500 samples for each case. Table 7.1 contains the data.

As was apparent from the earlier potential transient figures, there is little variation in the behavior of the 500 nm trench for all ion temperatures. The standard deviations are  $\sim 3$  V in all cases and mean potentials for the

entire trench as well as specific locations at the trench exit are similar when results among the different ion temperatures are compared. There is a mild trend toward increased potentials with increasing ion temperature, which is not unexpected given the increased ability of ions to impact the trench sidewalls. When the trench width is reduced to 100 nm, this trend strengthens for the 10,000 K case. More striking, however, is increase in the standard deviation for all measurements. Values here are in the range of 8 to 10 V. The mean values do not significantly differ from the corresponding 500 nm values, however.

As the trench width is reduced to 50 nm, the above trends are overtaken by a severe increase in the standard deviation to values above 20 V at the trench exit. Mean potentials at these locations now approach 0 V. There is also a significant decrease in the average potential within the trench region to values below 10 V, whereas values at or above 20 V were common for the larger trenches.

### 7.3 Potential Contours

Snapshots were taken of the potentials within the trench region, and the resulting contour plots are given in Figures 7.4, 7.5, and 7.6 for ion temperatures of 1 K, 300 K, and 10,000 K, respectively. Snapshots were chosen based on the statistical analysis provided in Table 7.1. Data from the “All” cases (the average potential of all points within the trench at each time step) were used to determine mean ( $\bar{X}$ ) and extreme ( $\bar{X} \pm 2\sigma$ ) average potentials for each trench size/ion temperature combination. The 500 average potential values for each combination were then compared with  $\bar{X}$  and  $\bar{X} \pm 2\sigma$ , with those average potential values closest to the targeted values chosen as representative.

For the 500 nm wide trenches, a comparison among the potential con-

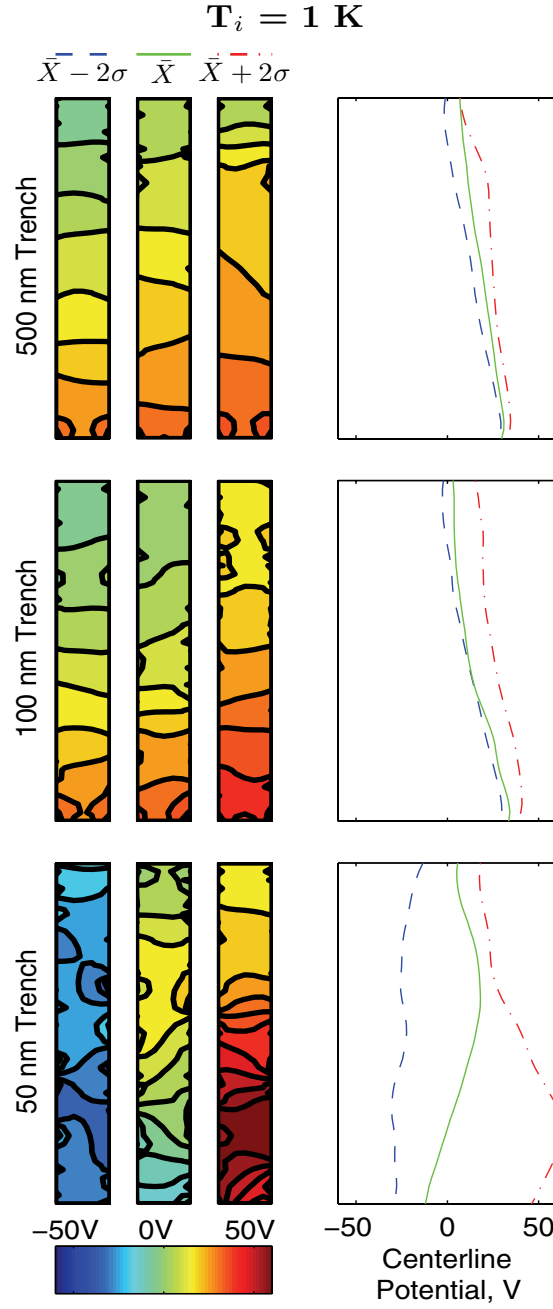


Figure 7.4: Potential contours indicating mean ( $\bar{X}$ ) and extreme ( $\bar{X} \pm 2\sigma$ ) behavior, with centerline potentials in the trench region.  $T_i = 1 \text{ K}$ .

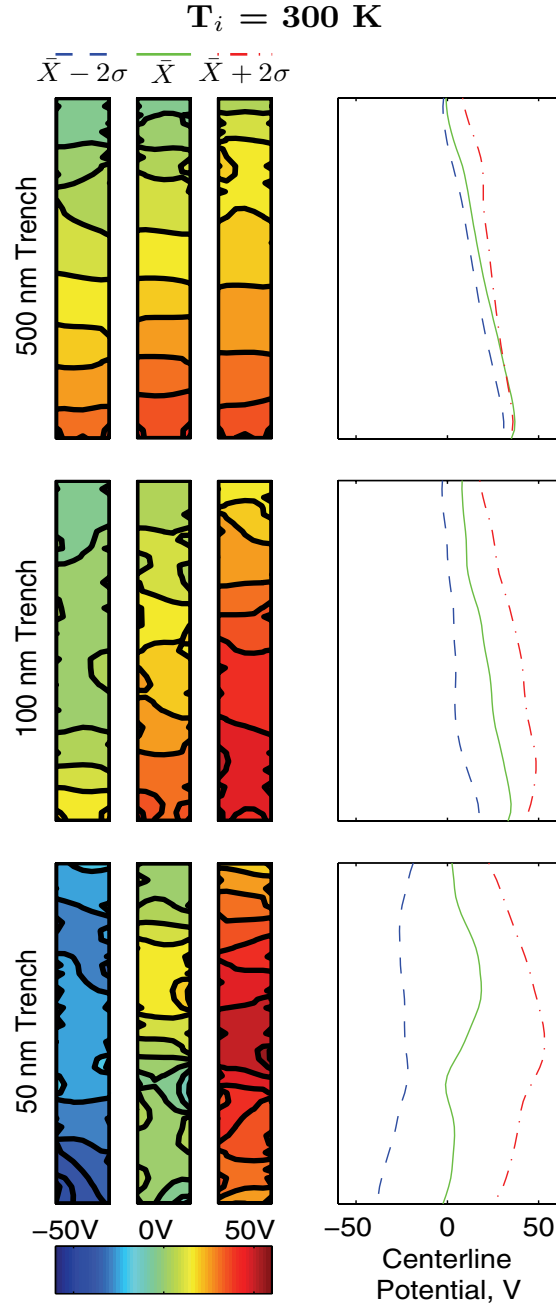


Figure 7.5: Potential contours indicating mean ( $\bar{X}$ ) and extreme ( $\bar{X} \pm 2\sigma$ ) behavior, with centerline potentials in the trench region.  $T_i = 300 \text{ K}$ .

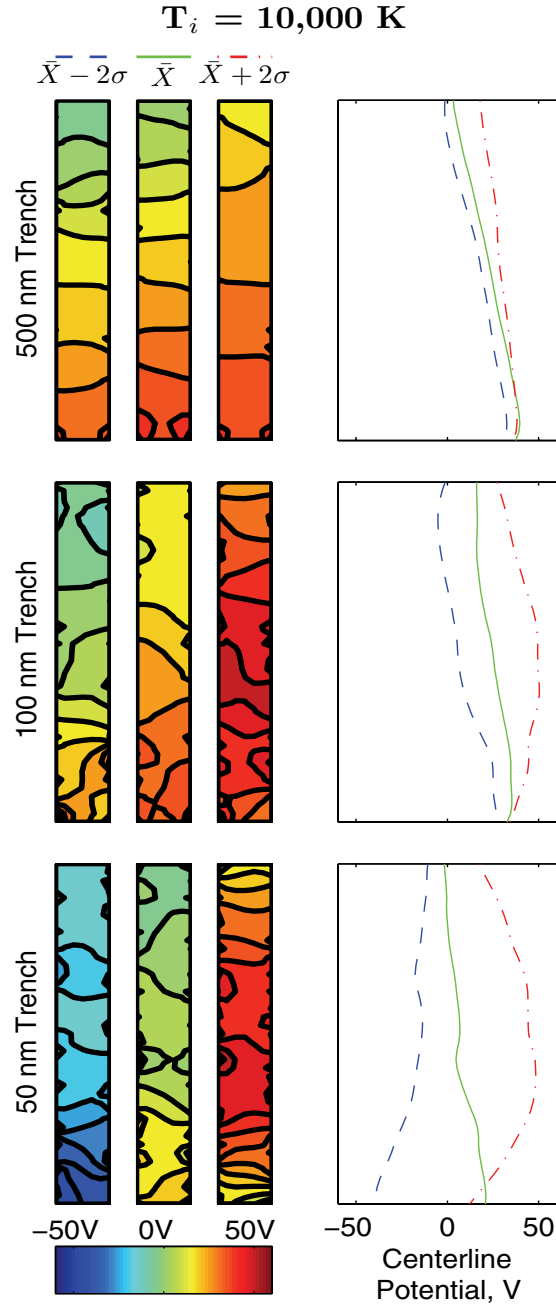


Figure 7.6: Potential contours indicating mean ( $\bar{X}$ ) and extreme ( $\bar{X} \pm 2\sigma$ ) behavior, with centerline potentials in the trench region.  $T_i = 10,000 \text{ K}$ .

tours reveals a lack of variability in the potentials, again showing steady-state behavior. For all ion temperatures and each potential behavior, potentials of 35 V are obtained near the trench exit center, a significant barrier to low energy ions. In addition, the isolines are largely parallel to the  $x$  axis and somewhat equally spaced, indicating small  $x$  components and near-constant  $z$  components of the electric fields within the trench region.

The charging behavior changes dramatically as the trench dimension is decreased, although there is still very little influence of the ion temperature on the results obtained. By 100 nm, isolines are seen with varying spacing and regions where they are no longer parallel to the  $x$  axis; the electric field components are no longer constant ( $E_z$ ) nor insignificant ( $E_x$ ). For extreme cases, the potential barrier at the exit has been reduced to  $\sim 20$  V or lower. A further decrease in size to 50 nm results in similar but more extreme behavior. Potentials range from -50 to 50 V, and the electric field strengths are larger, with  $E_z$  ranging from positive to negative along the centerline for the mean case. It can also be surmised that the potential barrier within the trench is no longer a significant obstruction to low energy ions approximately half of the time.

## 7.4 Ion Trajectories

The impact of the resulting electric fields on ion trajectories was investigated, as illustrated in Figure 7.7. Here, the  $\bar{X} - 2\sigma$  data for an ion temperature of 1 K were used for the electric fields. That is, an electric field at each trench width that should be favorable for the ions to enter the trench, relative to the average field at that trench width. To clearly demonstrate the differences between the three trench widths, unimodal ion energy distributions



are used for high energy (45 eV) and low energy (15 eV) ions. In addition, the initial  $x$  velocity components are set to 0 in all cases. For this analysis, the potentials are fixed at their values from the  $\bar{X} - 2\sigma$  data and not updated upon ion impacts with the dielectric surface.

For the 45 eV ions, both the 500 nm and 100 nm wide trenches have a significant impact on the trajectories of ions which exit the trench. The electric fields at the trench bottoms are strong enough to alter the  $x$  velocities of the ions, resulting in a focusing of the ions to the trench exit midpoint. This is contrasted by the trajectories from the 50 nm wide trench. Here, ion trajectories are mildly focused at a region near the exit of the domain. In addition, no ions are directed into the trench sidewall.

At 15 eV, ions for both the 500 nm and 100 nm wide trenches fail to exit the trench. Trajectories are significantly altered to force collisions with the sidewalls for ions which enter the trench region or, as seen with some ions in the 500 nm trench, are forced out of the trench, exiting at the top of the simulation domain. At 50 nm, however, almost all ions entering the trench region reach the exit. These ions undergo focusing to one side at the trench exit, indicating an imbalance in the potentials at the trench sidewalls there.

## 7.5 Exiting Ion Flux and Energy

As illustrated in Figures 7.8, 7.9, and 7.10, the flux and kinetic energy distribution of ions passing through the trench was examined to determine the influence of the difference in charging behaviors. Again, all three ion temperatures were considered, but little difference was seen among them once the systems had completed the initial charging stage and reached steady-state. Thus, the main influences of ion temperature here are its impact on the ion

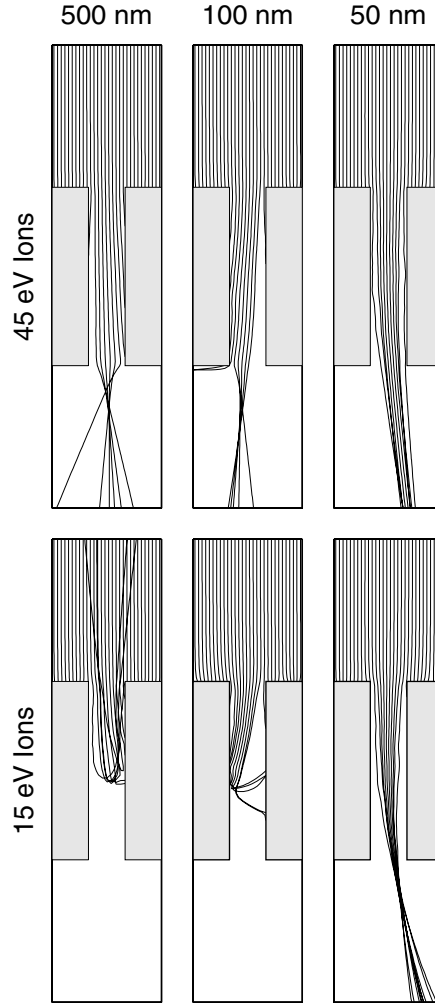


Figure 7.7: Trajectories of high and low energy ion species passing through trenches with the indicated widths. The electric fields used match the  $\bar{X} - 2\sigma$  contours for an ion temperature of 1 K (Figure 7.4) with the appropriate trench width. In all cases, the initial  $x$  velocity component is 0.

energy distribution function for ions entering the simulation domain and its hastening of steady-state behavior as the temperature is increased.

For the 500 nm wide trench, ions of all energies are able to pass through the trench during the initial surface charging stage, regardless of ion temperature. Once the pseudo-steady-state is reached, however, low energy ions entering the trench are either directed to the trench sidewall or forced out the trench entrance, as the potential barrier at the trench exit remains above 20 V at all times. In addition, the results for the 1 K case provide more evidence to the lack of impact the electric fields in the trench have on ion trajectories during the initial charging stage. Both low and high energy ions pass directly through the trench region in large numbers.

This situation changes for a trench of width 100 nm. As with the larger trench described above, there is a period of charge buildup on the dielectric surface during which low energy ions may pass through the trench. Once the near steady-state is reached, however, low energy ions are able to exit the trench on a periodic basis, corresponding to spikes wherein the potential in the trench is reduced to near or below zero.

As the trench width is reduced to 50 nm, low energy ions pass through the trench with little interruption throughout the simulation. Again this can be explained through an investigation of the behavior of the potential. In this case, there is no discernible period of charge accumulation on the dielectric surface as seen with the larger trenches, so relatively constant behavior of ion energies exiting the trench is expected. In addition, large fluctuations in the potential at the trench exit occur with high frequency, leading to roughly equal periods of the trench being positively and negatively charged and allowing a steady stream of low energy ions to pass through the trench.

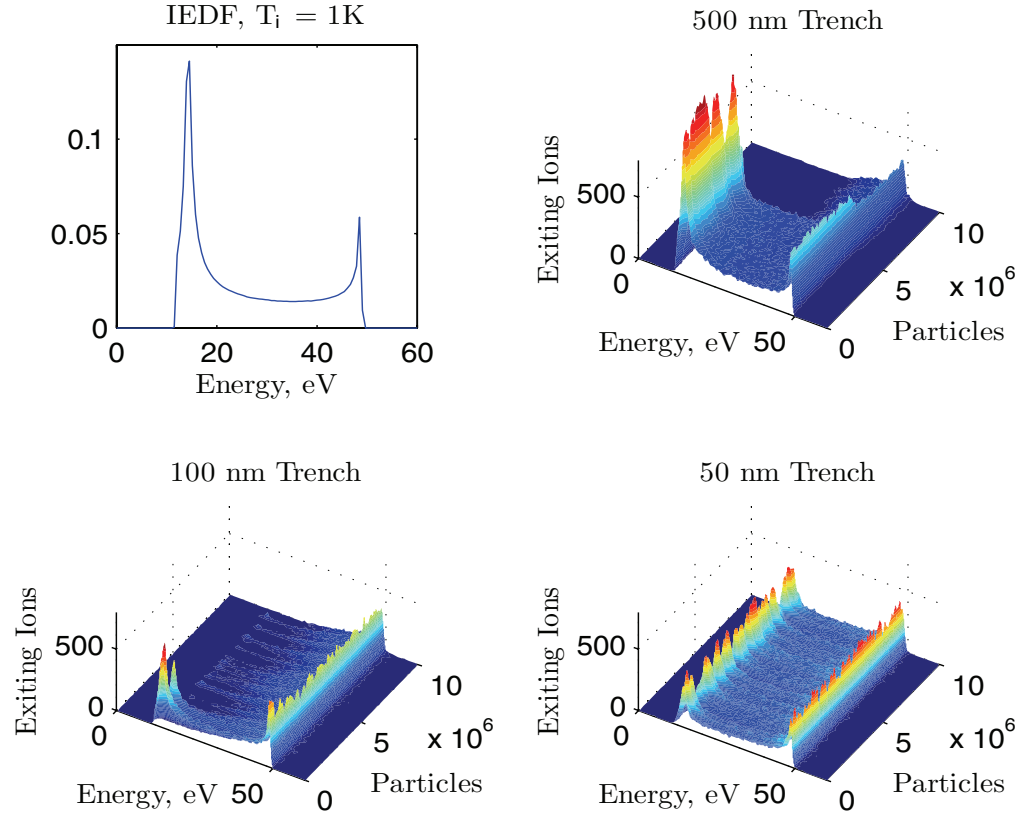


Figure 7.8: Extrusion plots showing numbers and energies of ions reaching the trench exit with the number of combined ions and electrons entering the simulation domain. Intervals of 20,000 combined ions and electrons entering the domain are used between recording of data. The ion energy distribution function of ions entering the simulation domain is also given.  $T_i = 1$  K.

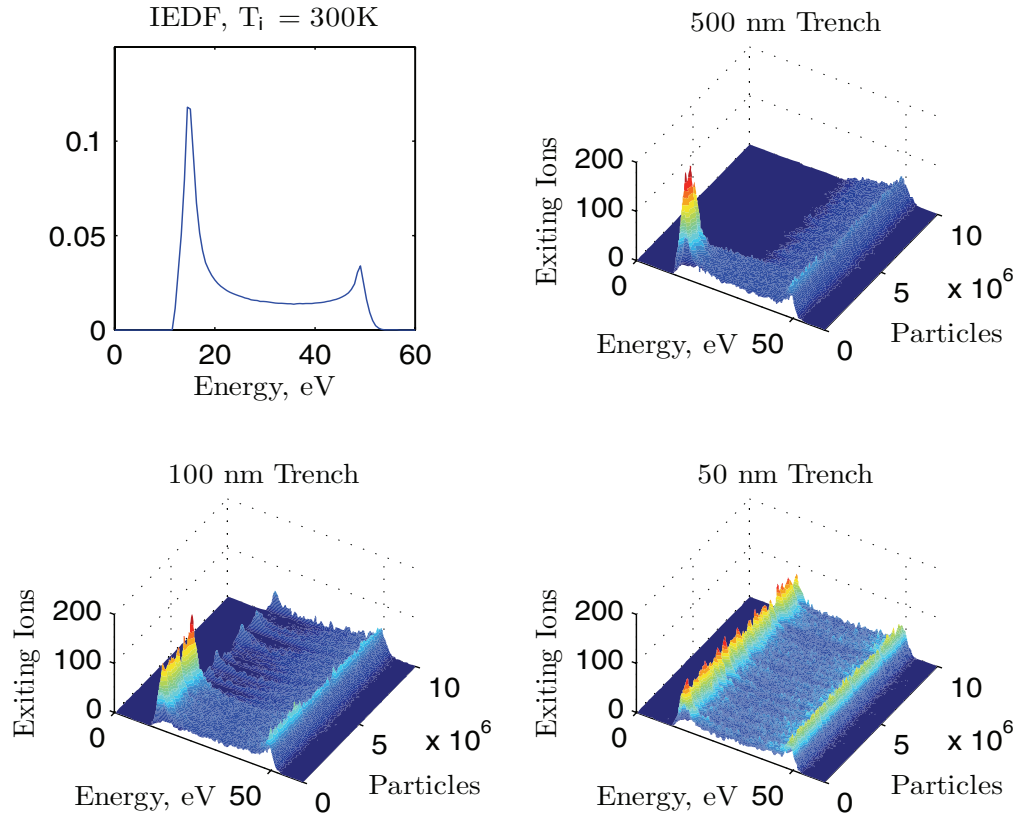


Figure 7.9: Extrusion plots showing numbers and energies of ions reaching the trench exit with the number of combined ions and electrons entering the simulation domain. Intervals of 20,000 combined ions and electrons entering the domain are used between recording of data. The ion energy distribution function of ions entering the simulation domain is also given.  $T_i = 300$  K.

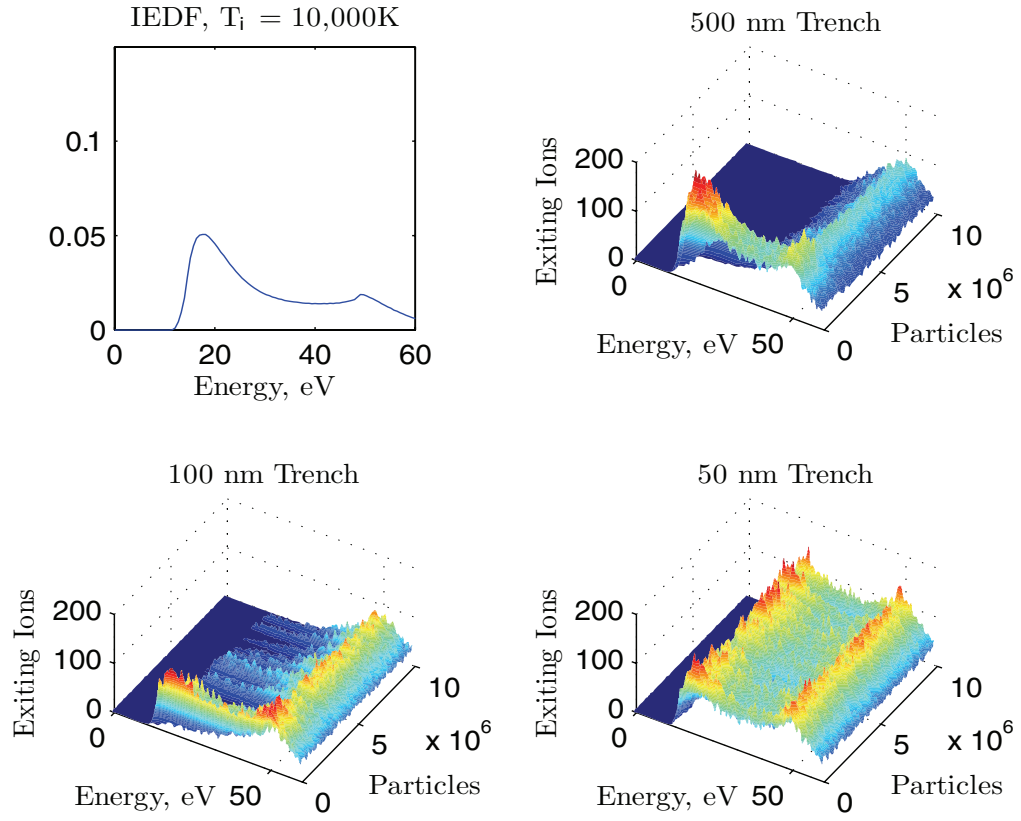


Figure 7.10: Extrusion plots showing numbers and energies of ions reaching the trench exit with the number of combined ions and electrons entering the simulation domain. Intervals of 20,000 combined ions and electrons entering the domain are used between recording of data. The ion energy distribution function of ions entering the simulation domain is also given.  $T_i = 10,000$  K.

## 7.6 Summary

The differential charging of high aspect ratio dielectric trenches under ion and electron bombardment has been investigated using a two-dimensional computational model. Potential distributions in the computational domain were updated after charge transfer from each impinging ion or electron, with explicit treatment of surface charge conduction. This approach allows tracking of the fluctuations in potentials present within the trench region, unlike earlier methods which mostly looked at the steady-state charging behavior of patterned structures at the micron or larger scales, considering average fluxes of ions and electrons for a given period of time.

The results demonstrate oscillations in the potential in high aspect ratio dielectric trenches, with both the magnitude and frequency of the oscillations increasing as the dimensions of the structure decrease. This effect is intertwined with the flux and energies of ions passing through the trench. Low energy species which were unable to reach the trench exit for a large trench width (500 nm) are able to pass through as structures shrink to 100 nm wide and below, with fluctuations mimicking the fluctuations in the potentials. In addition, these results are consistent across a variety of ion temperatures and hence ion angular distributions.

While this two-dimensional model clearly demonstrates the possible occurrence of stochastic surface charging on high aspect ratio dielectric structures, future work will extend this model to three dimensions to note what effect, if any, the additional degree of freedom will have on this oscillating behavior, beyond perhaps a reduction in the absolute dimension at which the onset of the behaviors shown above occur. In addition, heterogeneous dielectric-conductor structures will be considered to more closely approximate

the structures typically encountered in plasma processing systems. The improved understanding of differential surface charging at the nanoscale will provide valuable guidance on applying plasma techniques to the fabrication of future nanostructure-based devices.



## Chapter 8

### Conclusion

The results which have been presented have shown the value of computational modeling efforts to understanding of the transient charging phenomena occurring on the micron- and nanometer-scale. With careful consideration of model components and assumptions and the use of experimental data to validate model results, many insights can be made into the physical processes which occur at interfaces in these systems. In addition, predictions can be made to guide the rational development of these fabrication technologies as processing requirements grow more stringent.

For the ECM-USVP system, the model presented has provided a first look at the nature of the overpotentials and resulting dissolution currents which occur at the liquid-solid interface during nanosecond-scale voltage pulses. This information is given both spatially and temporally and is unavailable by experimental measurement. Also, predictions of etch performance have been made for 1D and 2D systems, with a theoretical treatment made available which demonstrates the relationships between resolution, system geometry, and pulse duration. With one experimental measurement, resolutions can be determined for a variety of tool diameters and pulse durations, and fundamental limitations to decreasing tool diameter or pulse duration can be considered.

For plasma charging of dielectric, the transient behavior of charging processes has been given at a temporal resolution not previously considered.

Beyond obtaining measurements of potential that cannot be made experimentally, this model has revealed the importance in investigating the variation in surface charging behavior at the individual ion and electron level rather than using averaged behavior of many species. With the advent of high aspect ratio heterogeneous structures of small absolute dimension, these transient effects will grow more important and may significantly impact plasma processing technologies currently in use.

## Appendices

## Appendix A

### Electrochemical Fabrication Processes

Electrochemical machining (ECM) is the name given to a variety of processes that use electrochemical means to modify substrate electrodes (workpieces) through use of specially designed tool electrodes and operating conditions which confine the regions where electrochemical reactions occur. In many cases these techniques mimic the tool movements found in traditional physical processes and have been developed to overcome the shortcomings of those processes, thus earning them moniker “machining.” Along with related electrochemical etching and deposition technologies, they have found widespread use with traditional manufacturers and increasingly in microfabrication.

ECM techniques can offer significant advantages over other machining technologies. They are capable of machining hard, brittle materials to high aspect ratio, unlike traditional techniques which require mechanical interaction. In addition, electrochemical dissolution tends to leave surface properties such as composition and crystal orientation unmodified. This is in contrast to thermal methods, such as electrical discharge machining (EDM), which leave heat-affected layers. Thus ECM is a preferred choice for applications in which surface properties are important, and electrochemical methods are often used as a finishing step following other means of modification [52].

Herein several ECM techniques are described along with other electrochemical technologies, with an emphasis on technologies being developed for

microfabrication.

## **A.1 Hole Drilling Processes**

### **A.1.1 Electrochemical Drilling**

Electrochemical drilling (ECD) is perhaps the most common method by which holes are formed through electrochemical means. In this technique, a metal tube serves as the cathode tool, with a concentrated salt electrolyte leaving the tube at high velocity. As dissolution occurs, the tool is lowered into the workpiece, with electrolyte exiting through the small gap between electrodes. This flow of electrolyte reduces heat buildup and serves to remove etch products which otherwise may form precipitates [65].

Holes with diameters ranging from approximately 1.0 to 7.5 mm can be formed via ECD, with aspect ratios up to 20:1. The separation between tool and workpiece is typically 0.025 to 1.3 mm, with an applied voltage ranging from 10 to 30 V. Electrolyte flow in the region between electrodes is maintained between 30 and 60 m/s at temperatures between 24 and 65 C, with the spent electrolyte filtered prior to reuse [48].

In order to reduce stray removal of material from sidewalls, the tube is often coated with an insulating material everywhere except the tip. Spraying or dipping the tool is the most common way of applying insulation, but in some cases a more durable coating is required. In general, the insulating material must (1) adhere to the tool electrode material without forming pores, (2) form a coat with adequate thickness to shield applied potentials of 30 V, (3) be thermally resistant to temperatures of upwards of 200 C during continuous operation, and (4) be chemically resistant to the electrolyte used. In addition, it should have a smooth surface so as not to disrupt the flow of electrolyte,

and its application should not damage or significantly modify the shape of the tool. Teflon, urethane, and epoxy resins are commonly used materials [48].

Material removal rates are a complex function of tool feed rate, electrolyte conductivity, applied potential, and workpiece composition. In a typical scheme, an electrolyte compatible with the workpiece material is selected, and its concentration and other operating parameters are then adjusted until the desired machining results are obtained. Once determined, variation in electrolyte conductivity through changes to its composition and temperature should be minimized with adequate flow and filtration.

In general, linear removal will match the speed of the tool, which typically ranges from 0.25 to 20 mm/min. The feed rate also impacts the separation between electrodes—other quantities being equal, increasing the tool speed causes the frontal gap to shrink until the resulting increase in current produces a linear removal rate matching the new tool velocity. As the side gap is proportional to the frontal gap, an increase in the tool speed will also reduce the side gap, resulting in a smaller hole diameter. Increasing the feed rate in this fashion, however, requires a proportional increase in the power supplied, as  $P = VI$ . Likewise, manipulation of the applied potential can affect power requirements. For example, doubling the voltage while maintaining the same frontal gap will result in a doubling of the current and thus a quadrupling of the required power [48].

### **A.1.2 Shaped Tube Electrochemical Machining**

Shaped tube electrochemical machining (STEM) is essentially a modified electrochemical drilling (ECD) process, originally developed to drill high aspect ratio holes for which ECD processing proved inadequate. Its primary

distinguishing characteristic is the use of a strong acid electrolyte rather than a concentrated salt. This keeps machined workpiece material in solution rather than forming precipitates which may hinder electrolyte flow or cause short circuits between tool and workpiece [65].

Most operating characteristics of STEM are similar to those of ECD. Tool feed rates are generally within a tighter range of 0.75 to 3.0 mm/min, and the required voltage is somewhat lower at 5 to 15 V. Electrolyte pressure is commonly on the range of 275 to 500 kPa. A key difference between STEM and ECD is the necessity for periodic reversals in polarity to prevent the tool from becoming plated with the workpiece material. A typical system has a forward bias for 5 to 10 seconds followed by 75 to 250 ms of reverse bias, with the reverse bias ranging from 10 to 100% of the forward bias [57].

STEM has several advantages and disadvantages when compared with ECD. Its primary advantage is the ability to form holes with aspect ratios of up to 300. In addition, it is capable of drilling somewhat smaller holes than ECD, with diameters as low as 0.5 mm reported [4]. It is also commonly used for creating large numbers of holes, even those of varying diameters and/or not parallel, simultaneously. It is limited, however, in that only corrosion-resistant workpiece and tool materials may be used due to the acid electrolyte. This electrolyte also requires additional handling precautions and gives rise to hazardous waste products [57].

### **A.1.3 Electrochemical Jet Machining**

Electrochemical jet machining (ECJM) is a blanket term describing processes which employ a pressurized electrolyte jet for machining of holes and grooves. These techniques typically use capillary tubes or small nozzles to

confine the flow of electrolyte, but operating pressures, applied voltages, and cathode materials vary greatly between methods. Descriptions of some of the key electrochemical jet machining technologies are given below.

#### **A.1.3.1 Capillary and Electro Stream Drilling**

Capillary drilling (CD), also known as electrochemical fine drilling (ECF), is a technique for forming holes with diameters ranging from 0.2 to 0.5 mm with aspect ratios as high as 100 [4]. It employs a glass capillary surrounding a wire electrode, with electrolyte forced through the annular region at moderate pressure (3-20 bar) onto a workpiece. The wire electrode is typically 1 mm or more from the tube outlet so as not to affect electrolyte flow, necessitating large applied potentials (100-200 V) due to the increased separation between electrodes. Holes are typically etched at rates of 1-4 mm/min, with the tube steadily lowered into the workpiece.

Electro stream drilling (ESD), also known as electro jet drilling (EJD), is a similar method to CD but uses glass tubes drawn down to nozzles leading to fine capillaries. Wire electrodes are again employed, but in this case remain within the tube region rather than entering the capillaries. The longer, narrower path length between electrodes relative to that of CD means substantially larger applied potentials (150-850 V) are required, and thus additional precautions must be taken when insulating the system. Operating pressures and etch rates are comparable to those of CD [56]. ESD is capable of drilling holes as small as 0.125 mm in diameter, smaller than that of CD, but aspect ratios are limited to around 40 [4].

In both CD and ESD, strong acid electrolytes (10-25 wt%) are used to provide a highly conductive medium for current flow and to insure that



dissolved metals do not form precipitates. Despite this, etch rates are typically low for machining of single holes, and thus these techniques are primarily used for machining of arrays of holes in parallel, with several capillaries/tubes fed from a manifold. When used in this arrangement, care must be taken to keep a similar arrangement for the wire electrode location among different elements of the array to prevent differing etch characteristics, particularly in the case of CD. It should also be noted that the spacing of holes in ESD is limited by the size of tubes feeding the capillaries, a limitation not present in CD. Additional limitations for both techniques include waste handling of strong acids, the need for filtration of the feed electrolyte to prevent clogging, and the susceptibility to breakage of the glass capillaries [56].

#### **A.1.3.2 Jet Electrolytic Drilling**

As its name implies, jet electrolytic drilling (JED) also uses jets of pressurized electrolyte to modify substrates, but in this case the nozzle feeding the electrolyte remains above the substrate approximately 2-4 mm rather than being lowered into the substrate during etching. Due to this constant separation, an insulating material is no longer needed to feed the electrolyte, and thus metal nozzles are typically used, doubling as electrodes. As with ESD, the large separation between electrodes requires high applied voltages, in the range of 400-800 V [65].

Higher pressures (10-60 bar) than those used in CD and ESD are required for JED to keep the electrolyte jet tightly focused. Other characteristics are similar to those from CD and ESD, including the use of strong acid electrolytes, low etch rates (0.5-2.0 mm/min) for single holes, and the use of manifolds with multiple nozzles to create multiple holes simultaneously. Likewise,

limitations are largely the same, with filtration of the feed electrolyte often required and special measures taken to insure proper insulation and with waste handling [65].

#### **A.1.3.3 Other ECJM**

In addition to high aspect ratio holes, ECJM has increasingly been used in a variety of micromachining applications. In one approach, a metal nozzle is used as in JED, but the separation between the nozzle and workpiece is less than 0.5 mm. A concentrated salt electrolyte (20 wt%) is employed rather than an acid, at pressures ranging from 5-200 bar. This variance in pressure, along with current densities ranging from 20-200 A/cm<sup>2</sup> and the ability to position the workpiece with an XY stage, provides a range of etch characteristics for both pits and grooves. Applications have included the patterning of rolling bearings with micro indentations to promote oil film formation and the generation of complicated three-dimensional patterns through the use of superposition [44, 55]. In addition, reversing the polarity and using an electrolyte with metal ions can give selective electrodeposition [43].

Another approach has coupled ECJM with laser beams to reduce undercutting in the etching of holes [20]. This method requires the fabrication of a small chamber containing the cathode, an inlet for the electrolyte, and a nozzle outlet with laser aligned along its axis. The localized heating provided by the laser confines the location of the electrochemical reactions beyond that of the jet alone, further reducing stray cutting. Careful consideration of the electrolyte and workpiece materials must be taken, however, as photoelectrochemical and thermal effects may result in unwanted anodic reactions.

## A.2 Surface Finishing

### A.2.1 Electroplating

Electroplating is the controlled deposition of a layer, usually metallic, onto a surface, usually electrically-conductive, to impart improved functionality or appearance. In a typical electroplating system, the surface to be coated is connected as cathode and immersed in an electrolyte bath containing the salt of the metal to be deposited. The positively-charged metallic ions in solution are attracted to the surface cathode and reduced, precipitating to form a layer.

Electroplating operates at potentials at or beyond the onset of reduction, but prior to the onset of parasitic reactions. In a typical voltammogram, a peak is seen in the current density which indicates the optimal bias for maximum plating efficiency. Further increases in the bias will result in parasitic reactions.

Extensive research has gone into methods of surface preparation, the composition of electrolyte baths, and means of controlling current distribution. Surface preparation is critical in electroplating, as even excellent metal coatings can have poor adhesion if the surface contains contaminants from the environment or prior processing or has been chemically altered (e.g. oxide layers). In addition, marks or scratches upon a surface tend to become more pronounced under electroplating rather than being concealed. Treatments include cleaning through use of solvents, abrasive materials, or ultrasonic baths and removal of surface films through acid or alkali solutions.

The electrolyte formulation depends strongly on the metal to be deposited. It should contain a salt of the metal and/or readily accept it from dissolving anode(s). In addition, a variety of complexing agents, surfactants,

and inhibitors may be present to promote smooth and bright deposits. Hence, complex salts such as cyanide complexes are often employed. To illustrate the variety of formulations, we consider the case of copper. Alkaline cyanide copper solutions are often used to make initial deposits (“strikes”), owing to their ability to plate thin layers of uniform thickness onto a variety of cathode materials (This ability to produce uniform layers is often referred to as the “throwing power” of a bath). Acidic copper solutions such as that of copper sulfate and sulfuric acid may then be used following the strike to plate thicker layers of copper. Alternately, an alkaline pyrophosphate copper bath is sometimes employed, with or without a strike, depending on the substrate material [74].

Control of current distribution at the cathode surface is an essential aspect of obtaining a uniform coating. There is a tendency for complex cathode shapes to have their protrusions preferentially coated due to the increased current density in those locations relative to other features. As mentioned above, this effect can somewhat be overcome through the use of inhibitors, which have a higher convective flux to protrusions. Equally important are the number and placement of anodes, as well as modifications to the current density supplied. For highly irregularly-shaped objects, an alternative process known as electroless plating may be employed. This method involves an autocatalytic reaction at the substrate surface without the use of electrodes and typically results in uniform coverage.

As electroplating has been practiced commercially since the mid 19th Century, it has a wide variety of applications. Perhaps its most common use is to improve the corrosion resistance of metals such as iron and steel by applying coatings such as zinc and chromium. It is also commonly used to deposit gold

or silver on jewelry and silver on utensils as well as for the plating of silver, copper, and brass in electrical connectors. Other metals used as coatings include nickel, iron, cadmium, indium, tin, and lead.

### **A.2.2 Electrochemical Polishing**

Electrochemical polishing, sometimes referred to as electropolishing or reverse electroplating, is the controlled anodic leveling and/or brightening of a conductive surface, often resulting in improved surface properties and increased reflectivity. In this process, the surface to be modified is immersed in electrolyte and a bias applied, with the surface as anode. The non-uniform current distribution, resulting from the protrusions and recessions of the surface, gives rise to different rates of dissolution, with surface peaks preferentially removed [19].

Electrochemical polishing typically uses concentrated acid electrolyte mixtures and a bias falling within the range of potentials at which a current density plateau is reached, which varies depending on the anode material and electrolyte composition. It is generally agreed that, at these potentials, the electrochemical reactions are mass transport-limited, although there is some contention as to the rate-limiting species and transport mechanisms. In some systems, particularly those with a high rate of dissolution and a neutral electrolyte, metal ions from the anodic dissolution exceed the solubility limit, giving rise to the precipitation of a salt film. Further dissolution is then limited by diffusion of ions into the bulk electrolyte. With acid electrolytes, however, it has been posited that a viscous liquid boundary layer forms at the anode, restricting the diffusion of an acceptor species to the anode interface [59].

The primary benefit of electrochemical polishing is a reduction in sur-

face roughness. It typically outperforms mechanical polishing methods, giving a smoother surface without leaving behind directionally-oriented effects. For optimal performance, however, careful positioning of the cathode may be required, as macroscopic unevenness can be introduced by the electrochemical process. The term “leveling” is generally applied when the surface roughness is decreased to the micron range and larger. A further reduction to the sub-micron range, accompanied by specular reflectivity, is termed “brightening.” To achieve the latter, the dissolution mechanism must be independent of crystallographic orientation, hence the importance of operating conditions which are transport-limited rather than under activation control [45]. Electrochemical polishing is also useful for the removal of surface layer imperfections, such as burrs, weld scale, heat treatment discoloration, and residual material from grinding. Its primary disadvantages are related to the toxic, highly corrosive acid electrolytes typically used, which may require special handling as well as generating hazardous waste products.

Electrochemical polishing has most often been used on stainless steel, where a commercial process involving a concentrated phosphoric acid and sulfuric acid mixture has been employed worldwide [1]. Applications have ranged from engine parts to medical devices to equipment in pharmaceutical facilities. A variety of other metals have also been commercially electropolished, including copper, nickel, and titanium. Recently, electropolishing has been investigated as a means of removing excess copper following damascene processes in copper interconnect fabrication, replacing chemical mechanical planarization of potentially fragile low-k dielectrics [70]. It has also been used as a finishing step to remove burrs and improve surface roughness following EDM [28].

## **A.3 Electroforming**

Electroforming is the formation of three-dimensional shapes through the use of electrochemical deposition. It differs from other plating processes in that the cathode substrate is a mold, to be removed from the deposited layer. As such, it adds an additional requirement that the cathode and plating material be easily separable. Electroforming allows for unmatched precision in the reproduction of fine details from mold to part, but it is an expensive, slow process.

Molds, or mandrels, used in electroforming fall into two categories, permanent and expendable. Permanent molds are typically metallic, but conductive plastics are sometimes employed. The 300-series stainless steels are often chosen due to their naturally passive surfaces, but copper or brass may also be used if passivated with a chromium layer. Care must be taken in handling of permanent molds, as excessive wear or scratches will be reproduced in the part. Expendable mandrels may be fabricated out of a variety of materials, but aluminum is a popular choice due to the ease of machining and polishing and ability to be dissolved easily in caustic solutions [51].

Electroforming applications include the fabrication of the main combustion chamber of the space shuttle, heart pump components, artificial joint implants, and cold welding of dissimilar metals.

## **A.4 Microfabrication**

### **A.4.1 Masked Processes**

For a large number of microfabrication applications, traditional electrochemical methods are not applicable due to the inability to localize reactions.

A common method to overcome this barrier is the application of surface masks, which selectively protect substrate areas in a fashion similar to their use in plasma and chemical etching processes. Both electrochemical dissolution and deposition can then be used on the exposed surface regions.

For dissolution applications, neutral salt electrolytes are used, along with a tool capable of applying uniform current distribution and a large, uniform rate of mass transport to the unprotected anode surface. With such a tool, lateral etching may be controlled, allowing for anisotropic (unidirectional) etching of high aspect ratio structures. This differs from wet etching processes, which typically use aggressive acid solutions and result in isotropic etching and undercutting of the mask(s). In addition, the neutral salt electrolyte solutions are easily filtered and do not result in hazardous waste or require special handling. The process also generally gives higher throughput and a better surface finish than wet etching but is susceptible to island formation as a result of a loss of electrical contact. Dissolution applications include ink-jet nozzle plates, conducting lines for printed circuit boards, and metal masks, such as the aperture masks used in some color CRTs [18].

Through-mask deposition requirements closely mirror those of general electroplating applications. Electrolyte solutions contain salts of the metal ion to be deposited along with additives to promote smooth, uniform film growth through control of mass transport and current distribution. Alternately, electroless plating may be used. Masks are typically applied after deposition of any seed layers, so as not to promote growth upon the masks [8]. Applications include through holes and vias for printed circuit boards and thin film recording heads used in magnetic recording hardware [7].

Masks are also often used in micro-electroforming, where they can act



as the mold on top of a suitable cathode material. As with electroforming, however, micro-electroforming is a relatively expensive process, not suitable for low end applications. Micro-electroforming is a key component of the LIGA process used in fabrication of MEMS [62] and is also used in the mass replication of CDs and DVDs, where the electroformed piece itself becomes a mold [69].

#### **A.4.2 Damascene Process**

The damascene process [8] is a method of fabricating copper interconnects in microelectronic devices through use of electroplating. It was developed out of a desire to replace aluminum interconnects and the inability to plasma etch copper substrates. Its primary advantages over other techniques (such as the use of surface masks) are the plating of copper directly onto functional parts of the devices and the ability to inlay via holes and trenches in a single deposition step, known as dual damascene processing. The damascene process was developed at IBM in the early 1990s, with replacement of vacuum-deposited aluminum occurring in 1997. Since that time, most leading chip manufacturers have switched to electroplated copper technologies.

The damascene process involves a series of deposition, masking, and removal steps using a variety of technologies. In a typical process, one or more insulator layers are vacuum-deposited, separated by etch stop layers. Resist masks are applied, plasma etching of the insulator layers occurs, and the masks removed. A barrier layer is then applied to the patterned insulator, followed by a seed layer of copper. Next, copper is electroplated onto the insulator, usually significantly overfilling the structure. Chemical-mechanical polishing is then used to remove the excess copper and planarize the structure. This

entire process may then be repeated multiple times, resulting in a multi-layer device.

The electroplating step in the damascene process has been developed to exhibit superconformal deposition of copper through use of proprietary additives. In this type of deposition, copper is preferentially deposited at the bottoms of the trench and via structures, allowing for fillings free of defects such as the voids seen in subconformal deposition and seams arising from conformal processes. Such fillings improve the reliability of the copper interconnects, significantly reducing certain diffusion pathways for copper electromigration.

#### **A.4.3 Pulsed Electrochemical Machining**

In addition to using fine jets and masked surfaces, electrochemical machining has increasingly turned to the use of pulsed voltage sources to confine electrochemical reactions on the workpiece [5, 63, 72]. In this method, the tool electrode (often an STM tip) is given a negative bias for a short duration, resulting in the localized charging of the electrochemical double layers in regions where the tool and workpiece electrodes are in close proximity. The resulting localized overpotential drives the selective dissolution of material at the workpiece, with resolutions on the sub-micron level possible. The bias is then removed for a duration sufficient to allow the double layers to discharge before a new pulse is initiated. This technique is being considered for the production of micro-electro-mechanical systems (MEMS), for high aspect ratio etching, for 3D etching, and for biomedical applications

Pulsed ECM processes rely on the similarity of electrochemical systems to resistor-capacitor (RC) circuits during the transient phase. The electrolyte represents a resistance, which varies based on the differing current pathlengths

between regions of the tool and workpiece. The electrochemical double layers at both the tool and workpiece may be considered as capacitors, with different regions charging at different rates owing to the variation in the local current during the pulse. Thus, a particular pulse duration can be compared with the time constants of these RC circuits with varying electrolyte resistance in order to approximate the range at which electrochemical modification will occur.

A variety of substrate and tool materials, electrolytes, and operating conditions have been used in pulsed ECM systems. Copper and stainless steel have been most commonly etched workpieces, but doped semiconductors have also been shown capable of modification. Tool electrodes have been fashioned from Pt or Ti wires and may be simple cylinders or in the form of a complex template to be communicated to the substrate.

While pulse durations are sometimes as large as 5 ms, values are more typically under 100 ns, with current state-of-the-art systems capable of generating pulses on the order of 1 ns [41]. The length of the pause following the pulse is often given as a ratio, with a 1:10 pulse:pause ratio the most commonly used value. Applied potentials fall in the range of 1-10 V, thus no additional precautions need to be taken when insulating the system. A wide range of electrolytes and concentrations have been demonstrated to allow dissolution of the workpiece to occur. These include hydrochloric acid, copper sulfate + sulfuric acid, copper sulfate + hydrofluoric acid, and hydrofluoric acid + sulfuric acid, among others, with acid concentrations ranging from 0.01 M to 6 M depending on the workpiece material.

Extensive numerical studies have been performed on this technique [31–33, 35] to validate the analogy of the system to that of an RC circuit and to predict its performance. The experimental current response upon the applica-

tion of the pulse and the onset of the pause have been shown to match that of a model system of electrochemical double layers represented as capacitors in parallel, with the tool and workpiece capacitors connected by a mesh of resistors representing the electrolyte. Experimental data at varying pulse durations for the gap between tool and workpiece following a lateral etch has also been captured numerically, along with the identification of one-, two-, and three-dimensional etching regimes based on the ratio of tool diameter to etch resolution.

## Appendix B

### Product Effect on Electrolyte Resistivity

To determine if the effect of dissolution products on electrolyte resistivity is substantial, the worst-case system geometry and mass transport situation are considered. This entails a hole drilling process with a small gap between tool and substrate forming an annular region from which etch product must diffuse, as illustrated in Figure B.1. For this calculation, parameters matching those of the computational work are used: a 10  $\mu\text{m}$  diameter tool with velocity 1.5  $\mu\text{m}/\text{min}$  is etched into a copper substrate to a depth of 40  $\mu\text{m}$ , in the presence of a 0.1 M  $\text{CuSO}_4$ /0.075 M  $\text{H}_2\text{SO}_4$  electrolyte. The gap spacing is 3  $\mu\text{m}$ , similar to that of the shortest pulse duration considered, 25 ns.

Assuming pseudo-steady-state conditions and a cylindrical bottom to the hole, the volume removal rate  $\dot{V}$  is given by

$$\dot{V} = v_{tool} r_{hole}^2 \pi, \quad (\text{B.1})$$

where  $v_{tool}$  is the velocity of the tool and  $r_{hole}$  is the hole radius. Using the density of the substrate  $\rho_s$  and its molecular weight  $M_s$ , the rate at which moles of substrate enter the electrolyte solution is

$$F_s = \frac{v_{tool} r_{hole}^2 \rho_s \pi}{M_s} \quad (\text{B.2})$$

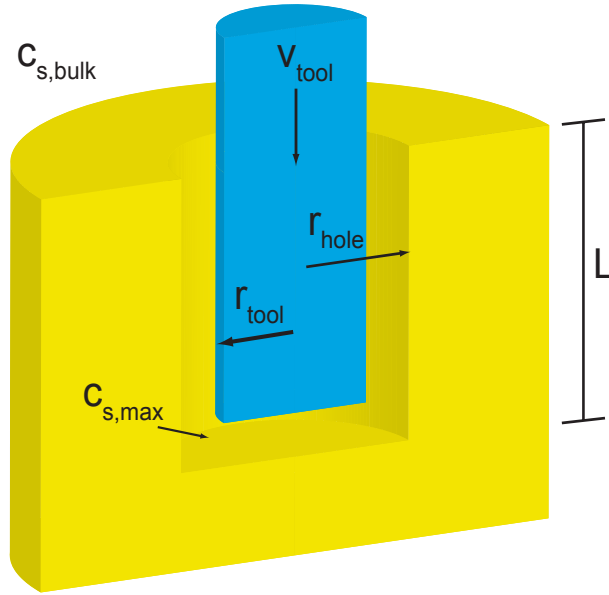


Figure B.1: Schematic of the geometry used to calculate the influence of dissolution products on electrolyte resistivity.

The flux is then given by dividing by the area of annular region:

$$\begin{aligned}
 N_s &= \frac{v_{tool} r_{hole}^2 \rho_s \pi}{M_s (r_{hole}^2 - r_{tool}^2) \pi} \\
 &= \frac{v_{tool} \rho_s}{M_s [1 - (\frac{r_{tool}}{r_{hole}})^2]}
 \end{aligned} \tag{B.3}$$

For small mole fractions of substrate in water, this is equivalent to

$$N_s = -c \mathcal{D}_s \nabla x_s = -\mathcal{D}_s \nabla c_s \tag{B.4}$$

Combining gives

$$\begin{aligned}
 \frac{v_{tool} \rho_s}{M_s [1 - (\frac{r_{tool}}{r_{hole}})^2]} &= -\mathcal{D}_s \nabla c_s \\
 &= \frac{\mathcal{D}_s (c_{s,max} - c_{s,bulk})}{L}
 \end{aligned} \tag{B.5}$$

where  $\mathcal{D}_s$  is the diffusivity of the substrate species in water,  $c_{s,max}$  is the maximum concentration of the substrate species,  $c_{s,bulk}$  is its concentration in the bulk electrolyte, and  $L$  is the length of the diffusion pathway, which equals the depth of the hole.

For a copper substrate,  $\mathcal{D}_s$  is  $7.3 \cdot 10^{-6} \text{ cm}^2/\text{s}$ ,  $\rho_s$  is  $8.92 \text{ g/cm}^3$ , and the molecular weight is  $63.546 \text{ g/mol}$ . The gap spacing of  $3 \text{ }\mu\text{m}$  gives a hole diameter of  $8 \text{ }\mu\text{m}$ . These values combine to give

$$\frac{c_{s,max} - c_{s,bulk}}{L} = 7.89 \cdot 10^{-3} M \text{ }\mu\text{m}^{-1} \quad (\text{B.6})$$

For a  $40 \text{ }\mu\text{m}$  hole depth, the increase in concentration relative to the bulk solution is  $0.316 \text{ M}$ . If we assume the contribution to the resistivity is essentially additive with the copper sulfate component, this gives the equivalent of a  $0.416 \text{ M CuSO}_4/0.075 \text{ M H}_2\text{SO}_4$  electrolyte, which has an estimated resistivity of  $21.3 \text{ }\Omega\cdot\text{cm}$ . This compares with the original solution resistivity of  $27.7 \text{ }\Omega\cdot\text{cm}$ , giving a decrease of  $\sim 25\%$ .

## Appendix C

### Electrolyte Resistivity Calculation

As mixed salt/acid electrolytes are used in many ECM-USVP systems, calculation of the electrolyte resistivity is not as straightforward as would be the case with a pure acid or salt electrolyte. With a pure electrolyte, one can refer to tables of electrolyte conductance as a function of concentration and interpolate to find the conductance for a given concentration. With a mixed electrolyte, one cannot simply interpolate for each species and add the resulting conductances, as the equivalent conductance ( $\Lambda$  [ $\Omega^{-1}\cdot\text{cm}^2\cdot\text{equiv}^{-1}$ ]) decreases with increasing concentration. As a trivial counterexample, consider that the electrolyte were made up of 0.025 M  $\text{H}_2\text{SO}_4$  combined with 0.025 M  $\text{H}_2\text{SO}_4$  and compare the added conductivity  $\kappa_{add}$  ( $= 2 \times 0.01265 = 0.0253 \Omega^{-1}\cdot\text{cm}^{-1}$ ) with the experimentally reported  $\kappa_{exp}$  ( $= 0.0225 \Omega^{-1}\cdot\text{cm}^{-1}$ ).

For the computational model, which focused on mixtures of  $\text{CuSO}_4$  and  $\text{H}_2\text{SO}_4$ , the following approach was adopted. First, equivalent conductance data for each species was collected at a variety of concentrations, and a cubic spline relating conductivity and concentration was constructed for each, of the form  $\kappa(C)$ . Next, unknown conductivities were determined for concentrations to be used in the computational model mixtures, considering the components separately. The conductivities were then used to obtain an equivalent concentration of the other species, using splines of the form  $C(\kappa)$ . This was followed by adding the generated concentration to the concentration of



the other solution component, and the conductivity of the “pure” mixture was determined from the spline  $\kappa(C)$ . The two resulting estimates of conductivity were then arithmetically averaged to give the estimated conductivity, with the reciprocal taken to give the resistivity.

As an example, consider a mixture of 0.1 M  $\text{CuSO}_4$  and 0.075 M  $\text{H}_2\text{SO}_4$ . Cubic splines report the conductivities of the pure species as  $7.35 \cdot 10^{-3}$  and  $32.1 \cdot 10^{-3} \Omega^{-1} \cdot \text{cm}^{-1}$ , respectively. The equivalent  $\text{H}_2\text{SO}_4$  concentration for 0.1 M  $\text{CuSO}_4$  is determined to be 0.0133 M using the  $C(\kappa)$  spline for  $\text{H}_2\text{SO}_4$ . In a similar fashion, the equivalent  $\text{CuSO}_4$  concentration for 0.075 M  $\text{H}_2\text{SO}_4$  is found as 0.711 M. Now, adding the concentrations for each species gives two approximations of the solution strength: 0.811 M  $\text{CuSO}_4$  and 0.0883 M  $\text{H}_2\text{SO}_4$ . The original  $\kappa(C)$  splines are then used again to obtain estimates of the mixture conductivity, in this case  $35.0 \cdot 10^{-3}$  and  $37.3 \cdot 10^{-3} \Omega^{-1} \cdot \text{cm}^{-1}$  according to the  $\text{CuSO}_4$  and  $\text{H}_2\text{SO}_4$  concentrations, respectively. These values are averaged to give a conductance of  $36.1 \cdot 10^{-3} \Omega^{-1} \cdot \text{cm}^{-1}$ , and the reciprocal gives the solution resistivity of  $27.7 \Omega \cdot \text{cm}$ .

The estimates of the resistivities of 0.1 M  $\text{CuSO}_4$  mixtures with  $\text{H}_2\text{SO}_4$  of varying concentration are given in Figure C.1.

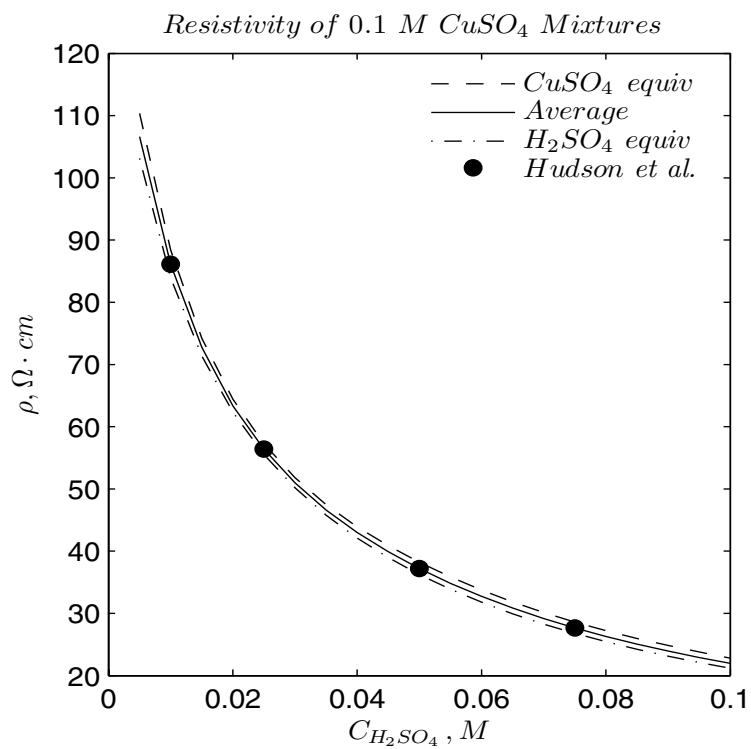


Figure C.1: Resistivity with  $\text{H}_2\text{SO}_4$  concentration for 0.1 M  $\text{CuSO}_4$  mixtures. Lines indicate estimates according to  $\text{CuSO}_4$  and  $\text{H}_2\text{SO}_4$  equivalents and their average. Dots represent the solutions used in [72].

## Appendix D

### Capacitance Calculation

One issue that arises due to the varying lengths of connections to the substrate and tool electrodes is the handling of capacitance, as illustrated in Figure D.1. Here, a single node has two connections to the substrate, with the connection made in the  $x$  direction longer than that of the  $z$  direction, giving  $R_x > R_z$ . Once the initial potential at the node is found upon application of a voltage pulse, it is clear that the initial current flowing through the capacitor connected in the  $z$  direction will be larger than that of the  $x$  direction. If  $C_x$  and  $C_z$  are considered equal or differences are based only on surface topology, the capacitors will charge at different rates owing to differences in the time constants  $R_x C_x$  and  $R_z C_z$ . This will give inconsistent overpotentials along the surface, which should clearly not be the case if, for example, the surface is a straight line (2D) or flat plane (3D).

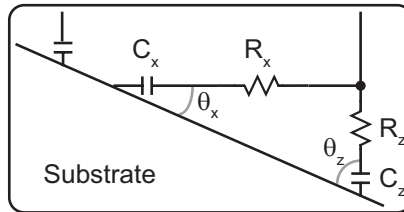


Figure D.1: Illustration of varying resistances of connections made to the substrate electrode in the  $x$  and  $z$  directions. The angle formed by a connection to the substrate helps to determine the capacitance of the connection.

A solution to how the capacitances should be treated was constructed by considering the following. (1) Connections made perpendicularly to a flat surface should have the full capacitance according to the area of the mesh cell. Thus, the capacitance for a connection made in the  $z$  direction is found by multiplying the capacity by the lengths of the mesh in the  $x$  and  $y$  dimensions. (2) Connections from a single node to two locations along a flat surface should have the same time constant. Hence, the ratio of the capacitances should be the inverse of the ratio of the resistances. From this condition, it becomes clear that both the surface geometry and direction of approach are relevant for determining the capacitance. Connecting the two conditions, the capacitance is given by multiplying the full capacitance of a connection made perpendicular to a flat surface by the sine of the angle formed by the connection to the surface.

# Appendix E

## Particle Trajectory Calculation

Particle trajectories are tracked through use of the equations of motion for a charged particle in an electric field:

$$m \frac{d\mathbf{v}}{dt} = q\mathbf{E} \quad (\text{E.1})$$

$$\frac{d\mathbf{x}}{dt} = \mathbf{v}, \quad (\text{E.2})$$

where  $m$  is the particle mass,  $\mathbf{v}$  is the particle velocity,  $q$  is the particle charge,  $\mathbf{E}$  is the local electric field, and  $\mathbf{x}$  is a vector denoting the particle position. The electric field is calculated at mesh points using finite differences on the potentials. The field local to the particle is then given by an equation of the form

$$\mathbf{E} = (1 - \bar{x})(1 - \bar{z})\mathbf{E}_{0,0} + (\bar{x})(1 - \bar{z})\mathbf{E}_{1,0} + (1 - \bar{x})(\bar{z})\mathbf{E}_{0,1} + (\bar{x})(\bar{z})\mathbf{E}_{1,1} \quad (\text{E.3})$$

where  $\mathbf{E}_{\mathbf{x},\mathbf{z}}$  are the electric field vectors at corners of the cell containing the particle and  $\bar{x}, \bar{z}$  are the relative positions of the particle within the cell, normalized by the  $x$  and  $z$  mesh lengths, respectively.

Fourth-order Runge-Kutta is used with the equations of motion, with the vectors broken down into their components:  $\mathbf{v}$  to  $v_x$  and  $v_z$ ,  $\mathbf{E}$  to  $E_x$  and  $E_z$ , and  $\mathbf{x}$  to  $x$  and  $z$ . To simplify the expressions,  $x$  and  $z$  are considered relative to their position within the cell, such that  $x \in [0, h_x]$  and  $z \in [0, h_z]$ ,

where  $h_x$  and  $h_z$  are the mesh lengths in the  $x$  and  $z$  directions, respectively.

The equations are then given by:

$$k_{11} = \Delta t f(x_0, z_0) \tag{E.4}$$

$$k_{12} = \Delta t g(x_0, z_0)$$

$$k_{13} = \Delta t h(v_{x0})$$

$$k_{14} = \Delta t j(v_{z0})$$

$$k_{21} = \Delta t f(x_0 + \frac{k_{13}}{2}, z_0 + \frac{k_{14}}{2})$$

$$k_{22} = \Delta t g(x_0 + \frac{k_{13}}{2}, z_0 + \frac{k_{14}}{2})$$

$$k_{23} = \Delta t h(v_{x0} + \frac{k_{11}}{2})$$

$$k_{24} = \Delta t j(v_{z0} + \frac{k_{12}}{2})$$

$$k_{31} = \Delta t f(x_0 + \frac{k_{23}}{2}, z_0 + \frac{k_{24}}{2})$$

$$k_{32} = \Delta t g(x_0 + \frac{k_{23}}{2}, z_0 + \frac{k_{24}}{2})$$

$$k_{33} = \Delta t h(v_{x0} + \frac{k_{21}}{2})$$

$$k_{34} = \Delta t j(v_{z0} + \frac{k_{22}}{2})$$

$$k_{41} = \Delta t f(x_0 + k_{33}, z_0 + k_{34})$$

$$k_{42} = \Delta t g(x_0 + k_{33}, z_0 + k_{34})$$

$$k_{43} = \Delta t h(v_{x0} + k_{31})$$

$$k_{44} = \Delta t j(v_{z0} + k_{32})$$

$$\begin{aligned}
v_x &= v_{x0} + \frac{1}{6}(k_{11} + 2k_{21} + 2k_{31} + k_{41}) \\
v_z &= v_{z0} + \frac{1}{6}(k_{12} + 2k_{22} + 2k_{32} + k_{42}) \\
x &= x_0 + \frac{1}{6}(k_{13} + 2k_{23} + 2k_{33} + k_{43}) \\
z &= z_0 + \frac{1}{6}(k_{14} + 2k_{24} + 2k_{34} + k_{44}),
\end{aligned}$$

where

$$\begin{aligned}
f(x, z) &= \frac{q}{m} \frac{E_{x0,0}(h_x - x)(h_z - z) + E_{x1,0}x(h_z - z) + E_{x0,1}(h_x - x)z + E_{x1,1}xz}{h_x h_z} \\
g(x, z) &= \frac{q}{m} \frac{E_{z0,0}(h_x - x)(h_z - z) + E_{z1,0}x(h_z - z) + E_{z0,1}(h_x - x)z + E_{z1,1}xz}{h_x h_z} \\
h(v_x) &= v_x \\
j(v_z) &= v_z
\end{aligned}$$

and the subscript 0 indicates the value at the beginning of a time step,  $\Delta t$ . The time step is initialized such that the particle moves at most one-tenth of a mesh length in the  $x$  and  $z$  directions, based on the initial velocity components. A subsequent check insures movement of no more than one-fourth of the mesh length in either direction or the time step is reduced and the trajectory recalculated.

The equations of motion are used as given above. Additional terms could be added to correct for the change in the electric field as the particle moves during a given time-step, but those fields are already updated for all four calculations during one Runge-Kutta time-step. A Taylor series expansion of the particle position in one dimension demonstrates the nature of the additional terms:

$$x = x_0 + x'_0 \Delta t + x''_0 \frac{(\Delta t)^2}{2!} + x'''_0 \frac{(\Delta t)^3}{3!} + \dots, \quad (\text{E.5})$$

where  $x$  is the particle position,  $x_0$  is the initial position,  $x'_0$  is the initial velocity, and  $x''_0$  is given by Equation E.1. Later coefficients are generated by further differentiating Equation E.1, keeping in mind that  $\frac{d}{dt} = \frac{\partial}{\partial t} + (\mathbf{v} \cdot \nabla)$ . Thus,

$$\begin{aligned} x'''_0 &= \frac{d(\frac{q}{m}E_x)}{dt} \\ &= \frac{q}{m} \left[ \frac{\partial(E_x)}{\partial t} + v_x \nabla E_x \right]_{t=t_0} \\ &= \frac{q}{m} \left[ 0 + v_{x_0} \frac{dE_x}{dx} \right], \end{aligned}$$

giving

$$x = x_0 + v_{x_0} \Delta t + \frac{q}{m} E_x \frac{(\Delta t)^2}{2!} + \frac{q}{m} v_{x_0} \frac{dE_x}{dx} \frac{(\Delta t)^3}{3!} + \dots \quad (\text{E.6})$$



## Bibliography

- [1] A. P. Abbott, G. Capper, K. J. McKenzie, and K. S. Ryder. Voltammetric and impedance studies of the electropolishing of type 316 stainless steel in a choline chloride based ionic liquid. *Electrochimica Acta*, 51(21):4420–4425, 2005.
- [2] D. Adalsteinsson and J. A. Sethian. A fast level set method for propagating interfaces. *Journal of Computational Physics*, 118(2):269–277, 1995.
- [3] D. Adalsteinsson and J. A. Sethian. The fast construction of extension velocities in level set methods. *Journal of Computational Physics*, 148(1):2–22, 1999.
- [4] M. S. Ahmed. Modern applications of EDM and ECM. In *IEEE Manufacturing Technology Update*, pages 1–14, 1993.
- [5] S. H. Ahn, S. H. Ryu, D. K. Choi, and C. N. Chu. Electro-chemical micro drilling using ultra short pulses. *Precision Engineering*, 28(2):129–134, 2004.
- [6] P. Allongue, P. Jiang, V. Kirchner, A. L. Trimmer, and R. Schuster. Electrochemical micromachining of p-type silicon. *Journal of Physical Chemistry B*, 108(38):14434–14439, 2004.
- [7] P. C. Andricacos and N. Robertson. Future directions in electroplated materials for thin-film recording heads. *IBM Journal of Research and*

- Development*, 42(5):671–680, 1998.
- [8] P. C. Andricacos, C. Uzoh, J. O. Dukovic, J. Horkans, and H. Deligianni. Damascene copper electroplating for chip interconnections. *IBM Journal of Research and Development*, 42(5):567–574, 1998.
  - [9] J. C. Arnold and H. H. Sawin. Charging of pattern features during plasma-etching. *Journal of Applied Physics*, 70(10):5314–5317, 1991.
  - [10] A. J. Bard and L. R. Faulkner. *Electrochemical Methods: Fundamentals and Applications*, pages 546–554. Wiley, New York, 2nd edition, 2001.
  - [11] A. J. Bard and L. R. Faulkner. *Electrochemical Methods: Fundamentals and Applications*, pages 9–10. Wiley, New York, 2nd edition, 2001.
  - [12] A. J. Bard and L. R. Faulkner. *Electrochemical Methods: Fundamentals and Applications*, pages 100–101. Wiley, New York, 2nd edition, 2001.
  - [13] A. J. Bard and L. R. Faulkner. *Electrochemical Methods: Fundamentals and Applications*, pages 102–103. Wiley, New York, 2nd edition, 2001.
  - [14] A. J. Bard and L. R. Faulkner. *Electrochemical Methods: Fundamentals and Applications*, pages 97–98. Wiley, New York, 2nd edition, 2001.
  - [15] A. Barkan, N. Dangelo, and R. L. Merlino. Charging of dust grains in a plasma. *Physical Review Letters*, 73(23):3093–3096, 1994.
  - [16] P.M. Bellan. *Fundamentals of Plasma Physics*, pages 3–4. Cambridge University Press, Cambridge, 2006.
  - [17] J.O’M. Bockris, A.K.N. Reddy, and M.E. Gamboa-Aldeco. *Modern Electrochemistry 2A: Fundamentals of Electrode Processes*, pages 1055–1057. Kluwer-Plenum, New York, 2nd edition, 2000.

- [18] M. Datta. Microfabrication by electrochemical metal removal. *IBM Journal of Research and Development*, 42(5):655–669, 1998.
- [19] M. Datta and D. Landolt. Fundamental aspects and applications of electrochemical microfabrication. *Electrochimica Acta*, 45(15-16):2535–2558, 2000.
- [20] M. Datta, L. T. Romankiw, D. R. Vigliotti, and R. J. Vongutfeld. Jet and laser-jet electrochemical micromachining of nickel and steel. *Journal of the Electrochemical Society*, 136(8):2251–2256, 1989.
- [21] D. J. Economou and R. C. Alkire. Effect of potential-field on ion deflection and shape evolution of trenches during plasma-assisted etching. *Journal of the Electrochemical Society*, 135(4):941–949, 1988.
- [22] H. B. Garrett. The charging of spacecraft surfaces. *Reviews of Geophysics*, 19(4):577–616, 1981.
- [23] H. Gerischer, D. M. Kolb, and J. K. Sass. Study of solid-surfaces by electrochemical methods. *Advances in Physics*, 27(3):437–498, 1978.
- [24] R. A. Gottscho, C. W. Jurgensen, and D. J. Vitkavage. Microscopic uniformity in plasma-etching. *Journal of Vacuum Science & Technology B*, 10(5):2133–2147, 1992.
- [25] K. Hashimoto. Charge damage caused by electron shading effect. *Japanese Journal of Applied Physics*, 33(10):6013–6018, 1994.
- [26] P. A. Heimann and J. E. Olsen. A sensitive method for measuring surface conductivity of insulators. *Journal of Applied Physics*, 53(1):546–549, 1982.

- [27] M.R. Hestenes and E. Stiefel. Methods of conjugate gradients for solving linear systems. *Journal of Research of the National Bureau of Standards*, 49(6):409–436, 1952.
- [28] J. C. Hung, B. H. Yan, H. S. Liu, and H. M. Chow. Micro-hole machining using micro-EDM combined with electropolishing. *Journal of Micromechanics and Microengineering*, 16(8):1480–1486, 2006.
- [29] G. S. Hwang and K. P. Giapis. On the origin of the notching effect during etching in uniform high density plasmas. *Journal of Vacuum Science & Technology B*, 15(1):70–87, 1997.
- [30] S. Iwata and A. Ishizaka. Electron spectroscopic analysis of the SiO<sub>2</sub>/Si system and correlation with metal-oxide-semiconductor device characteristics. *Journal of Applied Physics*, 79(9):6653–6713, 1996.
- [31] J. A. Kenney and G. S. Hwang. Electrochemical machining with ultra-short voltage pulses: modelling of charging dynamics and feature profile evolution. *Nanotechnology*, 16:S309–S313, 2005.
- [32] J. A. Kenney and G. S. Hwang. Computational analysis of intratool interactions in electrochemical micromachining with multitip tool electrodes. *Electrochemical and Solid State Letters*, 9(9):D21–D23, 2006.
- [33] J. A. Kenney and G. S. Hwang. Etch trends in electrochemical machining with ultrashort voltage pulses - predictions from theory and simulation. *Electrochemical and Solid State Letters*, 9(1):D1–D4, 2006.
- [34] J. A. Kenney and G. S. Hwang. Prediction of stochastic behavior in differential charging of nanopatterned dielectric surfaces during plasma processing. *Journal of Applied Physics*, 2006. (accepted).

- [35] J. A. Kenney, G. S. Hwang, and W. Shin. Two-dimensional computational model for electrochemical micromachining with ultrashort voltage pulses. *Applied Physics Letters*, 84(19):3774–3776, 2004.
- [36] B. H. Kim, B. J. Park, and C. N. Chu. Fabrication of multiple electrodes by reverse EDM and their application in micro ECM. *Journal of Micromechanics and Microengineering*, 16(4):843–850, 2006.
- [37] B. H. Kim, S. H. Ryu, D. K. Choi, and C. N. Chu. Micro electrochemical milling. *Journal of Micromechanics and Microengineering*, 15(1):124–129, 2005.
- [38] T. Kinoshita, M. Hane, and J. P. McVittie. Notching as an example of charging in uniform high density plasmas. *Journal of Vacuum Science & Technology B*, 14(1):560–565, 1996.
- [39] V. Kirchner, L. Cagnon, R. Schuster, and G. Ertl. Electrochemical machining of stainless steel microelements with ultrashort voltage pulses. *Applied Physics Letters*, 79(11):1721–1723, 2001.
- [40] V. Kirchner, X. H. Xia, and R. Schuster. Electrochemical nanostructuring with ultrashort voltage pulses. *Accounts of Chemical Research*, 34(5):371–377, 2001.
- [41] M. Kock, V. Kirchner, and R. Schuster. Electrochemical micromachining with ultrashort voltage pulses - a versatile method with lithographical precision. *Electrochimica Acta*, 48(20-22):3213–3219, 2003.
- [42] D. M. Kolb, R. Ullmann, and T. Will. Nanofabrication of small copper clusters on gold(111) electrodes by a scanning tunneling microscope. *Science*, 275(5303):1097–1099, 1997.

- [43] M. Kunieda, R. Katoh, and Y. Mori. Rapid prototyping by selective electrodeposition using electrolyte jet. *Annals of the CIRP*, 47(1):161–164, 1998.
- [44] M. Kunieda, M. Yoshida, and H. Yoshida. Influence of micro indents formed by electro-chemical jet machining on rolling bearing fatigue life. *ASME PED*, 64:693–699, 1993.
- [45] D. Landolt, P. F. Chauvy, and O. Zinger. Electrochemical micromachining, polishing and surface structuring of metals: fundamental aspects and new developments. *Electrochimica Acta*, 48(20-22):3185–3201, 2003.
- [46] W. Li, G. S. Hsiao, D. Harris, R. M. Nyffenegger, J. A. Virtanen, and R. M. Penner. Mechanistic study of silver nanoparticle deposition directed with the tip of a scanning tunneling microscope in an electrolytic environment. *Journal of Physical Chemistry*, 100(51):20103–20113, 1996.
- [47] M.A. Lieberman and A.J. Lichtenberg. *Principles of Plasma Discharges and Materials Processing*, pages 25–190. Wiley, New York, 1994.
- [48] T. L. Lievestro. Electrochemical machining. In *ASM Handbook Vol. 16, Machining*, pages 533–541. ASM International, 1989.
- [49] Z. L. Liu, X. B. Jing, and K. L. Yao. Simulation of ion transport characteristics in a collisionless rf sheath. *Journal of Physics D: Applied Physics*, 38(12):1899–1904, 2005.
- [50] C. K. Malek and V. Saile. Applications of LIGA technology to precision manufacturing of high-aspect-ratio micro-components and systems: a review. *Microelectronics Journal*, 35(2):131–143, 2004.

- [51] G. Malone and M. E. Browning. Electroforming. In *ASM Handbook Vol. 5, Surface Engineering*. ASM International, 1994.
- [52] T. Masuzawa. State of the art of micromachining. *Annals of the CIRP*, 49(2):473–488, 2000.
- [53] Jun Matsui, Kazunobu Maeshige, and Toshiaki Makabe. Effect of aspect ratio on topographic dependent charging in oxide etching. *Journal of Physics D: Applied Physics*, 34:2950–2955, 2001.
- [54] Makoto Matsumoto and Takuji Nishimura. Mersenne twister: A 623-dimensionally equidistributed uniform pseudorandom number generator. *ACM Trans. on Modeling and Computer Simulation*, 8(1):3–30, 1998.
- [55] W. Natsu, T. Ikeda, and M. Kunieda. Machining complicated patterns with electrolyte jet machining. *Proceedings of the 5th Euspen International Conference*, pages 649–652, 2005.
- [56] M. A. Newton. Electrostream and capillary drilling. In *ASM Handbook Vol. 16, Machining*, pages 551–553. ASM International, 1989.
- [57] M. A. Newton. Shaped tube electrolytic machining. In *ASM Handbook Vol. 16, Machining*, pages 554–556. ASM International, 1989.
- [58] T. G. Northrop. Dusty plasmas. *Physica Scripta*, 45(5):475–490, 1992.
- [59] D. Padhi, J. Yahalom, S. Gandikota, and G. Dixit. Planarization of copper thin films by electropolishing in phosphoric acid for ULSI applications. *Journal of the Electrochemical Society*, 150(1):G10–G14, 2003.

- [60] S. M. Park and J. S. Yoo. Electrochemical impedance spectroscopy for better electrochemical measurements. *Analytical Chemistry*, 75(21):455A–461A, 2003.
- [61] W. H. Press, S. A. Teukolsky, W. T. Vetterling, and B. P. Flannery. *Numerical Recipes in Fortran Vol. 1*, pages 89–91. Cambridge University Press, Cambridge, 2nd edition, 1992.
- [62] L. T. Romankiw. A path: from electroplating through lithographic masks in electronics to LIGA in MEMS. *Electrochimica Acta*, 42(20-22):2985–3005, 1997.
- [63] R. Schuster, V. Kirchner, P. Allongue, and G. Ertl. Electrochemical micromachining. *Science*, 289(5476):98–101, 2000.
- [64] R. Schuster, V. Kirchner, X. H. Xia, A. M. Bittner, and G. Ertl. Nano-scale electrochemistry. *Physical Review Letters*, 80(25):5599–5602, 1998.
- [65] M. H. Sen and H. S. Shan. A review of electrochemical macro- to micro-hole drilling processes. *International Journal of Machine Tools & Manufacture*, 45(2):137–152, 2005.
- [66] J. A. Sethian. *Level Set Methods and Fast Marching Methods*, pages 60–74. Cambridge University Press, Cambridge, 2nd edition, 1999.
- [67] J. R. Shewchuk. An introduction to the conjugate gradient method without the agonizing pain. Technical Report CMU-CS-94-125, School of Computer Science, Carnegie Mellon University, 1994.



- [68] H. Shin, C. C. King, T. Horiuchi, and C. M. Hu. Thin oxide charging current during plasma-etching of aluminum. *IEEE Electron Device Letters*, 12(8):404–406, 1991.
- [69] S. M. Silaimani and S. John. Review on recent advances in electroforming during the last decade. *Bulletin of Electrochemistry*, 17(12):553–560, 2001.
- [70] I. I. Suni and B. Du. Cu planarization for ULSI processing by electrochemical methods: a review. *IEEE Transactions on Semiconductor Manufacturing*, 18(3):341–349, 2005.
- [71] T. Tatsumi, Y. Hikosaka, S. Morishita, M. Matsui, and M. Sekine. Etch rate control in a 27 MHz reactive ion etching system for ultralarge scale integrated circuit processing. *Journal of Vacuum Science & Technology A*, 17(4):1562–1569, 1999.
- [72] A. L. Trimmer, J. L. Hudson, M. Kock, and R. Schuster. Single-step electrochemical machining of complex nanostructures with ultrashort voltage pulses. *Applied Physics Letters*, 82(19):3327–3329, 2003.
- [73] A. L. Trimmer, J. J. Maurer, R. Schuster, G. Zangari, and J. L. Hudson. All-electrochemical synthesis of submicrometer Cu structures on electrochemically machined p-Si substrates. *Chemistry of Materials*, 17(26):6755–6760, 2005.
- [74] L. M. Wiesenberger and B. J. Durkin. Copper plating. In *ASM Handbook Vol. 5, Surface Engineering*, pages 159–169. ASM International, 1994.

- [75] D. H. Woo, H. Kang, and S. M. Park. Fabrication of nanoscale gold disk electrodes using ultrashort pulse etching. *Analytical Chemistry*, 75(23):6732–6736, 2003.
- [76] X. H. Xia, R. Schuster, V. Kirchner, and G. Ertl. The growth of size-determined Cu clusters in nanometer holes on Au(111) due to a balance between surface and electrochemical energy. *Journal of Electroanalytical Chemistry*, 461(1-2):102–109, 1999.
- [77] J. S. Yoo and S. M. Park. An electrochemical impedance measurement technique employing Fourier transform. *Analytical Chemistry*, 72(9):2035–2041, 2000.
- [78] J. S. Yoo, I. Song, J. H. Lee, and S. M. Park. Real-time impedance measurements during electrochemical experiments and their application to aniline oxidation. *Analytical Chemistry*, 75(14):3294–3300, 2003.

# Index

- Abstract*, vi
- Acknowledgments*, v
- Appendices*, 99
- Bibliography*, 138
- Butler-Volmer Equation, 12
- Capacitance, 123
- Capacitive Current, 14
- Capillary Drilling, 104
- Charge Depletion, 19
- Conjugate Gradient, 23, 26, 73
- Damascene Process, 113
- Dedication*, iv
- Differential Charging, 65
- Dissolution Current, 27, 56, 59
  - Evolution of, 34
- Double Layer Capacity, 9, 20
- ECM-USVP, 4, 17, 114
- Electro Stream Drilling, 104
- Electrochemical Double Layer, 7
- Electrochemical Drilling, 101
- Electrochemical Fabrication, 100
- Electrochemical Jet Machining, 103
- Electrochemical Polishing, 109
- Electroforming, 111
- Electrolyte Resistivity, 20, 117, 120
- Electroplating, 107
- Equations of Motion, 125
- Etch Resolution, 36
- Extension Velocity, 30
- Faradaic Current, 12
- Gauss's Law, 72, 74
- Gouy-Chapman-Stern Model, 7, 20
- Hole Drilling Processes, 101
- Ideal Polarized Electrode (IPE), 12, 13
- Ion Flux, 89
- Ion Trajectories, 88
- Jacobi Preconditioner, 27
- Jet Electrolytic Drilling, 105
- Laplace Equation, 69, 72
- Level Set Method, 28
- Masked Processes, 111
- Mersenne Twister, 72
- Narrow Band Method, 30
- Overpotential, 12, 22, 55, 58
  - Evolution of, 34
- Particle Generation, 71
- Particle Trajectory Calculation, 75, 125
- Plasma Charging of Dielectric, 67
- Plasma Sheath, 63
- Polarization Resistance, 15, 20
- Potential Contours, 84
- Potential Statistics, 83
- Profile Evolution, 27
- Pulsed Electrochemical Machining, 114

Runge-Kutta Method, 75, 125

Shaped Tube Electrochemical Machining, 102

Sheet Resistance, 76

Surface Conduction, 76

Surface Finishing, 107

Tafel Equations, 13

Tool Arrays, 57

Tool Templates, 50

Transient Charging Simulation, 22

Transient Current Response, 31

Transient Potential, 78

## Vita

Jason Andrew Kenney was born in Covington, Kentucky on 4 December, 1973, the son of Bobby Gene and Aline Kenney. He received Bachelor of Science degrees for both Chemical Engineering and Mathematics from the University of Kentucky in 1996, then received the Master of Science degree in Chemical Engineering from the California Institute of Technology in 1999. Following employment in the engineering consulting field, he became a volunteer teacher in northern Thailand for long enough to find the ‘sanook.’ He returned to the US to pursue a PhD at the University of Texas at Austin in August, 2002.

Permanent address: 435 Mason Rd.  
Williamstown, KY 41097

This dissertation was typeset with L<sup>A</sup>T<sub>E</sub>X<sup>†</sup> by the author.

---

<sup>†</sup>L<sup>A</sup>T<sub>E</sub>X is a document preparation system developed by Leslie Lamport as a special version of Donald Knuth’s T<sub>E</sub>X Program.